

การสังเคราะห์ถ่านกัมมันต์เจือไนโตรเจนจากซากหนอนไหมและใบก้ามปู
เพื่อประยุกต์ในตัวเก็บประจุยิ่งยวด

SYNTHESIS OF NITROGEN-DOPED ACTIVATED CARBON DERIVED FROM
SILKWORM PUPAE AND SAMANEA SAMAN LEAVES FOR
SUPERCAPACITOR APPLICATION



วิทยานิพนธ์นี้เป็นส่วนหนึ่งของการศึกษาตามหลักสูตรปริญญาปรัชญาดุษฎีบัณฑิต

สาขาวิชานาโนวิทยาและนาโนเทคโนโลยี

วิทยาลัยนาโนเทคโนโลยีพระจอมเกล้าลาดกระบัง

สถาบันเทคโนโลยีพระจอมเกล้าเจ้าคุณทหารลาดกระบัง

พ.ศ. 2561

KMITL-2019-NT-D-001-003

This material is reserved for educational use only, not allowed for commercial use.

Forbidden to modify the content, and cite the document when use.

SYNTHESIS OF NITROGEN-DOPED ACTIVATED CARBON DERIVED
FROM SILKWORM PUPAE AND SAMANEA SAMAN LEAVES FOR
SUPERCAPACITOR APPLICATION



A THESIS SUBMITTED IN PARTIAL FULFILLMENT
OF THE REQUIREMENT FOR THE DEGREE OF
DOCTOR OF PHILOSOPHY IN NANOSCIENCE AND NANOTECHNOLOGY
COLLEGE OF NANOTECHNOLOGY
KING MONGKUT'S INSTITUTE OF TECHNOLOGY LADKRABANG

2018

KMITL-2019-NT-D-001-003

This material is reserved for educational use only, not allowed for commercial use.

Forbidden to modify the content, and cite the document when use.



COPYRIGHT 2018

COLLEGE OF NANOTECHNOLOGY

KING MONGKUT'S INSTITUTE OF TECHNOLOGY LADKRABANG

This material is reserved for educational use only, not allowed for commercial use.

Forbidden to modify the content, and cite the document when use.

หัวข้อวิทยานิพนธ์	การสังเคราะห์ถ่านกัมมันต์เจือไนโตรเจนจากซากหนอนไหม และใบก้ามปูเพื่อประยุกต์ในตัวเก็บประจุยิ่งยวด
นักศึกษา	นางสาววิชญา สัตยารัฐ
รหัสประจำตัว	56607013
ปริญญา	ปรัชญาดุษฎีบัณฑิต
สาขาวิชา	นาโนวิทยาและนาโนเทคโนโลยี
พ.ศ.	2561
อาจารย์ที่ปรึกษาวิทยานิพนธ์	ผู้ช่วยศาสตราจารย์ ดร.วินัดดา วงศ์วิริยะพันธ์

บทคัดย่อ

ตัวเก็บประจุยิ่งยวดมีความสำคัญสำหรับการใช้พลังงานหมุนเวียนเพื่อทดแทนพลังงานเชื้อเพลิง ตัวเก็บประจุยิ่งยวดเป็นตัวเก็บประจุแบบไฟฟ้าเคมีมีข้อดี คือให้ค่าความหนาแน่นกำลังไฟฟ้าสูง อัตราการเก็บและคายประจุเร็ว และอายุการใช้งานนาน อย่างไรก็ตามยังมีความจำเป็นต้องพัฒนาค่าความหนาแน่นพลังงานสำหรับการนำไปประยุกต์ใช้งานจริง ซึ่งมี 2 ตัวแปรสำคัญคือค่าความจุไฟฟ้าจำเพาะและช่วงความต่างศักย์ของขั้วไฟฟ้า งานวิจัยนี้จึงศึกษาการเพิ่มค่าความหนาแน่นพลังงานโดยการเพิ่มค่าความจุไฟฟ้าโดยใช้ถ่านกัมมันต์เจือไนโตรเจนจากกากการเกษตรที่มีไนโตรเจนสูงโดยเลือกใช้ซากหนอนไหมและใบก้ามปู โดยงานวิจัยส่วนแรกศึกษาการสังเคราะห์ถ่านกัมมันต์โดยใช้ซากหนอนไหมเป็นสารตั้งต้นด้วยวิธีไฮโดรเทอร์มอลและการกระตุ้นทางเคมีด้วยซิงค์คลอไรด์ที่อุณหภูมิ 700 – 900 องศาเซลเซียส พบว่าปริมาณไนโตรเจนในถ่านกัมมันต์ที่ได้จากซากหนอนไหมมีค่าประมาณ 3.8 – 6.4 at% มีค่าลดลงตามอุณหภูมิ ในขณะที่พื้นที่ผิวมีค่าประมาณ 1062 – 1267 ตารางเมตรต่อกรัมซึ่งเพิ่มขึ้นตามอุณหภูมิ ถ่านกัมมันต์ที่เจือไนโตรเจนอุณหภูมิ 800 องศาเซลเซียส ให้ค่าความจุไฟฟ้าสูงสุด 92 ฟารัดต่อกรัมและค่าความหนาแน่นพลังงาน 18 วัตต์ชั่วโมงต่อกิโลกรัมในอิเล็กโทรไลต์แบบออร์แกนิก ซึ่งมีประสิทธิภาพการเก็บประจุสูงกว่าแม้จะมีพื้นที่ผิวน้อยกว่าถ่านกัมมันต์เชิงพาณิชย์ เนื่องจากถ่านกัมมันต์เจือไนโตรเจนสูงช่วยเพิ่มประสิทธิภาพการเก็บประจุแบบซูโดคาปซิเตอร์ และช่วยเพิ่มการนำไฟฟ้าของวัสดุ งานวิจัยส่วนที่สองศึกษาการสังเคราะห์ถ่านกัมมันต์โดยใบก้ามปูเป็นสารตั้งต้นและใช้วิธีการสังเคราะห์แบบขั้นตอนเดียวด้วยการกระตุ้นทางเคมีโดยไม่ผ่านกระบวนการไพโรไลซิส พบว่าอัตราส่วนใบก้ามปูต่อโซเดียมไฮดรอกไซด์ที่ 1:2 มีพื้นที่ผิว 2930 ตารางเมตรต่อกรัม ไนโตรเจน 4.6 at% ค่าความจุไฟฟ้าสูงสุด 179 ฟารัดต่อ

กรัมในสารละลายอิเล็กโทรไลต์แบบออร์แกนิก มีความเสถียร 97.5% หลังการใช้งาน 3000 รอบ สามารถเพิ่มความหนาแน่นของพลังงานโดยการขยายความต่างศักย์ได้ถึง 3.5 โวลต์ ได้ค่าความหนาแน่นพลังงาน 79 วัตต์ชั่วโมงต่อกิโลกรัม จากผลการวิจัยแสดงให้เห็นว่าสามารถสังเคราะห์ ถ่านกัมมันต์เจือไนโตรเจนจากใบก้ามปูโดยใช้เทคนิคการกระตุ้นทางเคมีเพียงขั้นตอนเดียว สามารถลดต้นทุนในการผลิต และสามารถเพิ่มความหนาแน่นพลังงานโดยเพิ่มค่าการเก็บประจุและเพิ่มความต่างศักย์ได้

คำสำคัญ : ถ่านกัมมันต์ การเจือไนโตรเจน กากการเกษตร ตัวเก็บประจุยิ่งยวด ความหนาแน่นพลังงาน



Thesis Title	Synthesis of nitrogen-doped activated carbon derived from silkworm pupae and <i>Samanea Saman</i> leaves and application for supercapacitor application
Student	Ms. Vichuda Sattayarut
Student ID	56607013
Degree	Doctor of Philosophy
Program	Nanoscience and Nanotechnology
Year	2018
Thesis advisor	Asst. Prof. Dr. Winadda Wongwiriyanon

ABSTRACT

Supercapacitor is one of the great importance for the use of renewable energy instead of fossil fuels. Supercapacitor or electrochemical capacitor has advantages including high power density, high rates of charge/discharge, and long cycle life. However, it is necessary to enhance the energy density for practical application. There are two essential parameters to optimize: specific capacitance value and potential range of electrode. This research has focused on the enhancement of energy density by nitrogen-doped activated carbons (ACs) derived silkworm pupae and *Samanea saman* leaves, which are nitrogen-enriched agricultural wastes. The nitrogen-doped ACs from silkworm pupae were conducted (P-ACs) via hydrothermal and chemical activation by using zinc chloride at 700 – 900 °C. The nitrogen content in the P-ACs was approximately 3.8 – 6.4 at%, decreasing with activation temperature, while the surface area was approximately 1062 – 1267 m² g⁻¹, increasing with activation temperature. The P-ACs synthesized at 800 °C showed the highest specific capacitance of 92 F g⁻¹ and the highest energy density of 18 Wh kg⁻¹ in organic electrolytes, surpassing commercial ACs despite possessing smaller surface area. The high nitrogen content enhanced the pseudocapacitance and improved conductivity of the ACs. On the other hand, the nitrogen-doped ACs from *Samanea saman* leaves (SSL) were conducted using a one-step chemical activation without carbonization process. The ratio of SSL and sodium hydroxide of 1:2 showed the superior properties of ACs in terms of a high surface area of 2930 m² g⁻¹, a nitrogen content of 4.6 at%, a specific

This material is reserved for educational use only, not allowed for commercial use.

capacitance of 179 F g^{-1} in organic electrolyte, an excellent cycling stability of 97.5 % after 3000 cycles, an energy density of 79 Wh kg^{-1} at a voltage range of 3.5 V. These results imply that the direct activation of nitrogen-enriched SSLs offering the advantages in terms of a short time, low cost and high energy density by enhancing specific capacitance and voltage range.

Keywords : Activated carbon, Nitrogen doping, Agricultural wastes, Supercapacitor, Energy density



ACKNOWLEDGEMENTS

Firstly, I would like to express my deep and sincere gratitude to my advisor, Asst. Prof. Dr. Winadda Wongwiriyan (College of Nanotechnology, King Mongkut's Institute of Technology Ladkrabang (KMITL)) for her encouragement, helpful suggestions, remarkable patience, and kind support.

I am deeply grateful to dissertation committees, Assoc. Prof. Dr. Wisanu Pecharapa, Dr. Mayuree Phonyiem, Asst. Prof. Dr. Tosapol Maluangnont (College of Nanotechnology, KMITL), Dr. Chalathorn Chanthad (National Nanotechnology Center, NANOTEC) for their comments and suggestions on this dissertation.

I would like to acknowledge the technical supports from Dr. Michiko Obata, Assoc. Prof. Dr. Masatsugu Fujishige, Assoc. Prof. Dr. Kenji Takeuchi, Prof. Morinobu Endo (Shinshu University), Dr. Paisan Khanchaitit, Dr. Pongtanawat Khemthong and Dr. Sanchai Kuboon (NANOTEC).

I would like to acknowledge the financial support from the Development of Activated Carbon Production Technology from Biomasses for Supercapacitor Project (P1750165) from NANOTEC and the Exchange Scholarships with the Institution of Foreign Higher Education, King Mongkut's Institute of Technology Ladkrabang (2018).

I would like to thank all the colleagues and friends, especially those who are the members of Carbon Nanomaterials Research Laboratory, College of Nanotechnology, KMITL for their supports and kindnesses.

Finally, this dissertation is dedicated to my parent, my sister and my best friends for their supports.

Vichuda Sattayarut

CONTENTS

	Page
บทคัดย่อ	i
ABSTRACT	iii
ACKNOWLEDGEMENTS	v
CONTENTS	vi
LIST OF TABLES	xi
LIST OF FIGURES	xiii
CHAPTER 1 INTRODUCTION.....	1
1.1 Significance of research.....	1
1.2 Objective of the study.....	3
1.3 Scope of the study	3
1.4 Thesis structure	4
CHAPTER 2 THEORY AND LITERATURE REVIEWS.....	6
2.1 Comparison of energy storage devices.....	6
2.2 Basic structure of supercapacitors	7
2.2.1 Electrode materials	8
2.2.2 Electrolytes.....	9
2.2.3 Separator	12
2.3 Type and working mechanism of supercapacitors.....	12
2.3.1 Electric double-layer capacitors.....	12
2.3.2 Pseudocapacitors.....	14
2.3.3 Hybrid supercapacitor	15
2.4 Activated Carbons	16
2.4.1 Preparation method of activated carbons from biomass.....	17

This material is reserved for educational use only, not allowed for commercial use.

Forbidden to modify the content, and cite the document when use.

CONTENTS (Cont.)

	Page
2.4.2 Pseudocapacitive effect of heteroatoms in the carbon network.....	20
2.4.3 Literature reviews on pseudocapacitive effect of heteroatoms-doped electrodes.....	23
CHAPTER 3 ANALYTICAL METHODS.....	27
3.1 Characterization of electrode materials.....	27
3.1.1 Scanning electron microscopy.....	27
3.1.2 Transmission electron microscopy.....	28
3.1.3 Nitrogen-adsorption isotherms.....	29
3.1.4 X-ray diffraction.....	33
3.1.5 X-ray photoelectron spectroscopy.....	35
3.1.6 Raman spectroscopy.....	36
3.2 Characterization of electrochemical properties.....	38
3.2.1 Cyclic voltammetry.....	39
3.2.2 Galvanostatic charge-discharge (CD).....	41
3.2.3 Electrochemical impedance spectroscopy (EIS).....	43
3.2.4 Energy and power density.....	44
CHAPTER 4 NITROGEN SELF-DOPED ACTIVATED CARBON DERIVED FROM SILKWORM PUPAE WASTE AND ITS ELECTROCHEMICAL PROPERTIES.....	46
4.1 Synthesis of nitrogen self-doped activated carbons from silkworm pupae by hydrothermal and chemical activation ..	47

This material is reserved for educational use only, not allowed for commercial use.

Forbidden to modify the content, and cite the document when use.

CONTENTS (Cont.)

	Page
4.2 Characterization of activated carbon derived from silkworm pupae.....	49
4.2.1 Morphology of activated carbon derived from silkworm pupae	49
4.2.2 Internal structure of activated carbons derived from silkworm pupae.....	50
4.2.3 Surface area and porosity of activated carbon derived from silkworm pupae.....	51
4.2.4 Crystallinity of activated carbons derived from silkworm pupae	53
4.2.5 Elemental composition of activated carbon derived from silkworm pupae.....	55
4.3 Electrochemical properties of activated carbon derived from silkworm pupae.....	58
4.3.1 Electrode preparation.....	58
4.3.2 Electrochemical measurement systems.....	58
4.3.3 Electrochemical performance of activated carbon derived from silkworm pupae in aqueous electrolyte	61
4.3.4 Electrochemical performance of activated carbon derived from silkworm pupae in organic electrolyte...	65
4.4 Summary.....	69
CHAPTER 5 NITROGEN SELF-DOPED ACTIVATED CARBON DERIVED FROM SAMANEA SAMAN LEAVES AND ITS ELECTROCHEMICAL PROPERTIES.....	71

CONTENTS (Cont.)

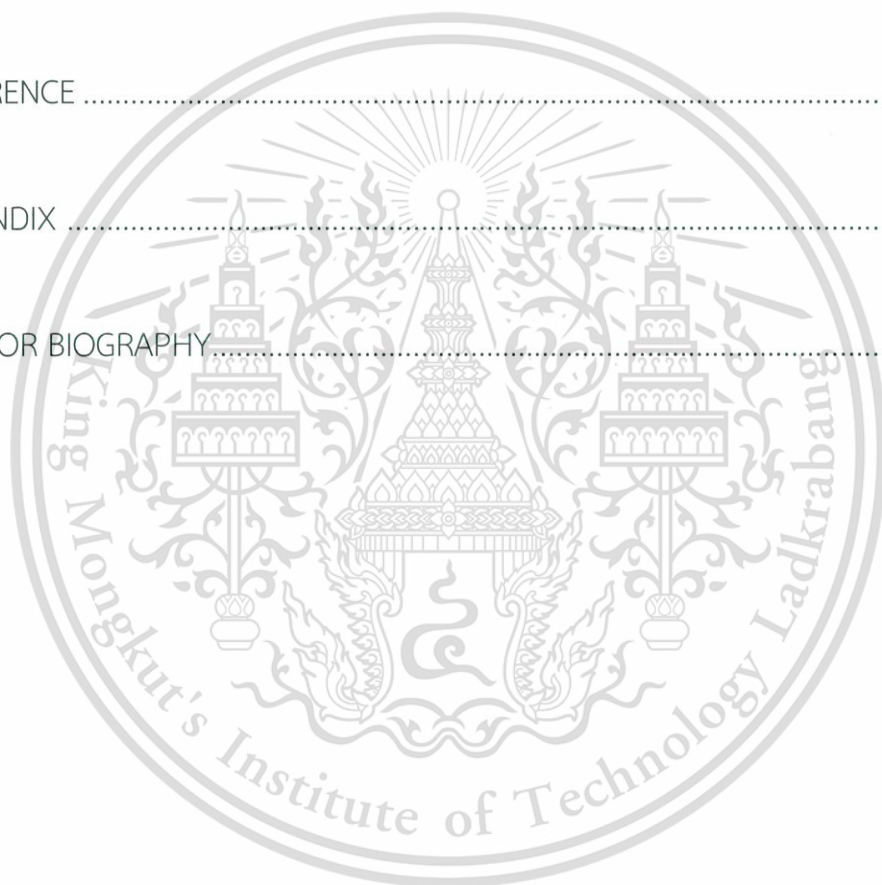
	Page
5.1 Synthesis of nitrogen self-doped activated carbons from <i>Samanea saman</i> leaves by direct activation	72
5.2 Characterization of activated carbon derived from <i>Samanea saman</i> leaves by direct activation	74
5.2.1 Morphology of activated carbon derived from <i>Samanea saman</i> leaves.....	75
5.2.2 Surface area and porosity of activated carbon derived from <i>Samanea saman</i> leaves.....	76
5.2.3 Crystallinity of activated carbon derived from <i>Samanea saman</i> leaves.....	79
5.2.4 Crystal plane structure of activated carbon derived from <i>Samanea saman</i> leaves.....	80
5.2.5 Element composition of activated carbon derived from <i>Samanea saman</i> leaves.....	81
5.3 Electrochemical properties of activated carbon derived from <i>Samanea saman</i> leaves	85
5.3.1 Electrode preparation	85
5.3.2 Electrochemical measurement systems.....	85
5.3.3 Electrochemical performance of activated carbon derived from <i>Samanea saman</i> leaves	88
5.3.4 Enhancement of energy density by extending voltage window.....	93
5.4 Summary.....	97
CHAPTER 6 CONCLUSIONS	98

This material is reserved for educational use only, not allowed for commercial use.

Forbidden to modify the content, and cite the document when use.

CONTENTS (Cont.)

	Page
6.1 Synthesis of nitrogen-doped activated carbon derived from <i>silkworm pupae and Samanea Saman</i> leaves for supercapacitor application.....	98
6.2 Suggestions for future work.....	101
REFERENCE	102
APPENDIX	107
AUTHOR BIOGRAPHY.....	112



LIST OF TABLES

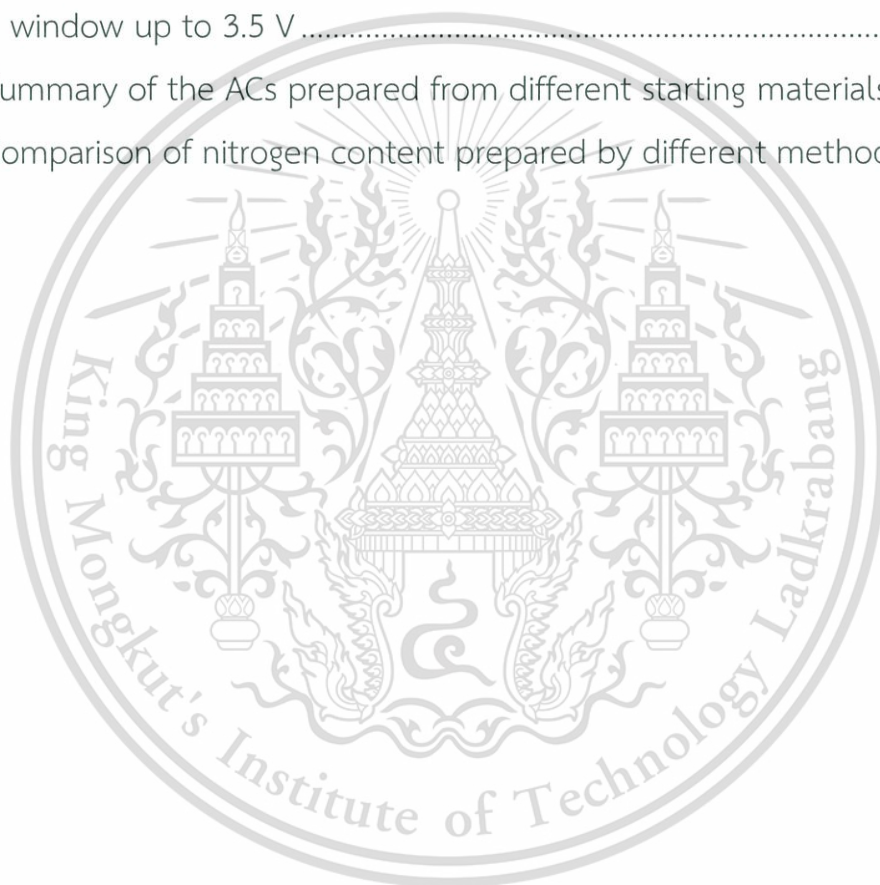
Table	Page
2.1 Comparison of energy storage devices.....	7
2.2 Properties of carbon materials used as electrodes in EDLCs.....	9
2.3 Comparison of each electrolyte	10
2.4 The ion size of TEABF ₄ in PC	11
2.5 Comparison of each type of supercapacitors	16
2.6 Literature reviews of supercapacitor based on ACs derived from biomass.....	24
2.7 Literature reviews of nitrogen self-doped ACs derived from biomass ..	25
2.8 Comparison of nitrogen-doping methods.....	26
3.1 Electrochemical techniques.....	39
4.1 Condition of chemical activation process.....	48
4.2 Characterization techniques and their corresponding information.....	49
4.3 Surface and porosity properties of all samples.....	53
4.4 Chemical composition of all samples evaluated from XPS spectra	57
4.5 Test condition based on aqueous and organic electrolytes.....	59
4.6 Condition measurement of electrochemical properties.....	60
4.7 Electrochemical performance of the P-ACs and YP50 electrodes in aqueous electrolyte.....	64
4.8 Electrochemical performance of P-ACs and YP50.....	67
5.1 Condition of a direct activation for synthesis of ACs derived from SSLs	74
5.2 Characterization techniques and their corresponding information.....	75
5.3 Porosity properties of SD- and S-ACs.....	78
5.4 Chemical composition of the SD- and S-ACs evaluated from XPS spectra.....	84
5.5 Test condition based on organic electrolytes.....	86

This material is reserved for educational use only, not allowed for commercial use.

Forbidden to modify the content, and cite the document when use.

LIST OF TABLES (Cont.)

Table	Page
5.6 Measurement condition of electrochemical properties based on organic electrolyte.....	87
5.7 Summary of electrochemical properties of the SD- and S-ACs.....	92
5.8 Summary of electrochemical properties of the SD2 at the voltage window up to 3.5 V.....	95
6.1 Summary of the ACs prepared from different starting materials.....	100
6.2 Comparison of nitrogen content prepared by different methods.....	101



LIST OF FIGURES

Figure	Page
1.1 Diagram of thesis structure	5
2.1 Ragone plot comparison of energy storage devices	6
2.2 Charged and discharged states of a supercapacitor	8
2.3 Model of the EDLCs: (a) Helmholtz model, (b) Gouy-Chapman model and (c) Stern model	14
2.4 Process flow diagram of ACs production	17
2.5 Parameters influencing hydrothermal converting of biomass	18
2.6 Nitrogenated functional groups in the carbon network (a) pyridinic (N-6); (b) pyrrolic (N-5); (c) pyridonic (N-6) (d) quaternary (N-Q); and (e) oxidized nitrogen (N-X).....	21
2.7 Schematic view of the effect of the properties of the N-5, N-6, N-Q and N-X on the charge transfer resistance.....	22
2.8 Scheme of a possible redox reaction related with pyridinic, pyrrolic and pyridone types.....	23
3.1 (a) Schematic diagram of SEM and (b) A photograph of scanning electron microscope (SEM, HITACHI SU5000).....	28
3.2 (a) Schematic diagram of TEM and (b) A photograph of transmission electronic microscopy (TEM; JEOL JEM-2010)	29
3.3 (a) Types isotherm and (b) hysteresis loops of gas adsorption	30
3.4 Micromeritics ASAP 2020 series gas adsorption systems	33
3.5 (a) A schematic principle of XRD and (b) A photograph of X-ray diffractometry (XRD; Rigaku SmartLab Studio II)	34
3.6 (a) A schematic diagram of basic principle of XPS and (b) A photograph of X-ray photoelectron spectroscopy (XPS; PHI Quantera II)	36
3.7 Raman spectroscopy	37

This material is reserved for educational use only, not allowed for commercial use.

Forbidden to modify the content, **xiii** cite the document when use.

LIST OF FIGURES (Cont.)

Figure	Page
3.8 Typical V-t curves in cyclic voltammetry	40
3.9 The example of cyclic voltammetry graph plot.....	40
3.10 Galvanostatic charge-discharge curve.....	42
3.11 Nyquist plot of supercapacitor	43
4.1 Diagram of the synthesis of ACs derived from silkworm pupae.....	46
4.2 Flow chart of ACs synthesis derived from silkworm pupae.	47
4.3 Photograph of oven furnace for hydrothermal process	48
4.4 FE-SEM images of (a) P-HTC, (b) P700, (c) P800 and (d) P900	50
4.5 TEM images of (a) P-HTC (b) P700 (c) P800 and (d) P900	51
4.6 (a) N ₂ adsorption/desorption isotherms and (b) pore size distribution of all samples.....	53
4.7 XRD diffraction patterns of all samples.....	54
4.8 Raman spectra of all samples.....	55
4.9 (a) N1s and (b) O1s XPS spectra of P-ACs and YP50.....	57
4.10 CV curves of the P-ACs and YP50 electrodes	61
4.11 CD curves of P-ACs and YP50 electrodes	62
4.12 Nyquist plots of the P-ACs and YP50 electrodes.....	63
4.13 Radar plots to show relation of electrochemical performance and (a) porosities and (b) chemical compositions.....	65
4.14 CV curves of the P-ACs and YP50 coil cells	66
4.15 CD curves of the P-ACs and YP50.....	67
4.16 Cycling stability at the 3000 th	69
5.1 Diagram of synthesis of ACs from <i>Samanea saman</i> leaves.....	72
5.2 Flow chart of synthesis of ACs from <i>Samanea saman</i> leaves.....	72

LIST OF FIGURES (Cont.)

Figure	Page
5.3 FE-SEM images at low magnification of (a) SD2 and S-AC. FE-SEM images at high magnification of (c) SD1.5, (d) SD1.75, (e) SD2 and (f) S-AC....	76
5.4 (a) N ₂ adsorption/desorption isotherms, and (b) pore size distribution of the SD- and S-AC.....	78
5.5 XRD diffraction patterns of all samples.....	79
5.6 Raman spectra of all samples.....	81
5.7 (a) N 1s and (b) O 1s XPS spectra of the SD- and S-ACs.....	84
5.8 CV curves of the SD- and S-ACs.....	88
5.9 CD curves of the SD-and S-ACs.....	90
5.10 Nyquist plot of the SD- and S-ACs.....	91
5.11 Capacitance retention of the SD2.....	93
5.12 Specific capacitance by various voltage of SD2 in coin cell.....	94
5.13 Ragone plot of coil cell of SD2 compared to other reports.....	96
5.14 Photograph of coil cell of the P800 light up 64 white and 54 red LEDs.	96

CHAPTER 1

INTRODUCTION

1.1 Significance of research

Nowadays technology has been rapidly developed, causing the significantly increased demand for energy. The fossil fuel is a main energy source for electric power generation. However, the fossil fuel is a limited resource and shows negative impacts of global warming. Hence, energy storage device is one of the great importance for the use of renewable energy instead of fossil fuels. Supercapacitor, known as an electrochemical capacitor (EC), which bridges the gap between conventional capacitor and battery, has the great advantages including a higher power density, a higher rates of charge/discharge, a longer cycle life than battery and a higher energy density than conventional capacitor, and also green environment [1-3]. Supercapacitor consists of three important parts: (i) two electrodes using mainly carbon materials for ion adsorption storage, (ii) a separator to protect electrodes from shorting and (ii) an electrolyte containing cation and anion ions. According to the energy storage mechanisms, supercapacitor is divided to three types; (i) electrical double layer capacitor (EDLC) storing energy via electrostatic intercalation between the electrode/electrolyte interface by using ion adsorption, (ii) pseudocapacitor storing energy via faradic reaction process by using fast surface redox reactions, and (iii) hybrid supercapacitor incorporating the synergistic effects between EDLC and pseudocapacitor [4]. Hence, activated carbon (AC) with high specific surface area is known well as a crucial role in technology for electrode materials of supercapacitor owing to their several functionalities, high surface area, good chemical properties, electrochemical stability and relatively low cost [5]. Generally, the performance of

This material is reserved for educational use only, not allowed for commercial use.

Forbidden to modify the content, and cite the document when use.

supercapacitors depends on the capability of carbon materials and the ion transport. Normally, ACs are derived from carbon-rich organic precursors, for example, coconut shell and wood, to develop the surface area by carbonization treatment process and followed by physical and/or chemical activations. However, ACs have several drawbacks, such as decreasing of electrical conductivity when surface area increased due to its pore tortuosity and poor pore connectivity. Therefore, a great enhancement in capacitance of ACs can be reached by enhancing faradaic reactions and wettability of pore walls via the heteroatom doping such as oxygen and nitrogen [6-9]. The nitrogen-enriched carbons can be obtained by ammoxidation of nanoporous carbons or treatment carbon materials by nitrogen-based gases or chemicals. Nevertheless, these methods are complex and toxic. Thus, the *in situ* self-doping by using the nitrogen-rich biomass as a raw material has been the great of attraction as a renewable and environmental-friendly resource. Moreover, biomass is a class of low-cost carbon precursor with diverse microstructures.

Recently, improvement of a capacitive performance of supercapacitor is necessary to enhance the energy density for the practical application. Thus, by selecting appropriate carbon raw materials, the ACs with a controlled microstructure and doped with the required heteroatoms could be obtained. For example, nitrogen-doped ACs have been successfully synthesized from nitrogen-containing plants and animals such as green leaves, soy beans, yogurt, endothelium corneum gigeriae galli and silk cocoons [10-14]. However, nitrogen content of nitrogen self-doped ACs derived was relatively low compared with the post treatment method due to low nitrogen content in raw materials and loss of nitrogen during preparation process.

This research has focused on the enhancement of energy density by nitrogen-containing ACs derived from silkworm pupae and leaves, which are nitrogen-enriched agricultural wastes. The nitrogen-doped ACs from silkworm pupae were conducted via hydrothermal and $ZnCl_2$ chemical activation. The activation temperature was optimized. On the other hand, the nitrogen-doped ACs from *Samanea saman* leaves

This material is reserved for educational use only, not allowed for commercial use.

Forbidden to modify the content, and cite the document when use.

(SSL) were conducted using a one-step activation. The weight ratio of chemical reagent and SSL was optimized. The properties of ACs in terms of morphology, surface area, porosity, chemical composition were investigated. Finally, the electrochemical properties were characterized. The working potential range was extended by using organic electrolytes compared to the aqueous electrolyte.

1.2 Objective of the study

1.2.1 To enhance the energy density of supercapacitor by increasing capacitance and voltage window

1.2.1.1 To enhance of the specific capacitance value by nitrogen-enriched ACs

1.2.1.2 To increase the potential range of supercapacitor by nitrogen-enriched ACs

1.2.2 To synthesize high nitrogen self-doped ACs by using high nitrogen-containing agricultural wastes as a starting materials and one-step activation

1.2.3 To study the characteristics of the nitrogen self-doped ACs derived from silkworm pupae and *Samanea saman* leaves including the relation between material characteristics and electrochemical properties.

1.3 Scope of the study

1.3.1 Preparation of nitrogen self-doped ACs derived from silkworm pupae by using hydrothermal and chemical activation process

1.3.2 Synthesis of nitrogen self-doped ACs from leaves by using one-step activation

1.3.3 Measurement and comparison of electrochemical properties of supercapacitor based on nitrogen self-doped ACs using aqueous and organic electrolytes

1.4 Thesis structure

This thesis is composed of six chapters as shown in Figure 1.1. Chapter 1 describes the significance of research, the objective and scope of this study. Chapter 2 describes theory related on fundamental of supercapacitor, synthesis and properties of ACs and literature reviews on ACs derived from agricultural wastes. Chapter 3 explains the characterization techniques of electrode material and electrochemical properties. Chapters 4 and 5 present the experimental methodology, results and discussions of nitrogen self-doped ACs derived from silkworm pupae and *Samanea saman* leaves, respectively. Finally, Chapter 6 summarizes the findings from this research and suggestions for the future work.



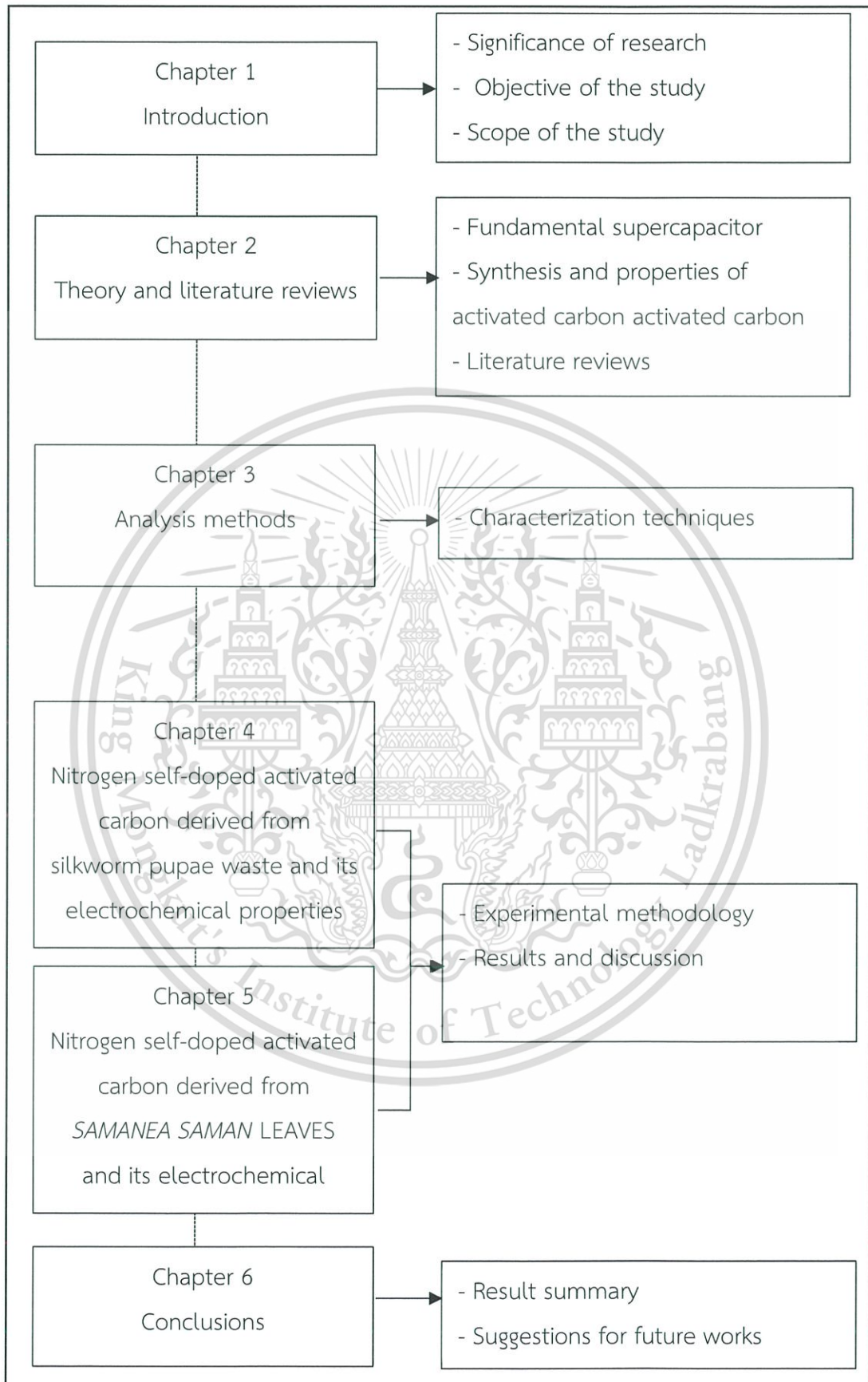


Figure 1.1 Diagram of thesis structure

This material is reserved for educational use only, not allowed for commercial use.

Forbidden to modify the content, and cite the document when use.

CHAPTER 2

THEORY AND LITERATURE REVIEWS

2.1 Comparison of energy storage devices

Supercapacitors (or ultracapacitors or electrochemical capacitors) are an energy storage device based on charging/discharging at the electrode/electrolyte interface of electrode materials. Supercapacitors have bridged the gap between batteries and conventional capacitors. Their performance comparison is shown in Ragone plot as shown in Figure 2.1 [15]. Supercapacitors show the great advantages including a higher power density than batteries and a higher energy density than capacitors. However, supercapacitors suffer from their lower-energy density, whereas batteries exhibit a higher energy density. Moreover, supercapacitors can offer a long cycle life, a very fast charge and discharge time (second to minutes) and also environmentally friendly. Table 2.1 shows a comparison of capacitors, supercapacitors and batteries.

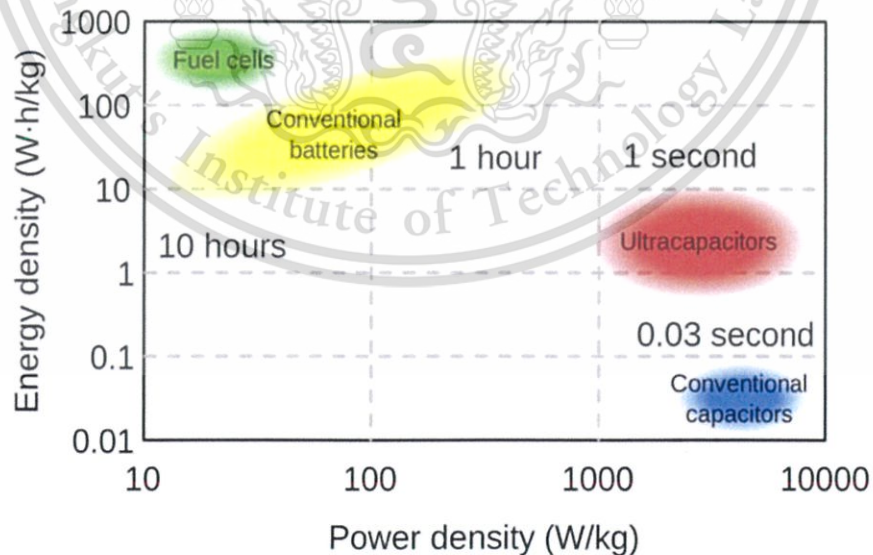


Figure 2.1 Ragone plot comparison of energy storage devices [15]

Table 2.1 Comparison of energy storage devices

Characteristics	Capacitors	Supercapacitors	Batteries
Electrode materials	Al, Ta oxide	Activated carbons	Pb, Ni-Cd, and Ni-MH
Storage mechanism	Electrostatic	Electrostatic	Chemical
Energy density (W h kg ⁻¹)	< 0.1	1 – 10	~20 – 150
Power density (W kg ⁻¹)	>>10,000	500 – 10,000	<10,000
Discharge time	10 ⁻⁶ – 10 ⁻³ seconds	Seconds to minutes	0.3 – 3 hours
Charging time	10 ⁻⁶ – 10 ⁻³ seconds	Seconds to minutes	1 – 5 hours
Cycle life (cycles)	>>10 ⁶ (>>10 years)	>10 ⁶ (>10 years)	~1500 (~3 years)
Maximum voltage	High	<3 – 4 V	Low
Charged storage	Between charged plates	Interface of electrode/electrolyte	Entire electrode
Parameter to demine properties	- Geometric area of the electrodes - Dielectric constant	- Electrode microstructure - Active surface area - Type of electrolyte	- Active mass - Thermodynamics

2.2 Basic structure of supercapacitors

Figure 2.2 represents the basic structure of supercapacitors. Supercapacitors consist of three main parts: (i) two electrodes such as activated carbons to absorb and storage ions, (ii) separator based on an ion-permeable membrane to prevent two electrodes from shorting together, and (iii) electrolyte contains free mobile ions. Before charge state, positive and negative ions are uniformly dispersed in the electrolyte and there is no electric field at the electrode surface. When a voltage is applied, the ions in the electrolytes are attracted to the oppositely charged electrode. Energy is stored

This material is reserved for educational use only, not allowed for commercial use.

as a charge separation in double layers, so called electric-double layer capacitors (EDLCs), formed at the interface between the surface of the electrode material and the electrolyte.

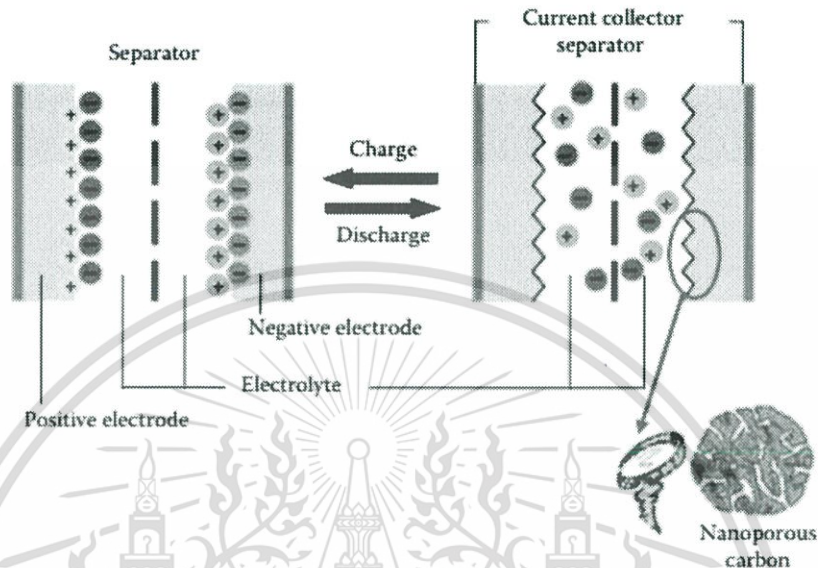


Figure 2.2 Charged and discharged states of a supercapacitor [15]

2.2.1 Electrode materials

Normally, the electrode materials are pasted on the conductive collectors. The electrode materials absorb and storage ions which are mainly carbon materials. Supercapacitors utilize the great properties of carbon materials, including large surface area, relatively good electrical conductivity, excellent chemical stability, and low cost. Carbon materials ranging from conventional activated carbons (ACs) to nano-scale carbon materials such as graphenes and carbon nanotubes have been evaluated as electrode materials for EDLCs as shown in Table 2.2. Among carbon materials, ACs are the most widely used as electrode materials in commercial EDLCs. ACs are attractive materials for EDLCs preparation owing to their extremely high surface area. In theory, the higher the surface area, the higher the specific capacitance of supercapacitor. Aspects such as pore size distribution, material precursor, electrolyte ion size, surface

This material is reserved for educational use only, not allowed for commercial use.

Forbidden to modify the content, and cite the document when use.

wettability, and pore accessibility need to be considered when evaluating a potential electrode material.

Table 2.2 Properties of carbon materials used as electrodes in EDLCs

Electrode material	SSA* (m ² g ⁻¹)	C _S * (F g ⁻¹)	
		Aqueous electrolyte	Organic electrolyte
Activated carbon (ACs)	1000 – 3000	200 – 400	100 – 150
Templated carbons	500 – 2500	120 – 350	120 – 135
Carbon nanotubes (CNTs)	120 – 500	20 – 180	20 – 80
Carbide-derived carbons	1000 - 1600	-	100 – 140

*SSA: Specific surface area and C_S: gravimetric capacitance values.

2.2.2 Electrolytes

The electrolyte is one of the key components of supercapacitor, providing ionic conductivity and facilitating charge compensation on each electrode in the cell. Generally, the electrolytes used in EDLCs can mainly be classified into three types: (i) aqueous electrolyte, (ii) organic electrolyte, and (iii) ionic electrolyte (ILs). Recently, the electrolytes for supercapacitor have developed for new and high-performing electrolytes to obtain a high voltage, high ionic conductivity, low viscosity, a wide working temperature range, low toxicity and low cost. Table 2.3 shows the comparison of each electrolyte [16, 17].

Table 2.3 Comparison of each electrolyte

Characteristics	Electrolyte		
	Aqueous	Organic	Ionic liquids (ILs)
Voltage window (V)	≤ 1.2	2.5-2.8	3-6
Ion size	Small	Moderate	Small
Ionic conductivity ($S\ cm^{-1}$)	Up to ~ 1	$\sim 0.01 - 0.05$	< 0.015
Viscosity (cP)	Low	Moderate/High	High
Cost	Low	Moderate/High	Very high
Assembly condition	Air	Inert atmosphere	Inert atmosphere
Toxicity	Low	Moderate/High	Low

2.2.2.1 Aqueous electrolytes

In general, the aqueous electrolytes are grouped into acid, alkaline, and natural solutions, such as H_2SO_4 , KOH and Na_2SO_4 , respectively. The aqueous electrolytes have a limited voltage range with a relatively low decomposition of water at voltage of $\sim 1.23\ V$ [16]. However, the advantages of the aqueous electrolyte are inexpensive, high ionic conductivity (up to $\sim 1\ S\ cm^{-1}$), smaller aqueous ions and easy handling in the normal environment condition especially assembly process. The specific capacitance ($F\ g^{-1}$) of carbons in the aqueous electrolytes is relatively high compared to other types of electrolytes.

2.2.2.2 Organic electrolytes

The specific capacitance in the organic electrolytes are normally lower than those in the aqueous electrolytes due to their larger solvated ion sizes and lower ionic

conductivity. However, the organic electrolytes are attractive in commercial supercapacitor market owing to their high operating voltage in the range of 2.5 to 2.8 V [18]. The organic electrolytes also have disadvantages in terms of toxicity, flammability and a complicated purification process under strictly controlled atmosphere to avoid the moisture. Currently, efforts have been done to for nontoxic organic electrolyte and good ion conductivity. The most popular of the organic electrolytes is tetraethylammonium tetrafluoroborate (TEABF_4) in propylene carbonate, which has ion size as shown in Table 2.4.

Table 2.4 The ion size of TEABF_4 in PC

Electrolyte	Solvated (nm)	De-solvated (nm)
TEA^+	1.35	0.67
BF_4^-	1.40	0.48

2.2.2.3 Ionic liquid (IL) electrolytes

The ionic liquid (IL) electrolytes have recently gained significant interest as alternative electrolytes for EDLCs [19]. The IL electrolytes are solvent-free molten salts or fused salts at lower or room temperature, possess high thermal and electrochemical stability over 3 V (3 – 6 V), and exhibit negligible volatility. The main IL electrolytes for supercapacitors are pyrrolidinium, imidazolium or aliphatic quaternary ammonium salts coupled with such anions as PF_6^- , BF_4^- , TFSI^- , or FSI^- . However, the disadvantage of the IL electrolytes are high viscosity, very low ionic conductivity and high cost due to a stringent requirement to manage and control preparation processes.

2.2.3 Separator

The separators play a key role in supercapacitor. Their main function is to prevent two electrodes from shorting circuits and allow rapid transport of electrolyte ions. The requirement of separator is a very thin sheet, non-conductive and the capability of conducting ions by either intrinsic ionic conductor or by soaking electrolyte. A separator is a porous membrane which is made of polymer or paper, permeable to ionic of electrolyte flow.

2.3 Type and working mechanism of supercapacitors

Supercapacitors are divided into three categories based on charge storage mechanism and construction: (i) electric double-layer capacitors (EDLCs), (ii) pseudocapacitors and (iii) hybrid capacitors.

2.3.1 Electric double-layer capacitors

The EDLCs have been first introduced by von Helmholtz who first developed and modeled the double-layer concept. The Helmholtz concept explains that a charged surface immersed in an electrolyte solution (both anions and cations) and then the charges at electrode surface and ions form a monolayer near the electrode surface. Two planar oppositely charged layers are formed at an electrode/electrolyte interface and are separated by a small distance d , implying as the radius of an ion (an atomic distance) as shown in Figure 2.3(a) [20]. After that, the Helmholtz model was refined by Gouy and Chapman. They proposed that the ion distribution should be continuous in the electrolyte solution and given by the Boltzmann distribution. The Gouy-Chapman model identifies that ions are mobile in the electrolyte solution under the combined effects of ion diffusion driven and so-called “diffuse layer” as shown in Figure 2.3(b). In 1924, Stern remodeled by combining the Helmholtz model and the Gouy-Chapman model and recognized two regions of ion distribution at the electrode electrolyte interface: (i) inner region of d called the

This material is reserved for educational use only, not allowed for commercial use.

compact layer (or Stern layer) or inner Helmholtz plane (IHP) and (ii) outer region called a diffuse layer or outer Helmholtz plane (OHP) as shown in Figure 2.3(c). In stern layer, ions are strongly adsorbed by the electrode. In diffuse layer, ions are a continuous distribution of electrolyte ions in solution driven by thermal motion. Hence, the capacitance of EDLCs (C_{dl}) are composed of two terms, the stern double-layer capacitance (C_H) and the diffuse region capacitance (C_{diff}). Thus, C_{dl} can be presented by the following equation:

$$\frac{1}{C_{dl}} = \frac{1}{C_H} + \frac{1}{C_{diff}} \quad (2.1)$$

The parameters that determine EDLC behavior are the electrode materials, electrode area, electric field across the electrode, and types of electrolyte ions (ie. solvent in electrolyte, size, electron-pair and dipole moment). Generally, the electrode material with a highly porous with a high specific surface area results in the complex EDLC behavior at pore surface of electrode material. The working principle of EDLCs can explained that (i) before charging, electrolyte ions (positive and negative) are uniformly dispersed without electric field at the electrode surface. (ii) A voltage is applied and the ions are attracted to the electrically opposite electrode. Energy is stored as a charge separation in double layers formed at the interface between the surface of electrode material and the electrolyte.

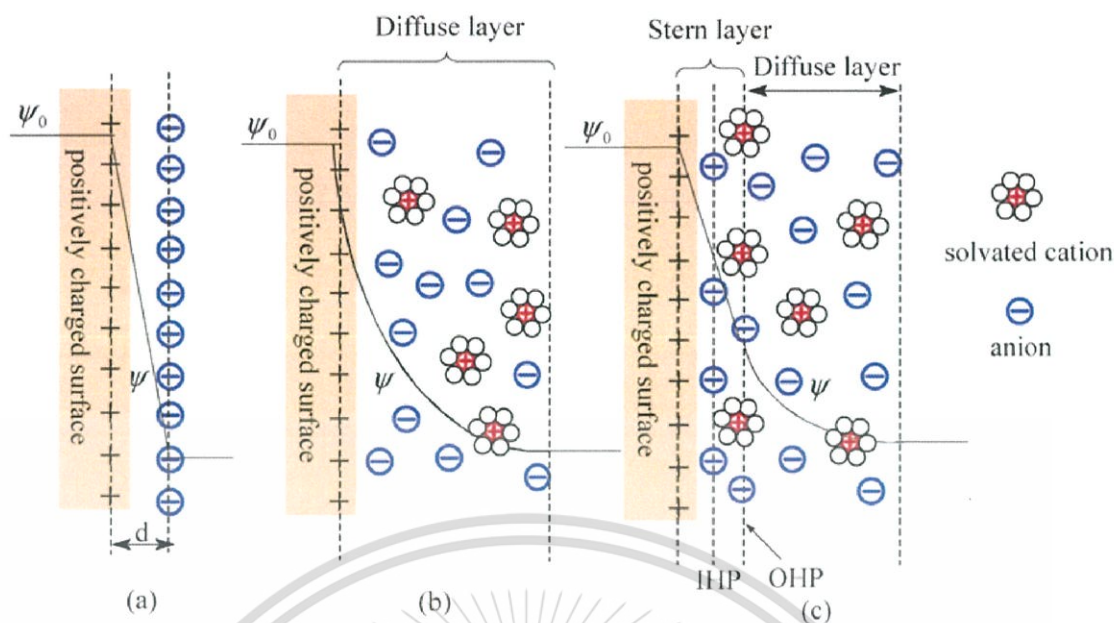


Figure 2.3 Model of the EDLCs: (a) Helmholtz model, (b) Gouy-Chapman model and (c) Stern model [20].

2.3.2 Pseudocapacitors

Pseudocapacitors represents a different kind of capacitance. Pseudocapacitance involves fast and reversible redox reaction between electro-active materials –electrolyte on the electrode surface. One of the most active materials is the transition metal oxide (such as ruthenium oxide) and conductive polymer (such as polyaniline (PANI) and polypyrrole (PPy)). The advantages of the pseudocapacitors are higher specific capacitance than EDLCs owing to the additional performance of active material providing a pseudocapacitive property. For example, amorphous hydrous ruthenium oxide ($\text{RuO}_2 \cdot x\text{H}_2\text{O}$) exhibited a high specific capacitance (720 F g^{-1}) [21]. The redox reaction of ruthenium oxide is as follows:



where $\text{RuO}_x(\text{OH})_y$ and $\text{RuO}_{x-\delta}$ display the interfacial oxyruthenium at higher and lower oxidation states. The proton of H_2SO_4 and the faradic charges can be reversibly stored and delivered through the redox transitions of the oxyruthenium groups. However, EDLCs and pseudocapacitors also have different advantages, i.e. the EDLCs have a higher power output but pseudocapacitors are greater in term of energy density.

2.3.3 Hybrid supercapacitor

Hybrid supercapacitor is combined between EDLCs and pseudocapacitors. Electrode materials used in hybrid supercapacitor are based on porous carbons composited with metal oxide and porous carbons composited with conductive polymer. The electrical energy of hybrid supercapacitor stores by combining between redox reaction electrode and electric double-layer absorption-desorption for others electrode. The advantages of hybrid supercapacitor are relatively great in energy and power densities and good cycling. However, almost of every performance is the intermediate level.

The comparisons of each supercapacitor are shown in Table 2.5.

Table 2.5 Comparison of each type of supercapacitors

Properties	EDLCs	Pseudocapacitors	Hybrid capacitors
Mechanism	Charge separation at the electrode/electrolyte interface	Reversible surface Faradic redox reaction	Redox reaction electrode and electric double-layer absorption/desorption for others electrode
Materials	Porous carbon materials	Transition metal oxide, conductive polymer	Porous carbon, graphene, metal oxide, conductive polymer
Advantage	High power density, good cycling behavior	High capacitance, high energy density	Relative high energy and power densities, good cycling
Disadvantage	Low energy density	Poor cycling	Almost of every performance is the intermediate level

2.4 Activated Carbons

Activated carbons (ACs) is known as high specific surface area. These are used in a wide range of applications concerned principally with the removal of species by adsorption from the liquid or gas phase. Hence, ACs have attracted significant scientific interest as the electrode materials for all types of supercapacitors, especially in EDLC type because of their high surface area, good chemical and electrochemical stabilities. ACs derived from a number of raw materials including agricultural wastes, coal, animal, wood, and synthetic polymer. These raw materials are synthesized to a number of different activation methods such as physical, chemical or combined activations to

afford porous carbon with the high adsorption capacity for a particular application as shown in Figure 2.4.

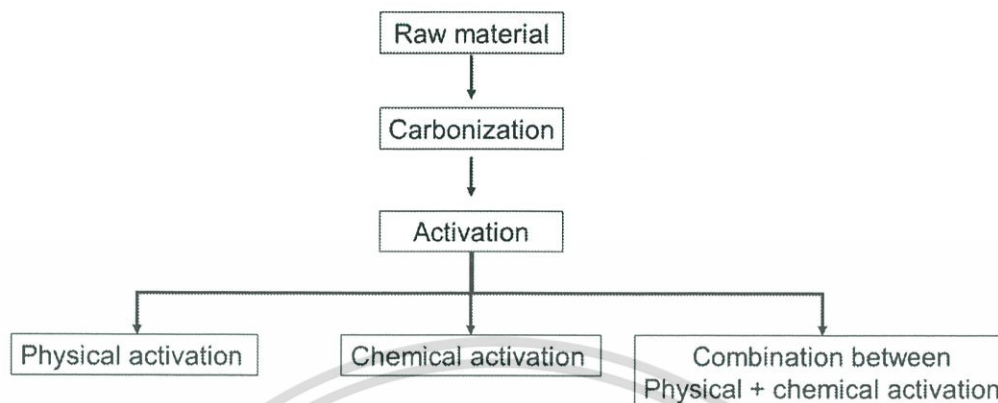


Figure 2.4 Process flow diagram of ACs production

2.4.1 Preparation method of activated carbons from biomass

1. Preparation of raw material

Prior to carbonization process, raw materials or biomass materials were blended into small pieces after drying.

2. Carbonization process

Carbonization process is based on the thermal breakdown of biomass included pyrolysis and hydrothermal processing. During the thermal pyrolysis under an inert atmosphere, the moisture and the volatile matter contents of biomass are removed and remaining solid char which displays properties different from the raw biomass materials. The products obtained as a result of pyrolysis are very depending on several factors, such as biomass type, heating rate, pyrolysis temperature, time, and the presence of catalyst.

Hydrothermal carbonization process is a crucial thermo-chemical conversion used to convert biomass into carbonaceous products. This process is an environmentally friendly and inexpensive technique. The hydrothermal carbonization

This material is reserved for educational use only, not allowed for commercial use.

Forbidden to modify the content, and cite the document when use.

process can be operated at temperatures range of 150-200 °C and get rid of oxygen from biomass. One of the most important advantages of this procedure is able to use biomass with high moisture content under pressure without the need for pre-drying and allow for a higher product yield. Biomass can be converted into the carbonaceous product by changing operating parameters variables such as temperature, time, catalyst presence and pressure as shown in Figure 2.5.

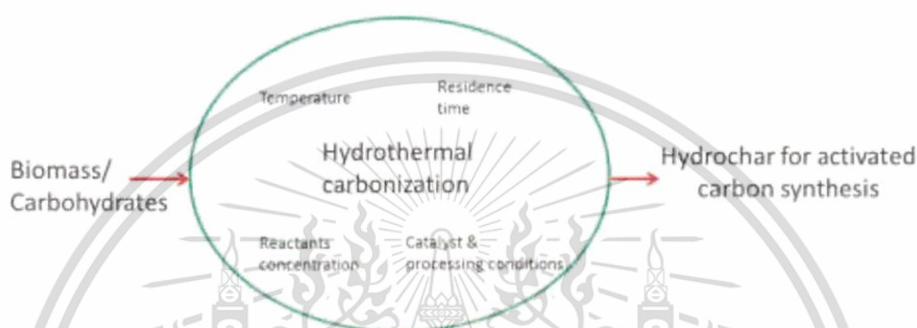


Figure 2.5 Parameters influencing hydrothermal converting of biomass [20]

3. Activation process

Generally, there are two methods for activation process, physical activation, and chemical activation.

(3.1) Physical activation

Physical activation is generally conducted in the presence of air, steam or CO₂. Air activation is conducted under a relatively low temperature <500 °C. The air activation step has been exhibited to dominant the porous properties of biomass-derived carbon. The steam activation process is combined with pyrolysis as single step. It can generate high oxygen-containing group on surface, which lead to a poor electrical conductivity of the resulting carbon. CO₂ activation is the most commonly used physical activation process, which is controlled gasification of a char with CO₂ gas at high temperature (800 – 1000 °C)

(3.2) Chemical activation

KOH or NaOH activation is the most often used chemical for activating biomass-derived carbons. In a general view, the development of a large surface area and high porosity in KOH-activated carbons is the result of the synergistic, comprehensive actions, including chemical activation and carbon lattice expansion by metallic K intercalation. The reactions of KOH and NaOH are shown as follows:



ZnCl₂ activation is another commonly used chemical activation agent for converting biomass-derived carbons into porous ACs. It acts as a dehydrating agent during the activation process and it also has a deoxygenation effect at high temperatures by removing oxygen in the form of water. The reactions of ZnCl₂ is shown as follows:



Moreover, microwave-induced activation is another activation approach. It combines between physical and chemical activations (called “physiochemical activation”)

2.4.2 Pseudocapacitive effect of heteroatoms in the carbon network

A significant enhancement in capacitance can also be obtained by using different types of faradaic reactions based on the oxygen and nitrogen content in the carbon network. Pseudocapacitive effects relate to the rapid faradaic reactions of appropriate functional groups and modification of electronic structure by the doped carbon.

1) Oxygen-doped carbons

The improvement of capacitance can be obtained from the oxygenated function in the carbon network owing to additional pseudo-capacitance as well as conductivity improvement. Examples of the oxygenated functionalities are O–C–O in carboxylic, O–C–O/C–OH in ester or phenol, and C=O in carbonyl/quinone. The content of oxygen functional groups included in each AC is different.

2) Nitrogen-doped carbons

Nitrogen is the heteroatom in the carbon network. Nitrogen can replace carbon (so-called “lattice nitrogen”), and bonds in the functional groups (so-called “chemical nitrogen”) at the edge of aromatic ring structural units, as shown in Figure 2.6 [8]. Examples of the nitrogenated functionalities are pyridinic nitrogen (N-6), pyrrolidonic nitrogen (N-5), quaternary nitrogen (N-Q), and oxidized nitrogen (N-X), respectively. The N-X content can improve electronic conductivity and enhance capacitance by the wettability properties.

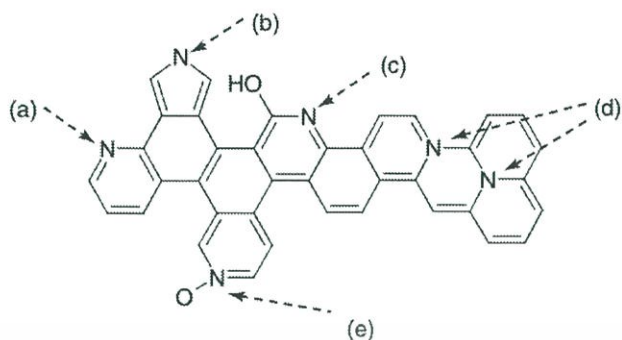


Figure 2.6 Nitrogenated functional groups in the carbon network (a) pyridinic (N-6); (b) pyrrolic (N-5); (c) pyridonic (N-6) (d) quaternary (N-Q); and (e) oxidized nitrogen (N-X) [8].

Normally, N-5 and N-6 lie at the edges of the graphene layer, where a nitrogen atom is bonded to two carbon atom, and can induce pseudocapacitance property. According to, N-5 and N-6 has a lone electron pair in the plane of ring as the acceptor and can accept the donors, causing the faradic reaction for contributing to pseudocapacitance as shown in Figure 2.7 [14]. In the case of N-Q group, nitrogen atom takes the position inside an aromatic ring (so-called graphitic N) with sp^2 hybridization and saturated bonding, enhancing the electrical conductivity of carbon materials as displayed in Figure 2.6. The N-X is oxidized pyridine nitrogen atom, providing positively charge. ACs obviously improve

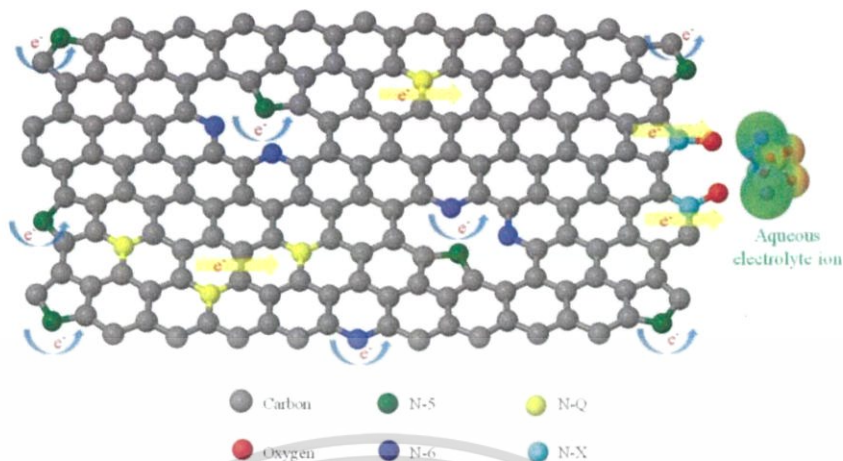
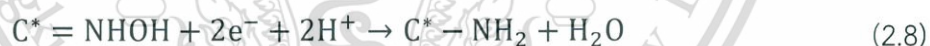


Figure 2.7 Schematic view of the effect of the properties of the N-5, N-6, N-Q and N-X on the charge transfer resistance [14].

The enhancement of capacitance with the nitrogen content in aqueous electrolyte (H_2SO_4) is explained by pseudo-redox reactions owing to the nitrogenated functional group as shown in equations (2.7) and (2.8) and Figure 2.8:



Where C^* stands for the carbon network.

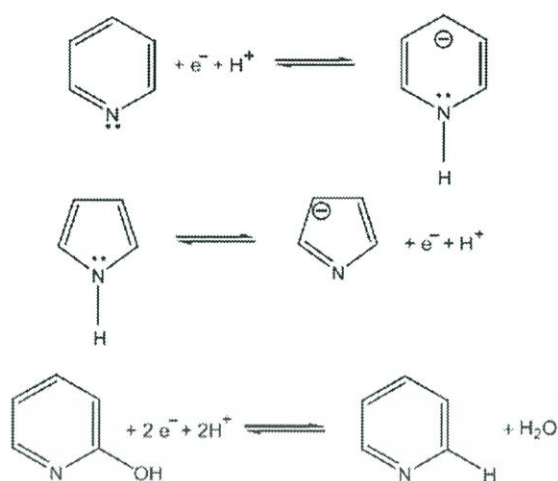


Figure 2.8 Scheme of a possible redox reaction related with pyridinic, pyrrolic and pyridone types [8]

2.4.3 Literature reviews on pseudocapacitive effect of heteroatoms-doped electrodes

Table 2.6 summarizes the capacitive performance of the previous works based on ACs derived from biomass precursors and compares effect of nitrogen doping. ACs without nitrogen doping can achieve high specific capacitance due to their high surface area. In contrast, nitrogen-doped ACs can achieve high specific capacitance, even their low surface area. Possible explanation for an increase in the capacitance of the nitrogen-doped ACs is the faradic reaction of the heteroatom-containing functional groups. The nitrogen-doped ACs can be obtained either by post-treating carbon materials with nitrogen-based gases such as ammonia or chemical reagents or self-doped nitrogen using nitrogen-containing precursors. However, post treatment method is complex, toxic and high cost.

Table 2.6 Literature reviews of supercapacitor based on ACs derived from biomass

Precursors	Activation method	SSA (m^2g^{-1})	N (wt.%)	C (Fg^{-1})	Ref.
Banana fiber	ZnCl ₂	1097	-	296	[22]
Bamboo	KOH	1293	-	67	[23]
Coconut shell	ZnCl ₂	1874	-	276	[24]
Potato starch	KOH	2342	-	335	[25]
Sunflower seed shell	KOH	2509	-	311	[26]
Melamine	KOH	1059	5.5	289	[27]
Broussonetia papyrifera	KOH	1759	1.7	320	[28]
Nut brown	KOH	1463	3.3	363	[29]

SSA: Specific surface area, C_s: specific capacitance

Thus, a simple method that can promote industrial production is required. Recently, the ACs derived from agricultural wastes have been focused, including *in situ* doping using heteroatom-enriched biomass as raw materials with its benefit in terms of renewable, abundant, and environmentally friendly resources. For example, nitrogen self-doped ACs are successfully synthesized from animals, such as silkworm cocoons, gelatin, endothelium corneum gigeriae galli, animal bone, yogurt, and plant biomass waste such as tobacco rods, green leaves, elm flower and bamboo shoot as shown in Table 2.7. Moreover, the source of nitrogen in animals comes from an amino acid, which is related to protein composition. In case of the origin of nitrogen in the plant may come from chlorophyll, which is associated with the green pigment found in the chloroplasts of plants, offering nitrogen self-doped ACs. However, the microstructure and the element composition of resulting ACs largely depend on the

This material is reserved for educational use only, not allowed for commercial use.

raw materials. Thus, by selecting appropriate raw materials, the ACs with a controlled microstructure and a desired amount of heteroatoms could be obtained.

Table 2.7 Literature reviews of nitrogen self-doped ACs derived from biomass

Precursors	Activation method	SSA ($\text{m}^2 \text{g}^{-1}$)	N (wt.%)	C_s (F g^{-1})	Ref.
Silkworm cocoon	KOH	3386	0.58	263	[30]
Gelatin	NaOH	3012	0.82	385	[31]
Endothelium corneum gigeriae galli	KOH	2149	0.70	198	[10]
Yougurt	KOH	1300	1.2	225	[12]
Tobacco rod	KOH	2097	1.41	286	[32]
Green leaves	NaOH	2664	2.32	98	[14]
Elm Flower	KOH	2048	2.63	275	[33]
Bamboo shoot	KOH	972	3.6	412	[34]

SSA: Specific surface area, C_s : specific capacitance

Table 2.8 summarizes comparison of nitrogen-doped ACs by post treatment and self-doped methods. The post treatment method uses nitrogen source such as urea ($\text{CH}_4\text{N}_2\text{O}$) and ammonium (NH_3). The nitrogen content of ACs prepared by the post-treatment method is high level but the process is complicated. On the other hand, the nitrogen self-doped method uses nitrogen-containing raw materials. Example

This material is reserved for educational use only, not allowed for commercial use.

Forbidden to modify the content, and cite the document when use.

of raw materials are chemical components such as melamine and polyacrylonitrile (PAN), and biomass. However, the chemical compounds are toxic and not sustainable material. Thus, biomass-derived nitrogen-doped ACs are attractive. Nevertheless, the nitrogen content is still low due to a low nitrogen content of raw material and a loss of nitrogen during preparation process. Thus, it is require to explore an appropriate biomass with a high nitrogen content and prepare by an effective method.

Table 2.8 Comparison of nitrogen-doping methods

	Method	N-content (at%)	Process complexity	Sustainable material
Post treatment	Post doping (CH ₄ N ₂ O, NH ₃)	2.9 – 7.8	X	X
Self-doped	N-containing chemicals (Melamine, Polyacrylonitrile (PAN))	2.5 – 6.3	O	X
	N-containing biomass	0.7 – 2.8	O	O

O = Good, X = Bad

CHAPTER 3

ANALYTICAL METHODS

3.1 Characterization of electrode materials

Electrode materials synthesized in this research were investigated by techniques and equipment as shown in Table 3. 1

Table 3. 1 Characterization techniques and their corresponding information

Techniques	Information
Scanning electron microscope (SEM; HITACHI SU5000)	Morphology
Transmission electron microscope (TEM; JEOL JEM-2010)	Internal structure
Nitrogen-adsorption isotherms (Micromeritics ASAP 2020)	Surface area, pore volume, pore size distribution
X-ray diffractometry (XRD; Rigaku SmartLab Studio II)	Crystal plane and carbon structure
Raman spectroscopy (Thermo Scientific DXR smart Raman)	Carbon structure
X-ray photoelectron spectroscopy (XPS; PHI Quantera II)	Chemical composition

3.1.1 Scanning electron microscopy

Scanning electron microscopy (SEM) is one of the techniques used to analyze the morphology of sample that backscatter, or secondary electrons are scanned on the sample and detected to create image of the sample. A schematic diagram of SEM is shown in Figure 3.1. In this work, SEM images were measured by a HITACHI S-4700 scanning electron microscope, which was operated at an acceleration voltage of 10 kV.

This material is reserved for educational use only, not allowed for commercial use.

Forbidden to modify the content, and cite the document when use.

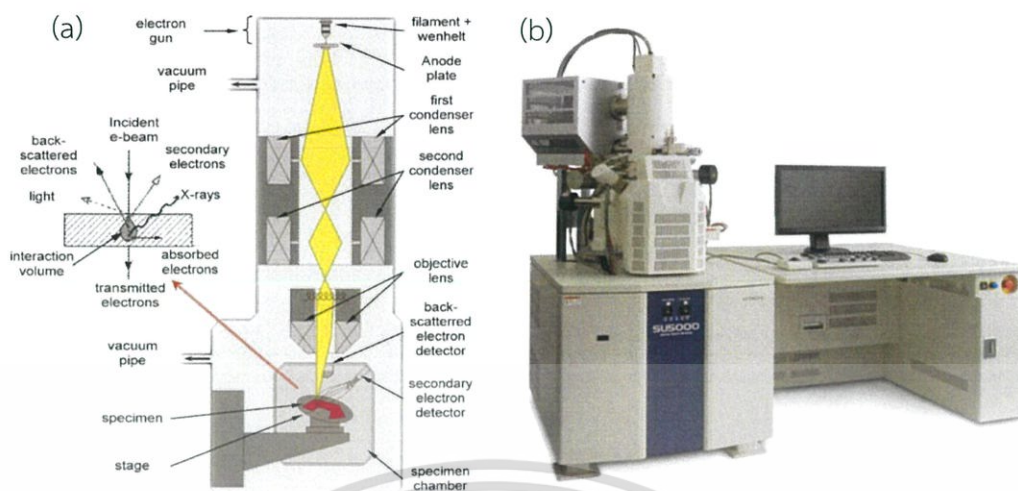


Figure 3.1 (a) Schematic diagram of SEM and (b) A photograph of scanning electron microscope (SEM, HITACHI SU5000) [35]

Sample for SEM observation was prepared as follows:

1. Activated carbons (ACs) powder was dried at 100 °C overnight in oven
2. Carbon tape was attached to SEM sample holder and ACs powder was slightly dropped on carbon tape

3.1.2 Transmission electron microscopy

Transmission electron microscopy (TEM) is used to characterize the internal structure at the high resolution. Information about the crystal structure and morphology can be obtained by a combination of electro optical imaging. The principle of TEM, the electrons are focused with electromagnetic lenses and the image is obtained on a fluorescent screen, or recorded on film or digital camera as shown a schematic diagram of TEM in Figure 3.2a. In this work, TEM images were obtained by a JEOL JEM-2010 transmission electron microscope operated at an accelerated voltage at 200 kV with LaB₆ filament.

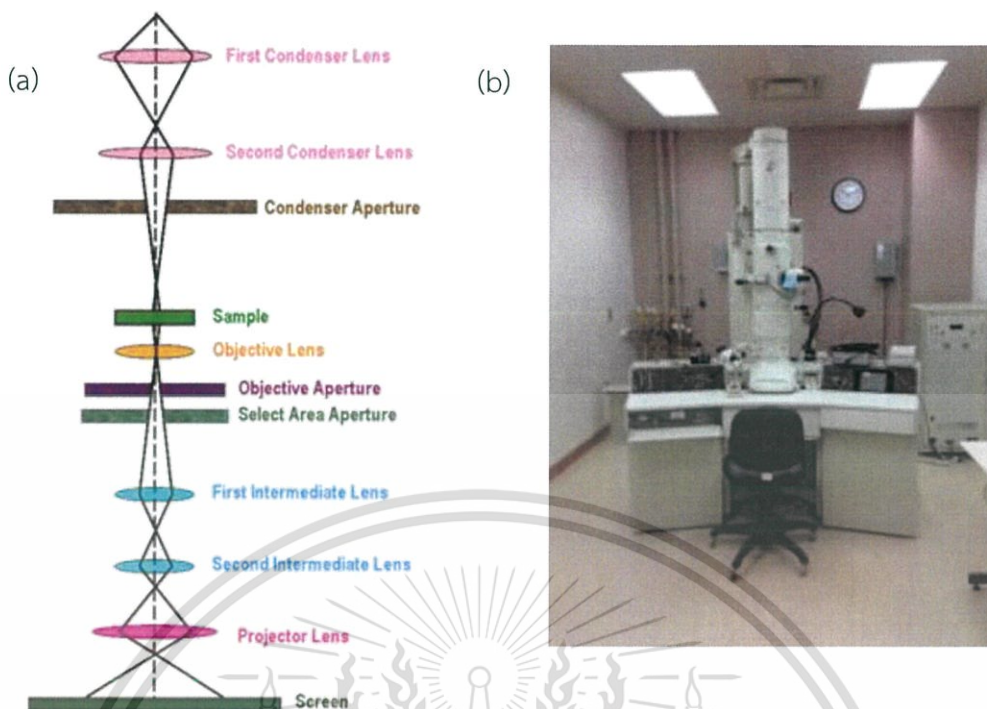


Figure 3.2 (a) Schematic diagram of TEM and (b) A photograph of transmission electronic microscopy (TEM; JEOL JEM-2010) [36]

Sample for TEM observation was prepared as follows:

1. ACs must be in fine powder size. ACs were dried at 100 °C overnight in oven
2. ACs were dispersed into liquid media such ethanol and sonicated for approximately 5-10 mins
4. 1-2 drops of AC dispersion were dropped on the carbon coated copper grid (C-coated Cu grid) with carbon side up
5. Cu grid was dried at least overnight in the designator for completely drying sample

3.1.3 Nitrogen-adsorption isotherms

The adsorption isotherm is used to describe the relationship between amounts of the adsorbate on the adsorbent as a function of its pressure (in case gas) at a constant temperature. Basically, adsorption can be classified into two types, This material is reserved for educational use only, not allowed for commercial use.

Forbidden to modify the content, and cite the document when use.

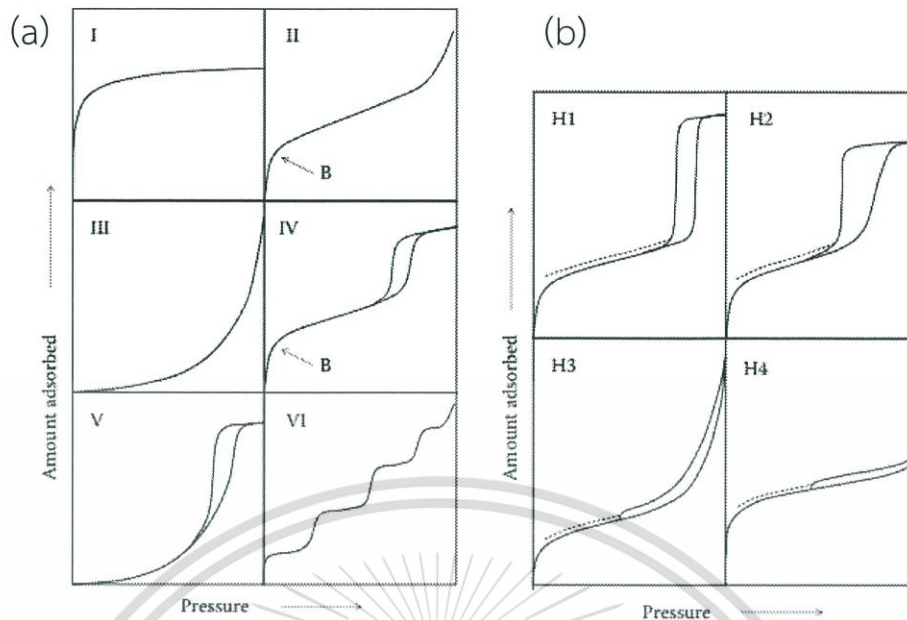


Figure 3.3 (a) Types isotherm and (b) hysteresis loops of gas adsorption [37]

physisorption and chemisorption between adsorbent and adsorption. For chemisorption, the process involved specific chemical interaction between adsorbent and adsorption which is reversible. In contrast, physisorption process is reversible due to its nature as dispersion force, repulsive force, polarization and electrostatic force. The different types of adsorbents (carbon materials, anodic aluminum oxide, zeolites, etc.) give the different shapes of physical adsorption isotherms. The physical adsorption isotherms can be classified into six groups as shown in Figure 3.3a.

- I. Type I isotherms are microporous solids pore characteristics. They are related to small external surface area of adsorbents such as activated carbons. They are obtained by gases and vapors on activated carbons.
- II. Type II isotherms are explored for macroporous and nonporous adsorbents, such as graphite, nanotubes and carbon blacks. The unlimited monolayer-multilayer adsorption was displayed in type II

isotherms. The point B indicates that the stage of the monolayer is completed, and the multilayer adsorption begins.

- III. Type III isotherms are irregular and characteristic of very weak adsorbate-adsorbent interaction. These are also typical of cooperative adsorption e.g. adsorption of water vapor on graphitized carbon blacks.
- IV. Type IV isotherms show the existence of a hysteresis loop owing to the capillary condensation on the mesopores. They are adsorbent characteristics that have a large proportion of mesopores such as the preparation of nanostructured carbons by using mesoporous silica as templates.
- V. Type V isotherms are associated with the type III isotherms. There are characteristics of weak adsorbate-adsorbent interaction such as water vapor adsorption on charcoal.
- VI. Type VI isotherms are typical of adsorbents with a very uniform nonporous surface. An adsorbed monolayer is presented in each step of staircase characteristics such as noble gas adsorption on graphitized carbon black.

The hysteresis loops are classified by the IUPAC as different types of four groups (H1, H2, H3, and H4) as shown in Figure 3.3b. In case of H1, adsorption and desorption branches are almost vertical and nearly parallel over a range of gas upstake. On the other hand, H4 shows the adsorption and desorption branches being horizontal and parallel over a wide range of relative pressures.

Adsorption theories and analysis methods

- Principles of BET

Brunauer, Emmett, and Teller developed the principles of BET. Langmuir proposed the kinetic model of adsorption and described the multilayer

This material is reserved for educational use only, not allowed for commercial use.

Forbidden to modify the content, and cite the document when use.

adsorption. At the low pressure, molecules start to adsorb onto the surface due to Langmuir adsorption isotherm at the low pressure. As the pressure is increased, next molecules will adsorb to pre-absorbed molecules, resulting in a multilayer formation.

$$\frac{P}{V(P_0 - P)} = \frac{1}{V_m C} + \frac{(C - 1)P}{V_m C P_0} \quad (3.1)$$

where V : volume of adsorbed vapor at standard temperature and pressure (STP)

V_m : the monolayer capacity at STP

P : the partial pressure of the adsorbate

P_0 : the saturation vapor pressure of the adsorbate

C : the BET constant

From equation 3.1 gives a linear relation between $P/V(P_0 - P)$ and P/P_0 , with the slope equal to $(C-1)/V_m C$ and with $1/V_m C$ as the interception with Y-axis. As the point B in type II isotherm becomes sharper, that is the interactions between the adsorbate and the adsorbent are stronger.

The specific surface area (SSA) of the adsorbent can be calculated from the adsorption data. The SSA of the adsorbent shown in $\text{m}^2 \text{g}^{-1}$ is

$$SSA = V_m A_m N_A 10^{-18} \quad (3.2)$$

Where N_A : The Avogadro constant.

V_m : The monolayer capacity (mol g^{-1})

A_m : The cross-sectional area of the adsorbed molecule (nm^2)

Figure 3.4 shown an equipment.



Figure 3.4 Micromeritics ASAP 2020 series gas adsorption systems [37]

Sample for nitrogen adsorption-desorption isotherms was prepared as follows:

1. Activated carbon (AC) powder was dried at 100 °C overnight in oven furnace.
2. The bare tube was weighed and recorded the data. After that, the 20 g ACs was loaded into the tube. The ACs-loaded tube was weighed and recorded the data again.
3. The ACs-loaded tube was inserted into the degassing channel. The ACs were degassed at 350 °C for 12 hours prior to nitrogen adsorption measurement.
4. The ACs-loaded tube was weighed again after degas process and recorded the data. After that, it was loaded into the nitrogen adsorption channel.

3.1.4 X-ray diffraction

X-ray diffraction (XRD) is a technique used to analyze the crystal structure of materials as shown in a schematic diagram in Figure 3.5. The XRD analysis is based on constructive interference of monochromatic X-ray and a crystalline sample. X-rays

This material is reserved for educational use only, not allowed for commercial use.

Forbidden to modify the content, and cite the document when use.

are generated by cathode ray tube and accelerated to the sample. XRD result is produced the constructive interference of a monochromatic beam of X-rays diffracted at specific angle by lattice planes separated by the interplanar distance (d) which correspond to Bragg's law in equation (3.3).

$$n\lambda = 2d\sin\theta \quad (3.3)$$

where n is a positive integer, λ is a wavelength of incident X-ray, d is an interplanar distance of lattice, θ is a scattering angle

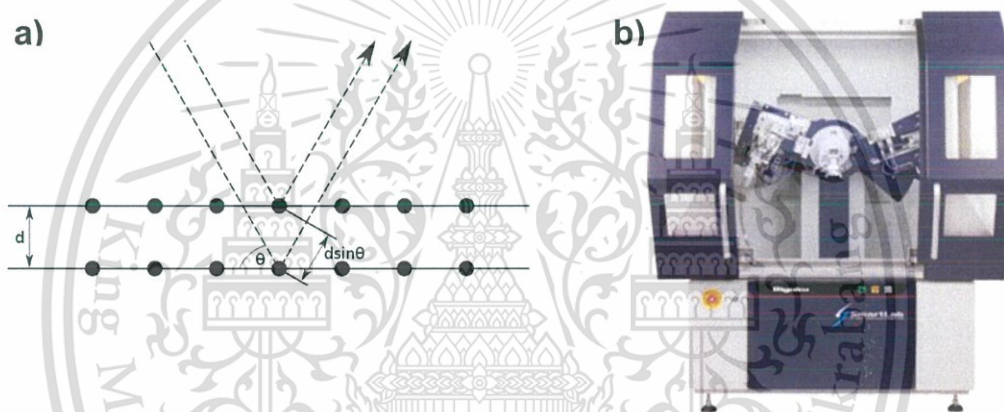


Figure 3.5 (a) A schematic principle of XRD and (b) A photograph of X-ray diffractometry (XRD; Rigaku SmartLab Studio II) [38]

Sample for XRD characterization was prepared as follows:

1. The ACs must be in fine powder size and dried at 100 °C overnight in oven
2. The glass slide holder was cleaned by ethanol.
3. The AC powder was prepared by slightly dropping the ACs powder onto the glass slide holder. The ACs powder was pressed by using another glass slide to make a smooth surface.

3.1.5 X-ray photoelectron spectroscopy

One of the most important technique for surface analysis of the chemical state of the elements is X-ray photoelectron spectroscopy (XPS). The basic principle of this technique is based on the photoelectric effect. When a beam of X-rays is conducted to the sample, the photon energy is transferred to the electron. Then, the electron gains energy to remove from the surface of the sample, called photoelectron. Figure 3.6 shows the schematic diagram of basic principle of XPS. For binding energy of the core level electron (E_b) calculated using the following equation:

$$E_b = h\nu - E_k - \phi \quad (3.4)$$

where $h\nu$ is the X-ray photon energy, E_k is the kinetic energy of the photoelectron and ϕ is the work function of the spectrometer (4-5 eV). The common X-ray source consists of two types; 1486.6 eV of Al $K\alpha$ and 1253.6 eV of Mg $K\alpha$. The average depth of surface analysis is approximately 5 - 10 nm. Consequently, the electron binding energy offers the identification of various elements. XPS can detect all elements except hydrogen. However, the electronic environment of the atom affected to the electron binding energy. Since, an atom is bonded to another atom of element, leading to a different electronegativity and changing the electron binding energy. The change of binding energy is the chemical shift, which can be used to identify chemical information of compound.

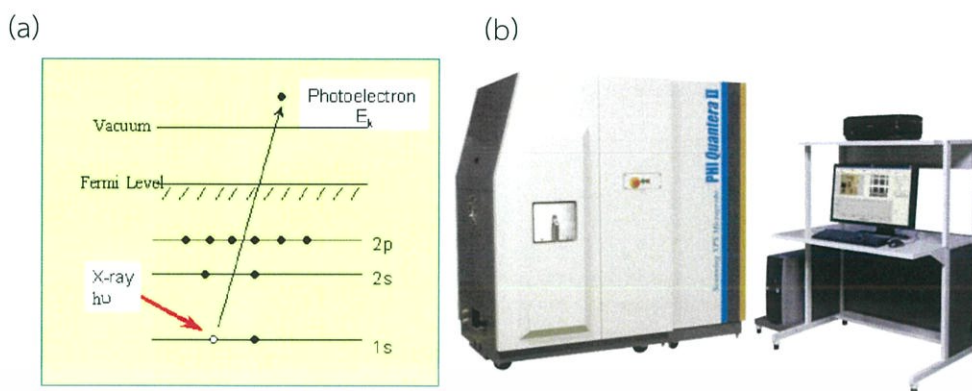


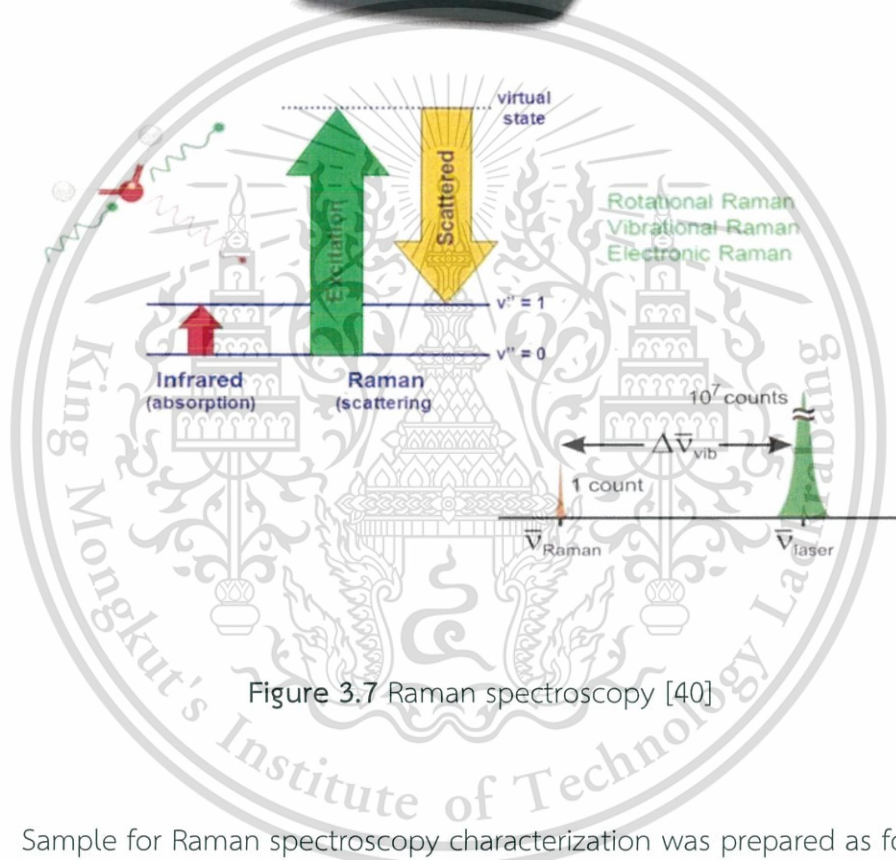
Figure 3.6 (a) A schematic diagram of basic principle of XPS and (b) A photograph of X-ray photoelectron spectroscopy (XPS; PHI Quantera II) [39]

Sample for XPS characterization was prepared as follows:

1. The ACs powder was dried at 100 °C overnight in oven
2. ACs powder was slightly dropped on carbon tape

3.1.6 Raman spectroscopy

Raman spectroscopy techniques is used to analyze carbon structure. This technique is based on the inelastic scattering, or Raman scattering of monochromatic light. Normally, the light is a laser source in the visible near infrared range Inelastic scattering in monochromatic light imply that the frequency of photons changes interaction with the sample, resulting in the energy being shift up or down. The shift in energy provides information about the vibrational modes. In the research used the Raman spectra from Thermo Scientific DXR smart Raman with a 532 nm laser source as shown in Figure 3.7.



Sample for Raman spectroscopy characterization was prepared as follows:

1. The ACs powder was dried at 100 °C overnight in oven
2. The ACs powder was slightly dropped on the sample holder

3.2 Characterization of electrochemical properties

Measurement of electrochemical properties was operated in a three or two electrode cell to an electrochemical workstation by Metrohm AUTOLAB PGSTST 302.

Table 3.1 showed electrochemical measurement technique



Table 3.1 Electrochemical techniques

Measurement techniques	Information
Cyclic voltammetry (CV)	<ul style="list-style-type: none"> - A quick determination of the domain of electroactivity - The number of active redox couples - The electrochemical reversibility - The capability and the cyclability
Galvanostatic charge/discharge (CD)	<ul style="list-style-type: none"> - The determination of the capacity - The faradic reversibility - The ohmic drop - The cyclability
Electrochemical impedance spectroscopy (EIS)	<ul style="list-style-type: none"> - The estimation of cell resistance - The kinetic parameters - The assessment of porous electrodes

3.2.1 Cyclic voltammetry

Cyclic voltammetry (CV), is one of the commonly used electrochemical measurement techniques with the advantage of ability to characterize an electrochemical system. In CV measurement, the potentiostat applies a potential to the working electrode with specific scan rate then reverses the scan, returning to the initial potential (see triangular wave from in Figure 3.8). The slope of the linear lines is called the potential (V) scan rate(v):

$$v = \frac{dV}{dt} \quad (3.5)$$

where V is expressed in V units and v is in $V.s^{-1}$. The potential–time plot can be expressed as:

$$V(t) = V_0 + vt \text{ for } V \leq V_1 \quad (3.6)$$

This material is reserved for educational use only, not allowed for commercial use.

Forbidden to modify the content, and cite the document when use.

$$V(t) = V_0 - vt \text{ for } V \leq V_2 \quad (3.7)$$

Where V_1 and V_2 are the two voltage boundaries.

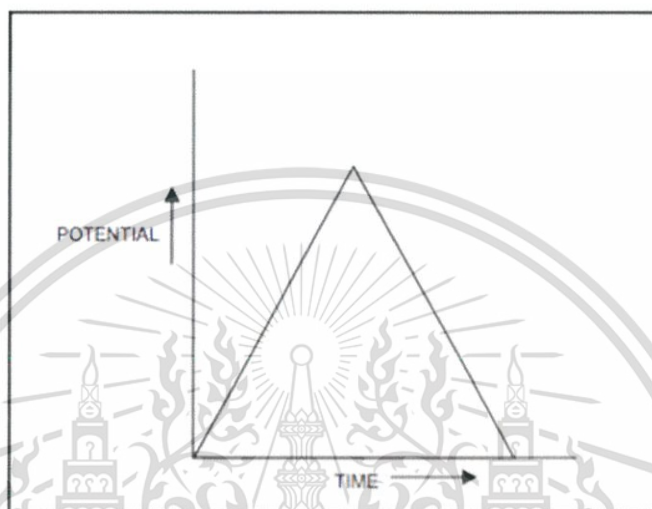


Figure 3.8 Typical V-t curves in cyclic voltammetry [15]

During the potential sweep, the potentiostat measures the current result obtained from each applied potential. These values are collected then plot into CV graph of squared i-V curves which is obtained for such supercapacitor. Figure 3.9 is shown the example of CV graph.

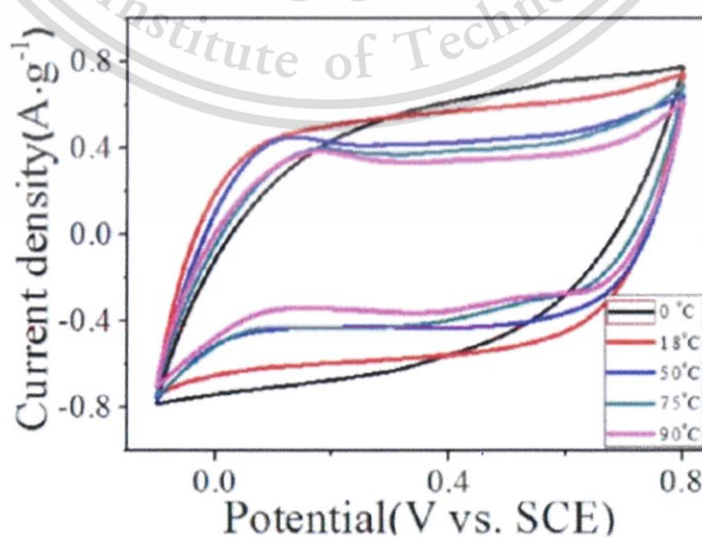


Figure 3.9 The example of cyclic voltammetry graph plot

This material is reserved for educational use only, not allowed for commercial use.

Forbidden to modify the content, and cite the document when use.

For the specific capacitance (C_s), can be calculated from the CV curve that obtained from the electrochemical measurement with equation 3.8

$$C = \frac{\int_{V_1}^{V_2} i(V) dV}{2(V_2 - V_1)mv} \quad (3.8)$$

where C_s is the specific capacitance ($F g^{-1}$), m is the weight of the electrode (g), v is the scan rate of CV curves ($V s^{-1}$), and $(V_2 - V_1)$ represents the potential window (V). Normally, the CV curve from EDLC is plotted as the rectangular shape while the pseudocapacitor generates with the additional redox reaction as oxidation and reduction peaks.

3.2.2 Galvanostatic charge-discharge (CD)

Galvanostatic charge-discharge (CD) technique is used to test the performance and cycle-life of EDLCs and is very different from cyclic voltammetry. According to the current is controlled and the voltage is measured. This method gives access to different parameters such as capacitance, resistance and cyclability. The voltage variation is described following below:

$$V(t) = Ri + \frac{t}{C}i(V) \quad (3.9)$$

Charge and discharge are conducted with constant current until reach the set voltage. The loop is repeated in cycle times to observe repeatable and the cycle-life time before performance is drop. The example of CD curve is shown in Figure 3.10.

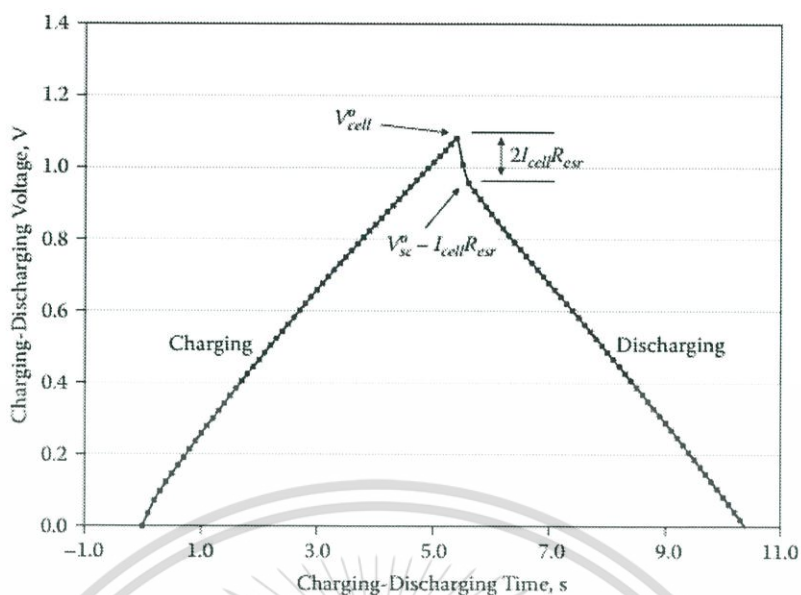


Figure 3.10 Galvanostatic charge-discharge curve [15]

The capacitance of a supercapacitor can be calculate from slope of the curve;

$$C = \frac{I\Delta t}{\Delta V} \quad (3.10)$$

where I is the set current, Δt is the discharge time, and ΔV is the voltage window.

The series resistance (R) is deduced from the voltage drop (V_{drop}) occurring over the current inversion (Δt);

$$R = \frac{V_{drop}}{\Delta I} \quad (3.11)$$

Generally, CD curve of the EDLC shows with triangular repeatable charge-discharge curve, whereas the pseudocapacitor shows with quasi-triangular representing the additional discharge time from redox reaction.

3.2.3 Electrochemical impedance spectroscopy (EIS)

Analysis based on electrochemical impedance spectroscopy (EIS) can be explained the resistance and capacitance of supercapacitor. In EIS measurement, voltage is carried out at several frequency (f) for impedance measurement. Figure 3.11 shows the Nyquist plots of supercapacitor. The EIS spectra consists of two main parts: firstly, a semicircle at the high-frequency (HF) region which relates to the series resistance (R_s) and the charge-transfer resistance (R_{CT}), and secondly, a nearly linear at the low-frequency (LF) region that corresponds to the diffusion controlled process.

- The series resistance (R_s) is the sum of the intrinsic resistance of the electrode material, the electrolyte resistance and the contact resistance between the electrode material and the current collector.
- The charge-transfer resistance (R_{CT}) is the diameter of the semicircle, implying the kinetic resistance to the ion transfer.
- The nearly vertical linear at LF region shows a straight line, indicating the ion diffusion rate at the interface between the electrode-electrolyte materials.

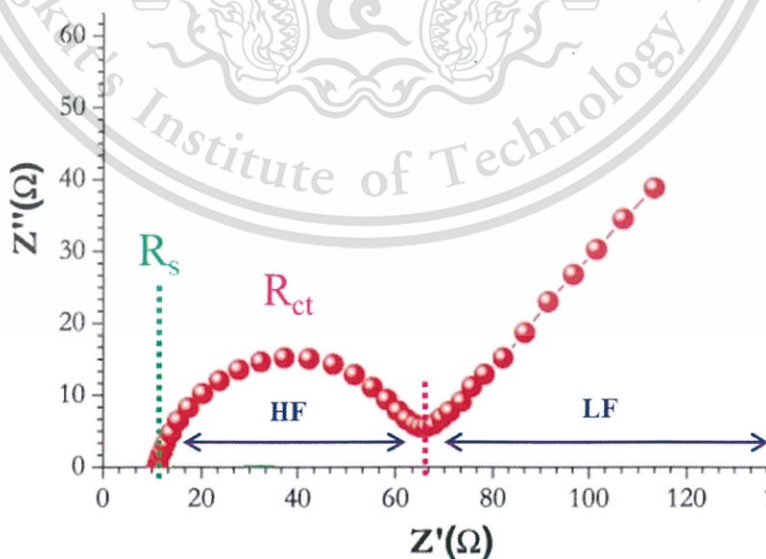


Figure 3.11 Nyquist plot of supercapacitor

This material is reserved for educational use only, not allowed for commercial use.

Forbidden to modify the content, and cite the document when use.

Practical analysis of pseudocapacitors by EIS must also consider the effects of porous structures present in some pseudocapacitive materials. Morphologies will exhibit Warburg diffusion regions (45° phases) or LF similar to those seen in porous double-layer devices. The region is induced by distribution of different resistance and capacitance between pores in the system at different sizes and distances from the collector.

3.2.4 Energy and power density

The energy density (E , $W\ h\ kg^{-1}$) of supercapacitor can be expressed as a quantity per unit weight (specific energy or power) or per unit volume. The energy (E) stored in a capacitor is related to the charge Q (C), at each interface and the potential difference V (V), and therefore is directly proportional its capacitance as exhibited in equation:

$$E = \frac{1}{2} CV^2 \quad (3.12)$$

Maximum energy is achieved when V is at a maximum, which is usually limited by the breakdown strength of the dielectric.

The second important parameter for characterizing supercapacitor is their power density. Normally, power density (P) is the rate of energy delivery per unit time. The resistance of the internal components of the capacitor (e.g., current collectors, electrode materials, dielectric/electrolyte, and separator) needs to be considered to determine P for a certain capacitor. The resistance of these components is usually measured in the total resistance referred to as the equivalent series resistance (ESR) (Ω). The ESR, by introducing a voltage drop, determines the maximum voltage of the supercapacitor during discharge and therefore limits the maximum energy and power of a supercapacitor. The measurement of power for supercapacitor is often measured

at match impedance (i.e., the resistance of the load is assumed to be the same as the supercapacitor ESR) which corresponds to the maximum power P_{max} , given by

$$P_{max} = \frac{V^2}{4ESR} \quad (3.13)$$

However, even though the resistance of a good supercapacitor is typically much lower than that of the connected load, the actual delivered peak, although still very high, is usually lower than P_{max}



CHAPTER 4

NITROGEN SELF-DOPED ACTIVATED CARBON DERIVED FROM SILKWORM PUPAE WASTE AND ITS ELECTROCHEMICAL PROPERTIES

This chapter describes synthesis of nitrogen self-doped activated carbons (ACs) derived from silkworm pupae to enhance energy density. Figure 4.1 shows a flow chart of the experimental procedure, including the morphology, surface area, pore size distribution, and chemical composition characterization.

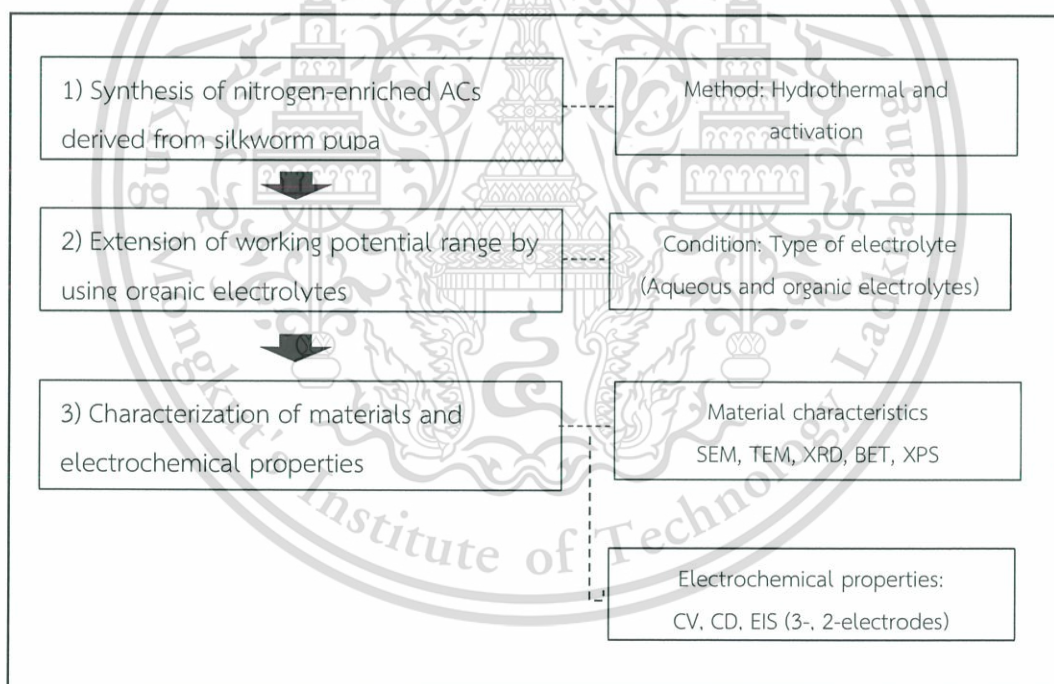


Figure 4.1 Diagram of the synthesis of ACs derived from silkworm pupae

4.1 Synthesis of nitrogen self-doped activated carbons from silkworm pupae by hydrothermal and chemical activation

ACs derived from silkworm pupae were prepared via main three processes as shown in Figure 4.2.

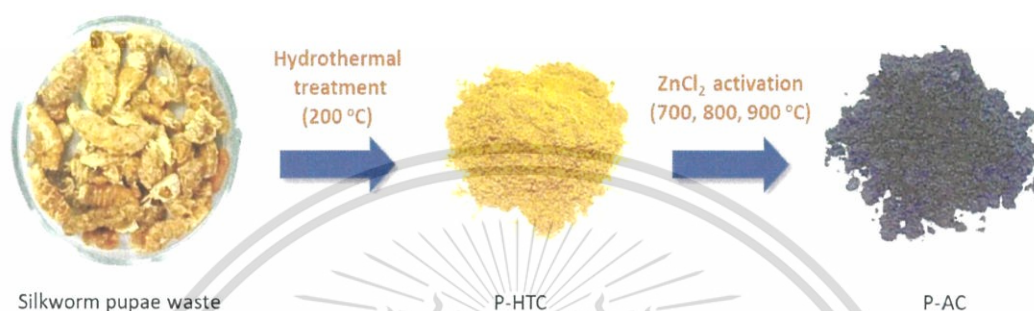


Figure 4.2 Flow chart of ACs synthesis derived from silkworm pupae.

Procedure to synthesize ACs derived from silkworm pupae is as follows:

1) Preparation of raw material:

Silkworm pupae waste was blended after drying and then were ground by ball milling.

2) Hydrothermal process:

The powder pupae were mixed with 1 M acetic acid at a weight ratio of 1:3 and stirred at room temperature for 24 hours. The mixture was kept into a glass-lined (250 ml) stainless steel autoclave for the hydrothermal process at 200 °C for 24 hours as shown in Figure 4.3. Then, the mixture after hydrothermal treatment was washed using ethanol and dried at 120 °C for 24 hours (herein after referred to as P-HTC).

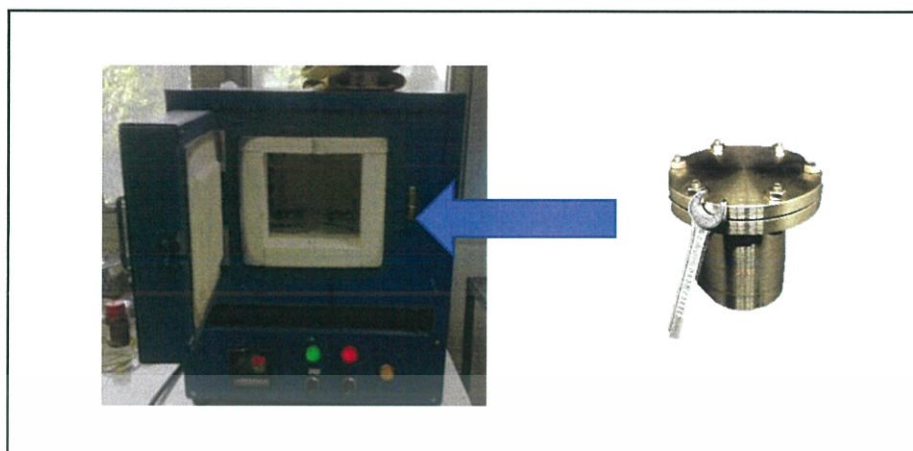


Figure 4.3 Photograph of oven furnace for hydrothermal process

3) Chemical activation process

The P-HTC was mixed with ZnCl_2 (2 g: 6 g) in 15 mL of ethanol and then stirred by a magnetic stirrer for 24 hours. After that, the mixture was loaded to oven furnace at 110 °C for 12 hours. The mixture was activated at different temperatures (700, 800 and 900 °C) under inert gas (N_2 99.999%) with the condition as shown in Table 4.1. After activation, the product was washed with 1 M hydrochloric acid (HCl), and subsequently DI water until it reached a natural pH. The final products were dried at 110 °C overnight and hereinafter referred to as P700, P800 and P900, respectively, corresponding to the activation temperature. The obtained ACs were characterized their morphology, porosity, chemical composition and electrochemical properties.

Table 4.1 Condition of chemical activation process

N_2 Flow rate (mL min^{-1})	Activation time (hour)	Ramping rate of heater ($^{\circ}\text{C min}^{-1}$)	Temperature ($^{\circ}\text{C}$)
300	2	5	700
			800
			900

4.2 Characterization of activated carbon derived from silkworm pupae

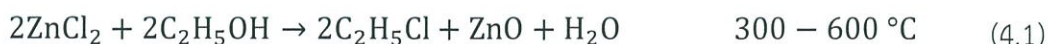
The analytical techniques used for the characterization of electrode materials are shown in Table 4.2.

Table 4.2 Characterization techniques and their corresponding information

Techniques	Information
Scanning electron microscopy (SEM; HITACHI SU5000)	Morphologies structure
Transmission electron microscopy (TEM; JEOL JEM-2010)	Internal structure
Nitrogen-adsorption isotherm (Micromeritics ASAP 2020)	Surface area and pore volume distribution
X-ray diffractometry (XRD; Rigaku SmartLab Studio II)	Crystallinity
Raman spectroscopy (Thermo Scientific DXR smart Raman)	Carbon structure
X-ray photoelectron spectroscopy (XPS; PHI Quantera II)	Chemical composition

4.2.1 Morphology of activated carbon derived from silkworm pupae

Figures 4.4a-d show FE-SEM images of the P-HTC, P700, P800 and P900, respectively. The morphologies of P-HTC and the P-ACs were completely different. The surface of the P-HTC was relatively smooth and nonporous, while those of the P-ACs were rough surface with sponge-like pores. These pores resulted from chemical reaction of ZnCl_2 during activation treatment, remaining empty space in the carbon structure. The chemical reactions are shown in the following equations:



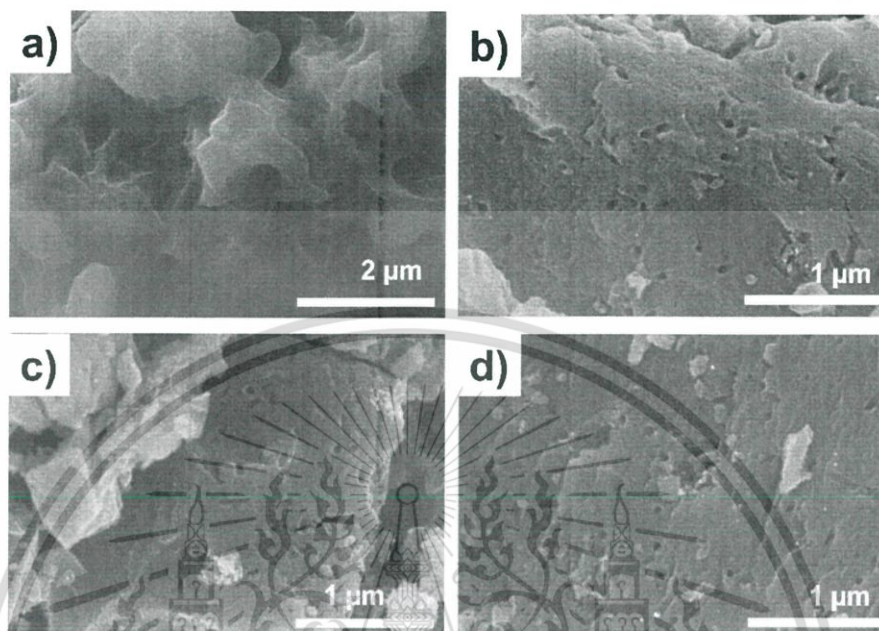


Figure 4.4 FE-SEM images of (a) P-HTC, (b) P700, (c) P800 and (d) P900

4.2.2 Internal structure of activated carbons derived from silkworm pupae

The internal structure of ACs was explored by TEM technique. Figs. 4.5a-d show TEM images of the P-HTC, P700, P800 and P900, respectively. TEM images reveal the bright fringes, indicating the micropore structure of ACs.

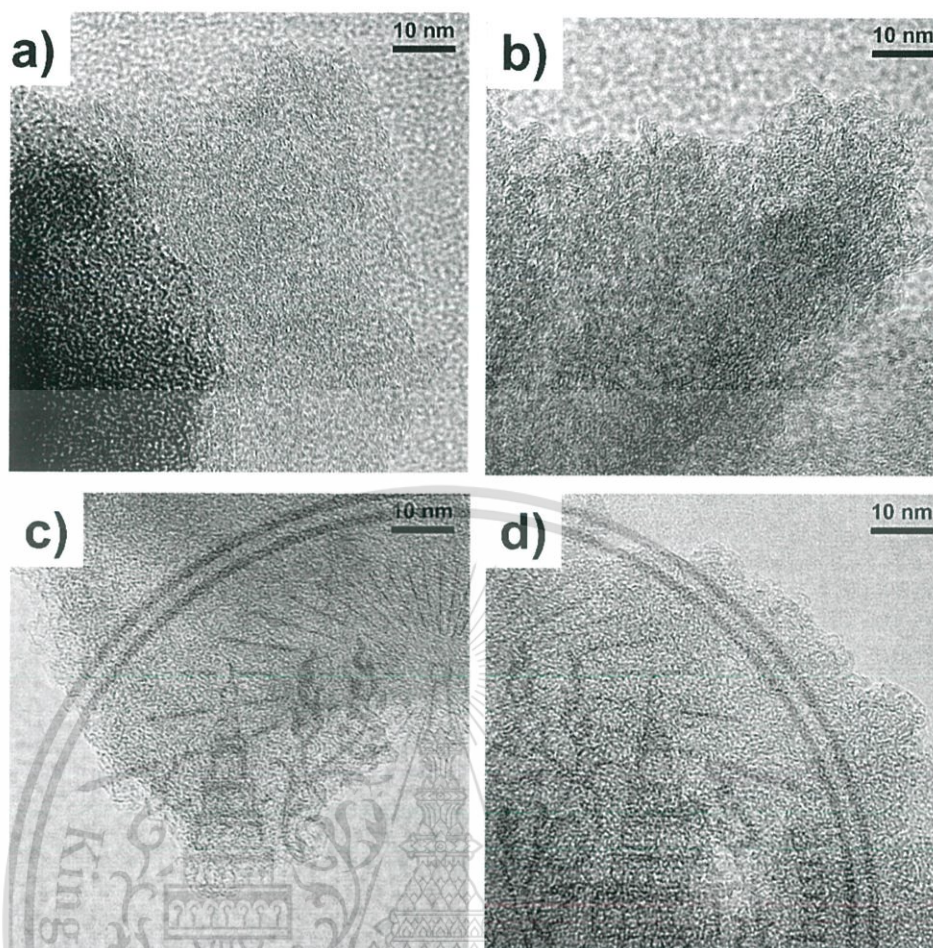


Figure 4.5 TEM images of (a) P-HTC (b) P700 (c) P800 and (d) P900

4.2.3 Surface area and porosity of activated carbon derived from silkworm pupae

N_2 adsorption-desorption isotherms technique was used to analyze the surface area and porosity properties of ACs. N_2 adsorption-desorption isotherms of the P-ACs and YP50 were significantly different, as shown in Figure 4.6a. YP50 showed a sharp N_2 adsorption-desorption isotherms at the low-pressure range with a parallel line to the relative pressure axis at the high-pressure range. The adsorption and desorption branches showed a relatively narrow hysteresis loop, implying Type I isotherms (defined by the IUPAC), indicating microporous solid pore characteristics of YP50.

On the contrary, N_2 adsorption-desorption isotherms of the P-ACs showed a gradual increase of slope at the low-pressure range, and then gradually parallel to the relative pressure axis at the high-pressure range. Moreover, their hysteresis loops were wider than the YP50, classified as the typical Type IV isotherms, indicating mesopore and micropore. The hysteresis loop in the region of the relative pressure between 0.4 – 1.0 of P/P_0 also became larger when the activation temperature increased. These results indicate well-developed mesoporosity of the P-ACs [41].

Figure 4.6b shows the pore size distribution obtained from the DFT method. The summarized data in Table 4.3 shows surface area, pore size, and pore volume of all samples. The pore size distribution of the YP50 displays in the range between 1.0 – 2.0 nm, implying the main component of micropores while the P-ACs show a pore size distribution range of 1.0 – 6.0 nm, containing both of micropores and mesopores. From the results of Table 4.3, the YP50 shows the highest values of S_{BET} ($1336 \text{ m}^2 \text{ g}^{-1}$), the highest ratio of micropore surface area and S_{BET} (S_{micro}/S_{BET}) (0.94) and the highest ratio of micropore volume to the total volume ($V_{\text{micro}}/V_{\text{total}}$) (0.82). In case of the P-ACs, the values of S_{BET} , S_{micro}/S_{BET} and $V_{\text{micro}}/V_{\text{total}}$ of each sample is in the following order: P900 ($1267 \text{ m}^2 \text{ g}^{-1}$, 0.90, 0.78) > P800 ($1187 \text{ m}^2 \text{ g}^{-1}$, 0.87, 0.71) > P700 ($1062 \text{ m}^2 \text{ g}^{-1}$, 0.77, 0.55). These results show that the surface area and micropores of the P-ACs were increased with the higher activation temperature. The average pore size of each samples is in the following order: P700 > P800 > P99 > YP50.

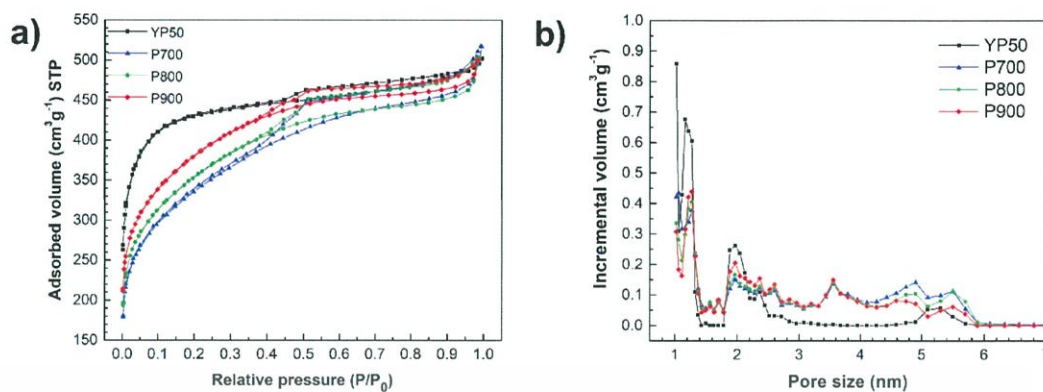


Figure 4.6 (a) N_2 adsorption/desorption isotherms and (b) pore size distribution of all samples

Table 4.3 Surface and porosity properties of all samples

Samples	S_{BET} ($m^2 g^{-1}$) ^a	S_{micro} ($m^2 g^{-1}$) ^b	S_{meso} ($m^2 g^{-1}$) ^b	S_{micro}/S_{BET}	S_{meso}/S_{BET}	Pore Diameter (nm) ^c	V_{total} ($cm^3 g^{-1}$) ^d	V_{micro} ($cm^3 g^{-1}$) ^d	V_{meso} ($cm^3 g^{-1}$) ^d	V_{micro}/V_{total}	V_{meso}/V_{total}
P700	1062	824	238	0.77	0.22	1.54	0.77	0.43	0.34	0.55	0.44
P800	1188	1033	155	0.87	0.13	1.48	0.73	0.52	0.21	0.71	0.28
P900	1267	1142	125	0.90	0.10	1.48	0.73	0.57	0.16	0.78	0.21
YP50	1336	1263	73	0.94	0.05	1.46	0.72	0.59	0.13	0.82	0.17

^a BET specific surface area. ^b Micropore surface area from *t*-plot method. ^c Pore diameter from DA method. ^d Micropore-mesopore volume from DFT method.

4.2.4 Crystallinity of activated carbons derived from silkworm pupae

The crystallinity of the P-ACs and commercial AC (YP50) was characterized by XRD technique in the 2θ range of 10° to 70° . As shown in Figure 4.7, the broad peaks at approximately 23.2° and 44.6° of the YP50 were identified as amorphous carbon. However, the P-ACs show a slight shift from 23.2° to 25.3° , implying a smaller interlayer (0.352 nm) compared to YP50 (0.360 nm). Moreover, the P-ACs showed the sharp peak

at approximately 26.4° , corresponding to the (002) plane of graphitic carbon. These results indicated that a higher graphitic degree of the P-ACs compared to the YP50.

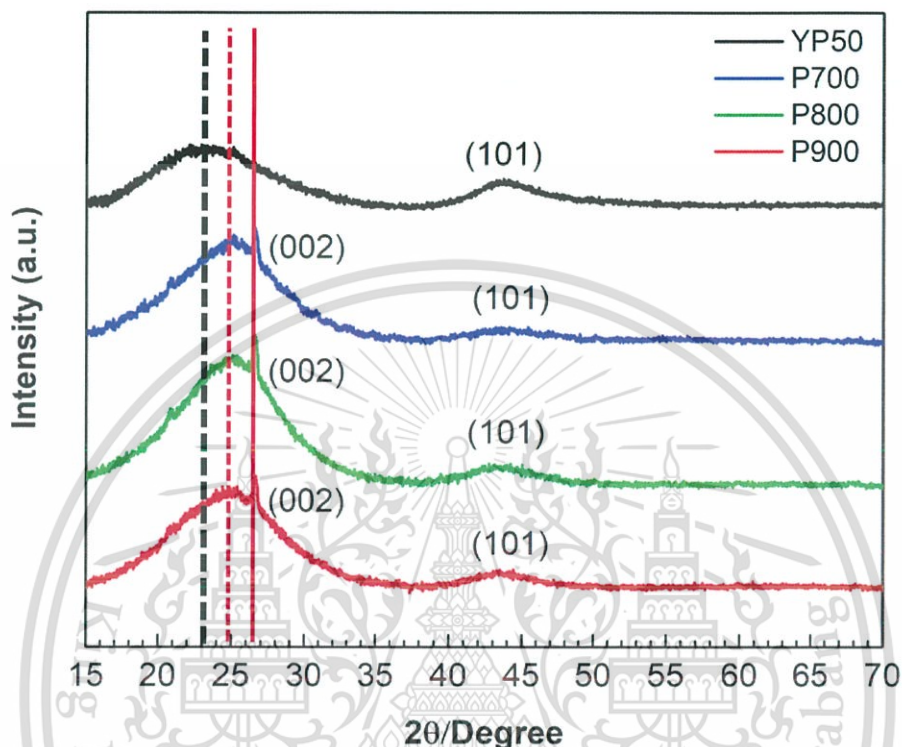


Figure 4.7 XRD diffraction patterns of all samples

Next, carbon structure of all samples was investigated by Raman spectroscopy technique. The Raman spectra of the P-ACs and commercial AC (YP50) were shown in Figure 4.8. Broad peaks indicating as D-band and G-band at Raman shifts of approximately 1350 and 1600 cm^{-1} were observed. Normally, D-band is caused by disordered carbon structures and G-band arises from stretching of the C-C bond in graphitic structures. The intensity ratio of D-band to G-band (I_D/I_G) relates to the ratio of defect sites in carbon materials. The values of I_D/I_G tended to increase when the activation temperature increased (P700 (0.919) < P800 (0.926) < P900 (0.928) < YP50 (0.940)). This indicates that YP50 showed a high content of the defects and disordered structures compared to the P-ACs. This is consistent with XRD results. Among the P-

ACs, P900 with the highest surface area showed the highest I_D/I_G , implying a high content of the defects and disordered structures. A higher surface area, a higher level of discontinuous carbon structures, inducing a formation of disordered structures.

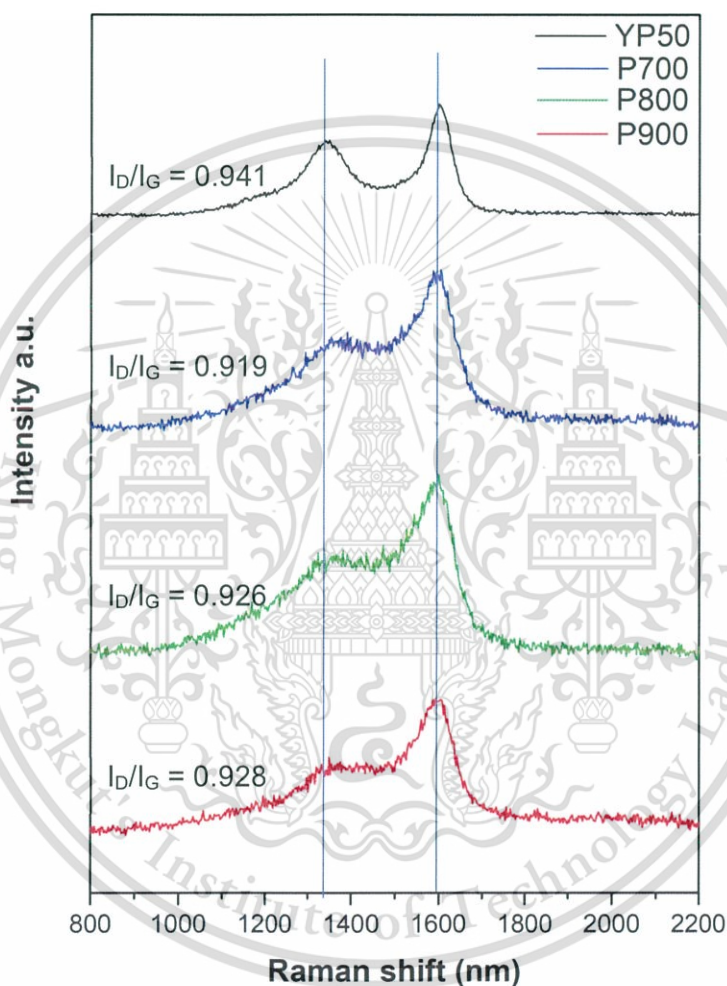


Figure 4.8 Raman spectra of all samples

4.2.5 Elemental composition of activated carbon derived from silkworm pupae

The nitrogen-doped ACs have been determined as one of promising heteroatom-doped materials for supercapacitor applications owing to additional This material is reserved for educational use only, not allowed for commercial use.

Forbidden to modify the content, and cite the document when use.

pseudo-capacitance and conductivity improvement. XPS technique was used to analyze the compositions and chemical states of the elements in the P-ACs. The quantitative analysis of the elemental composition is shown in Table 4.4. The P-ACs consisted of carbon, nitrogen and oxygen elements, while the YP50 found only carbon and oxygen from the XPS-wide scan spectra. The nitrogen content of P700, P800 and P900 was 6.3, 5.2 and 3.8 at%, respectively. The nitrogen content of the P-ACs is in the following order: P700 > P800 > P900. The nitrogen to carbon ratio (N/C) of P700, P800 and P900 was 0.07, 0.06 and 0.04, respectively. Among them, the P700 showed the highest N/C ratio. But the N/C ratio dramatically decreased when the temperature increased to 900 °C.

The N1s spectra of the P-ACs were analyzed to explore the nitrogen-bonding configuration. The N1s spectra obtained from all samples are shown in Figure 4.9a. The high-resolution N1s spectrum can be deconvoluted into four types of nitrogen groups. The peaks can be ascribed to the pyridinic nitrogen (N-6, 398.3 eV), pyrrolic nitrogen (N-5, 399.8 eV), quaternary nitrogen (N-Q, 401.7 eV) and oxidized nitrogen (N-X, 403.6 eV) [42, 43]. The relative peak area of each nitrogen-bonding configuration was calculated and shown in Table 4.4. Interestingly, N-Q shows the highest content. The formation of N-Q may be based on amino acid structure in silkworm pupae. The contents of N-5 and N-6 decreased when the activation temperature increased with the following order: P900 < P800 < P700. Nevertheless, the ratio of (N-Q)/[(N-5) + (N-6)] increased from P700 to P900. These results attributed to the recrystallization of N-Q or graphitic-N from the defective structures to N-5 and N-6 during thermal treatment.

Moreover, the O1s spectra were deconvoluted as shown in Figure 4.9b. Oxygen-containing configurations of all samples are classified into three groups, including O=C–OH (531.2eV) in carboxyl groups, C=O (532.2 eV) in carbonyl groups and C–OH (533.2 eV) in phenol groups and/or C–O–C (533.2 eV) in ether groups. The content of C=O tends to increase when the activation temperature increased. The O content and the oxygen to carbon ratio (O/C) ratio of all samples are shown in Table 4.4. The YP50

shows the lowest O/C ratio. There are no obvious differences in that of the P-ACs. The oxygen contents of the P-ACs are approximately 2-times higher than that of the YP50.

Table 4.4 Chemical composition of all samples evaluated from XPS spectra

Samples	Element content (at%)			O/C ratio	N/C ratio	Relative N1s peak area (at%)						
	C	O	N			N-6	N-5	N-Q	N-X	(N-6)+(N-5)	(N-Q)/[(N-6)+(N-5)]	
YP50	95.56	4.44	-	0.04	-	-	-	-	-	-	-	-
P700	86.50	7.10	6.30	0.08	0.07	1.06	1.74	2.50	1.00	2.80	0.89	
P800	88.40	6.40	5.20	0.07	0.06	1.01	1.44	2.22	0.53	2.45	0.90	
P900	88.80	7.40	3.80	0.08	0.04	0.42	1.14	1.94	0.30	1.56	1.24	

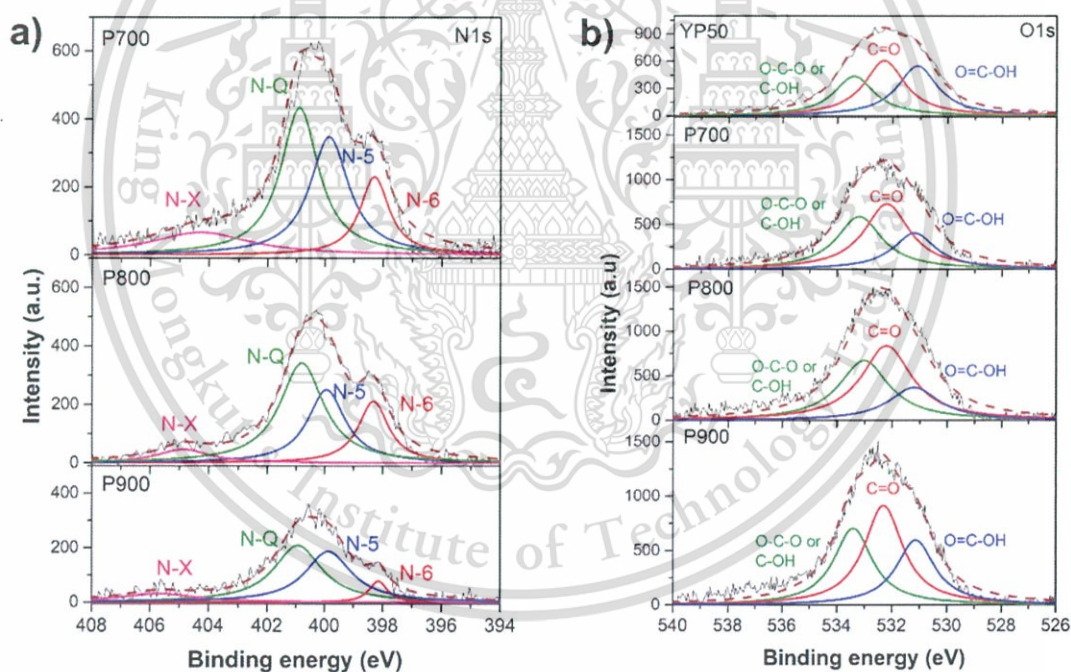


Figure 4.9 (a) N1s and (b) O1s XPS spectra of P-ACs and YP50

4.3 Electrochemical properties of activated carbon derived from silkworm pupae

4.3.1 Electrode preparation

The synthesized ACs was treated at 100 °C in vacuum oven overnight before tablet formation. The AC tablet was prepared by mixing the synthesized ACs, carbon black (CB) and polytetrafluoroethylene (PTFE) at the weight ratio of 90:5:5 in a mortar. After that, the mixture was formed an electrode tablet by pressing under a pressure of 10 kN using a 10-mm diameter mold.

Regarding to characterization of electrochemical properties of electrode material, the AC tablet was attached on Ni foam (MTI, Ni foam for supercapacitor cathode substrate, a thickness of 0.08 mm) using carbon paste and dried at 100 °C for 1.5 hours. To characterization supercapacitor cell, two of the AC tablets were assembled into a coin-cell structure (2032-type coin cell) as cathode and anode electrodes.

4.3.2 Electrochemical measurement systems

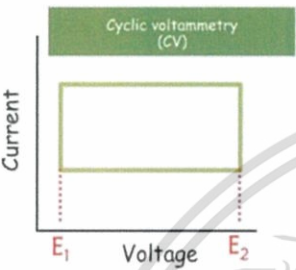

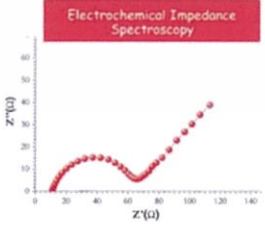
The electrochemical properties of the electrode material and cell based on ACs derived from silkworm pupae were characterized by three- and two- electrode systems (Metrohm AUTOLAB PGSTAT 302). Summary of the test condition based on aqueous and organic electrolytes and the test conditions of electrochemical properties are shown in Tables 4.5 and 4.6, respectively.

Table 4.5 Test condition based on aqueous and organic electrolytes

Detail	Aqueous electrolyte	Organic electrolyte
Electrolyte	1M Na ₂ SO ₄ *	1M TEABF ₄ * in PC
Measurement system	Three-electrode	Two-electrode
Assembly condition	Air	Inert atmosphere (Glove box)
Working electrode	AC electrode on Ni-foam	2-AC electrode in coin cell
Reference	Ag/AgCl	-
Counter electrode	Pt	-
Photograph measurement		

(Na₂SO₄) Sodium sulfate, (TEABF₄) Teraethylammonium tetrafluoroborate, (PC) Propylene carbonate

Table 4.6 Condition measurement of electrochemical properties

Technique	Parameter	Aqueous electrolyte (3-electrode cells)	Organic electrolyte (2-electrode cells)
Cyclic voltammetry (CV) 	Potential window	-0.2 – 0.8 V	0.0 – 2.5 V
	Scan rate	5 mV s ⁻¹	1 mV s ⁻¹
Galvanostatic charge/discharge (CD) 	Current density	0.2 A g ⁻¹	0.02 A g ⁻¹
	Potential window	1 V	2.5 V
Electrochemical impedance spectroscopy (EIS) 	Frequency range	0.1 Hz – 1 MHz	0.1 Hz – 1 MHz
	Voltage amplitude	5 mV	5 mV

This material is reserved for educational use only, not allowed for commercial use.

Forbidden to modify the content, and cite the document when use.

4.3.3 Electrochemical performance of activated carbon derived from silkworm pupae in aqueous electrolyte

Electrochemical properties were characterized in terms of cyclic voltammetry (CV), galvanostatic charge-discharge (CD) and electrochemical impedance spectroscopy (EIS) techniques.

1) Cyclic voltammetry (CV)

CV tests of each electrode was done at a potential range of $-0.2 - 0.8$ V at a scan rate of 5 mV s^{-1} using three-electrode system. Figure 4.10 shows the CV curves of the P-ACs and the YP50. The CV curves of the YP50 showed a relatively rectangular shape, indicating the electrical double layer capacitor behavior [44]. The CV curves of the P-ACs showed a slightly distorted shape with a hump located at approximately 0 V. The hump may be generated from redox reactions of the nitrogen functional groups [34, 45]. The P-ACs showed a larger curve area than the YP50. This result indicates a high capacitance even though a smaller surface area of the P-ACs.

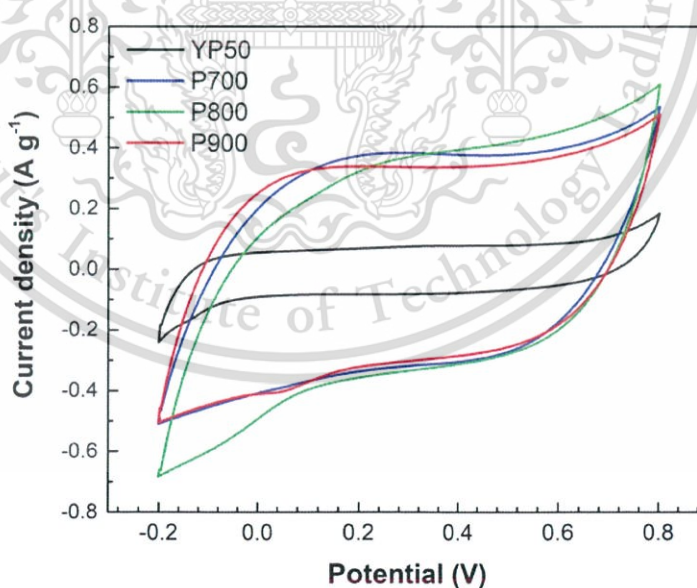


Figure 4.10 CV curves of the P-ACs and YP50 electrodes

2) Galvanostatic charge-discharge (CD)

The galvanostatic charge-discharge (CD) tests based on three-electrode system were operated at a current density of 0.2 A g^{-1} in a potential window 0 to 1.0 V as shown in Figure 4.11. All CD curves displayed a quasi-triangular shape, indicating a good electrochemical reversibility and supercapacitive behavior [46]. The P-ACs showed longer charge-discharge times than the YP50, implying a higher specific capacitance of the P-ACs. The values of the gravimetric and volumetric capacitances of each electrode were calculated by equation (3.10). The gravimetric capacitances of the P700, P800, P900 and YP50 were 131, 155, 100 and 52 F g^{-1} , respectively. The volumetric capacitances of the P700, P800, P900 and YP50 were 71, 86, 52 and 26 F cm^{-3} , respectively. The values of the gravimetric and volumetric capacitances of each electrode were summarized in Table 4.7. The P800 showed the longest charge-discharge times, given the highest values. The YP50 showed the lowest charge-discharge values in both gravimetric and volumetric capacitances.

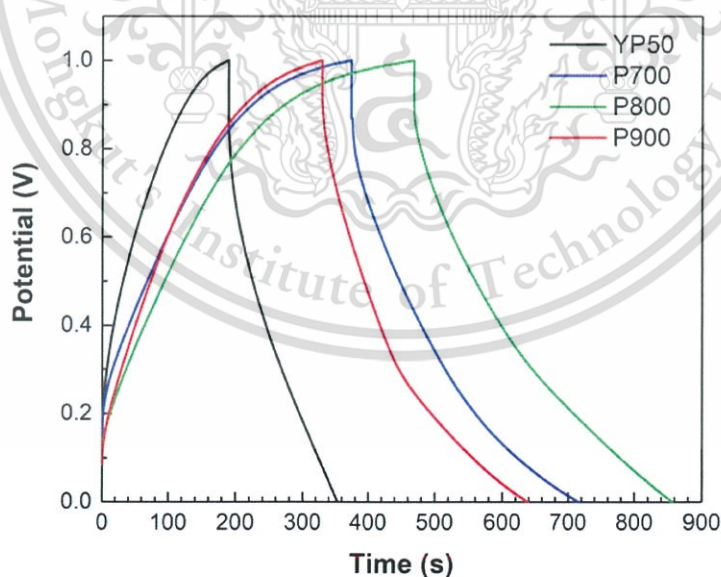


Figure 4.11 CD curves of P-ACs and YP50 electrodes

3) Electrochemical impedance spectroscopy (EIS)

The EIS test can explain electrochemical impedance by showing the Nyquist plot of supercapacitor, which consists of two parts: (i) a semicircle in the high-frequency and (ii) a straight line in the low-frequency regions. Figure 4.12 shows the Nyquist plots of each electrode. The Nyquist plots of all electrodes showed similar shape. The different offsets on the x-axis and different diameters reveal the different electrochemical characteristics of each electrode. From Nyquist plot, the series resistance (R_s) and the kinetic resistance to the ion transfer (R_{CT}) can be determined. The R_s , the sum of the resistances of electrode materials, the electrolyte and the contact between the electrode material and the current collector, can be estimated from the offset on the x-axis (Z' (Ω)) of the high-frequency semicircle. Moreover, the diameter of the semicircle represents the R_{CT} . The values of R_s of the P700, P800, P900, and YP50 were 4.8, 4.7, 4.1 and 6.8 Ω , respectively. The values of R_{CT} of the P700, P800, P900, and YP50 were 7.7, 7.3, 11.5 and 13.9 Ω , respectively. The values of R_s and R_{CT} of the P700, P800, P900, and YP50 were summarized in Table 4.7.

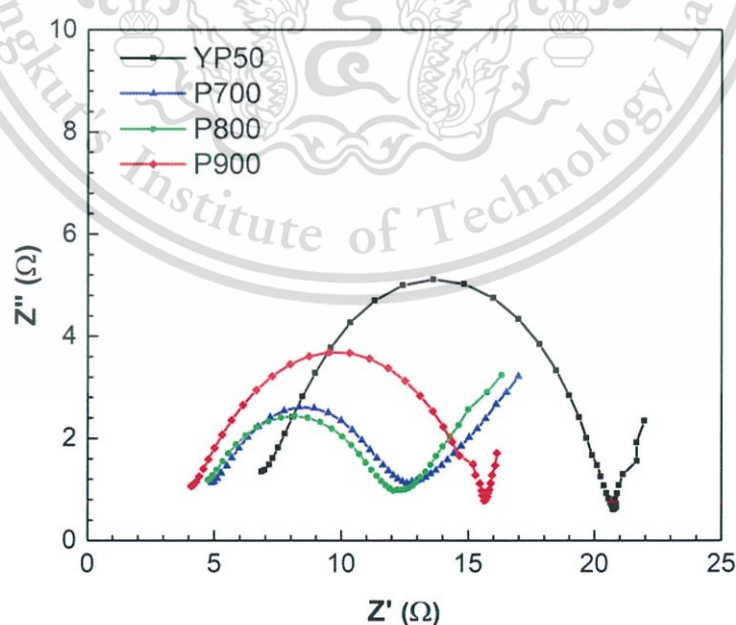


Figure 4.12 Nyquist plots of the P-ACs and YP50 electrodes

Table 4.7 Electrochemical performance of the P-ACs and YP50 electrodes in aqueous electrolyte.

Electrode	Specific capacitance		R_s (Ω)	R_{CT} (Ω)
	(Fg^{-1})	(Fcm^{-3})		
YP50	52	26	6.8	13.9
P700	131	71	4.8	7.7
P800	155	86	4.7	7.3
P900	101	52	4.1	11.5

Normally, the major factors for the high performance of supercapacitors are surface area, porosity, and heteroatom content on the surface of carbon material [41, 46, 47]. The YP50 did not exhibit the highest electrochemical performance, even though the highest surface area, the narrowest pore size distribution, and the smallest pore diameter. On the contrary, the nitrogen-enriched P-ACs showed a higher specific capacitance than the YP50. This result indicates that the nitrogen content is a dominant factor for the electrochemical performance enhancement.

Figures 4.13a-b show the radar plots to compare effect porosity properties and nitrogen-containing configurations on the electrochemical performance of each electrode, respectively. The P800 showed a higher specific capacitance than that of the P700 even though the P700 showed the highest nitrogen content. This means that it is essential to optimize nitrogen content and surface area to obtain the maximum electrochemical performance.

Besides, the R_s and R_{CT} values of each electrode relate to the surface area, and elemental composition. The R_s value of the P-ACs is in the following order: P900 < P800 < P700 < YP50. The R_{CT} value of the P-ACs is in the following order: P800 < P700 < P900 < YP50. ACs with high surface area possess the micropore structure of ACs and tend to have high resistance. The discontinuous conductivity path in the porous structure results in high resistance. However, the nitrogen of N-Q inside the aromatic

ring with sp^2 hybridization and completely saturated bonding can improve the conductivity of carbon material [48]. The working function of nitrogen configurations can be described as follows: (i) Negatively charged N-6 and N-5 improve the hydrogen atom accommodation and proton affiliation, causing the faradic reaction [5, 14]. (ii) Positively charged N-Q and N-X can improve electron transfer via the porous carbon, leading to capacitance enhancement and R_s reduction [14]. (iii) The oxygenated functional groups can increase the wettability of the carbon surface and enhance the pseudocapacitance. This is evidence as the highest specific capacitance and the lowest R_{CT} of the P800.

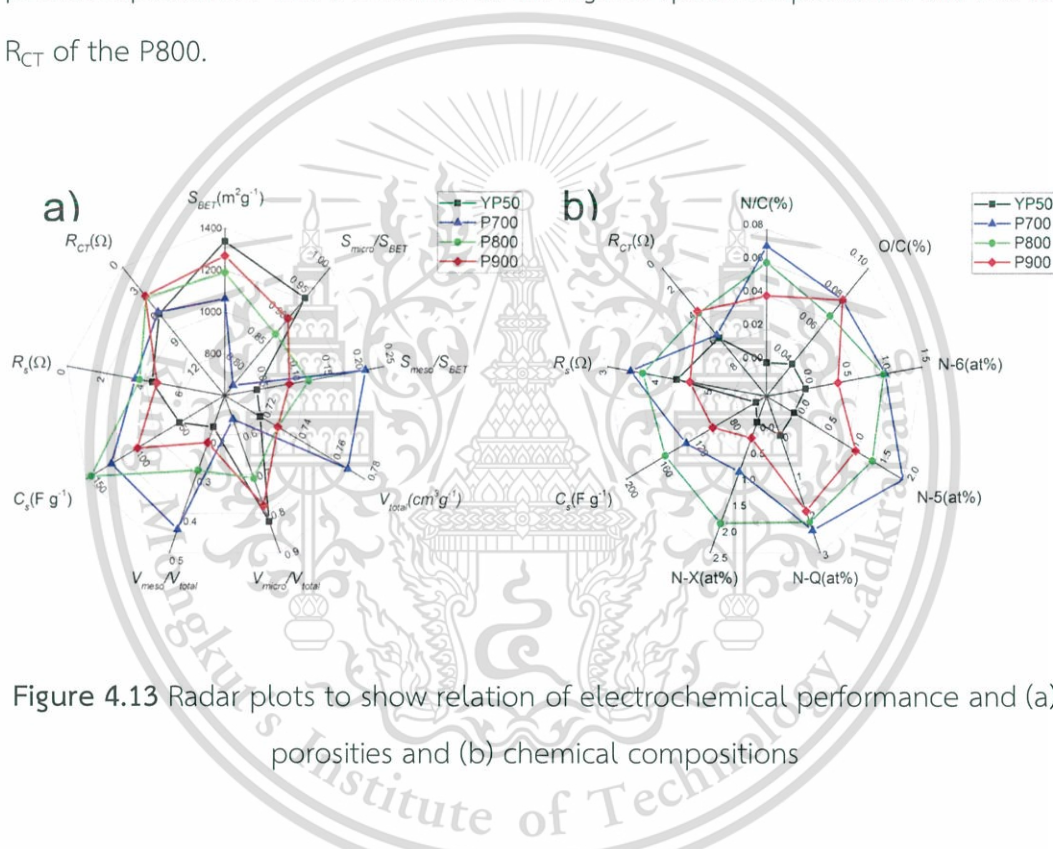


Figure 4.13 Radar plots to show relation of electrochemical performance and (a) porosities and (b) chemical compositions

4.3.4 Electrochemical performance of activated carbon derived from silkworm pupae in organic electrolyte

To enhance energy density, it is also necessary to increase window voltage of supercapacitor. However, window voltage depends on the electrolyte stability. Thus, in this research, organic electrolyte was employed to increase an operating voltage up to 2.7 V. Two electrodes were assembled using coin-cell structure in 1M TEABF₄ @ PC.

Electrochemical properties of each electrode were characterized in terms of cyclic voltammetry (CV), galvanostatic charge-discharge (CD) and capacitance retention.

1) Cyclic voltammetry (CV)

Figure 4.14 shows the CV curves with quasi-rectangular shapes and similar size at a scan rate of 5 mV s^{-1} , confirming an ideal capacitive behavior.

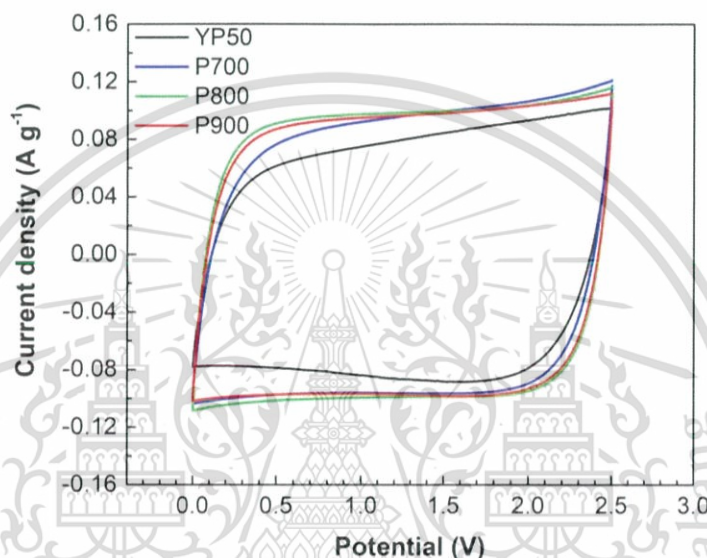


Figure 4.14 CV curves of the P-ACs and YP50 coil cells

2) Galvanostatic charge-discharge (CD)

The CD curves in Figure 4.15 exhibited relatively symmetric triangular shapes at an applied current density of 0.2 A g^{-1} . The gravimetric capacitances of the P700, P800, P900 and YP50 were 80, 92, 88 and 80 F g^{-1} , respectively. The energy densities of P700, P800, P900, and YP50 were 70, 80, 76 and 69 Wh kg^{-1} , respectively, calculated from equation (3.12). The power densities of P700, P800, P900, and YP50 were 237, 268, 265 and 209 W kg^{-1} , respectively, calculated from equation (3.13). The values of the specific capacitance, energy density and power density of each electrode were summarized as shown in Table 4.8.

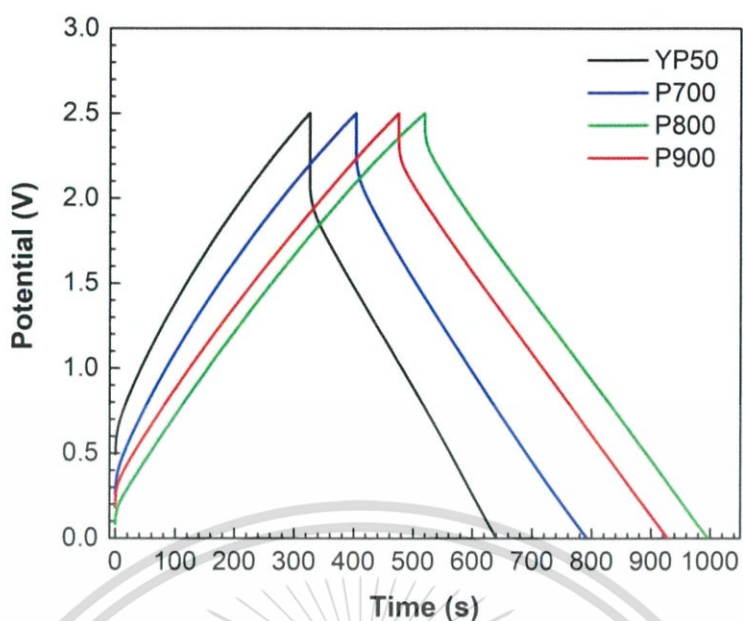


Figure 4.15 CD curves of the P-ACs and YP50

Table 4.8 Electrochemical performance of P-ACs and YP50

Electrode	Specific capacitance	Energy density	Power density (W kg ⁻¹)
	(Fg ⁻¹)	(W h kg ⁻¹)	
YP50	79	69	209
P700	80	70	237
P800	92	80	268
P900	88	76	265

The electrochemical properties of each electrode were not much different as in the aqueous electrolyte. Nevertheless, the P800 showed the highest specific capacitance while the YP50 showed the lowest values. However, the specific capacitance in organic electrolyte is less than in aqueous electrolyte. This may be due to a less effect of nitrogen-containing functional groups in organic electrolyte compared to aqueous electrolyte. Moreover, aqueous electrolytes are high ionic conductivity (up to $\sim 1 \text{ S cm}^2 \text{ mol}^{-1}$) and low viscosity, results in fast ion mobility than

This material is reserved for educational use only, not allowed for commercial use.

Forbidden to modify the content, and cite the document when use.

the organic electrolyte [49, 50]. Besides, a smaller size of ion of aqueous electrolyte makes it effectively transfer through the micro- and mesopores.

In case of organic electrolytes, the bare ions is smaller than the solvated ions. Ions are flexible with a variable diameter and can access into the pores. It is difficult to compare the effect of surface area and pore distribution on the electrochemical performance. However, the moderate surface area and the large pore diameter of the P800 provide the highest specific capacitance, implying that the nitrogenated functional groups and mesoporous structure contributed to enhancement supercapacitor in organic electrolyte systems.

3) Capacitance retention

Next, capacitance retention was investigated by CV test under a voltage window of 0.0 – 2.5 V at the scan rate of 20 mV s⁻¹ for a designated cycle. Capacitance retention (%) were calculated as follow:

$$\text{Capacitance retention (\%)} = \frac{nC_S}{1^{\text{th}}C_S} \times 100 \quad (4.2)$$

where n: order of cycles and C_S: specific capacitance. Figure 4.16 shows a capacitance retention on the P800, displaying the capacitance retention of 97.6% after 3000 cycle. These results indicate the good electrochemical cycling stability and show that ACs derived from pupae wastes are stable both in aqueous and organic electrolytes.

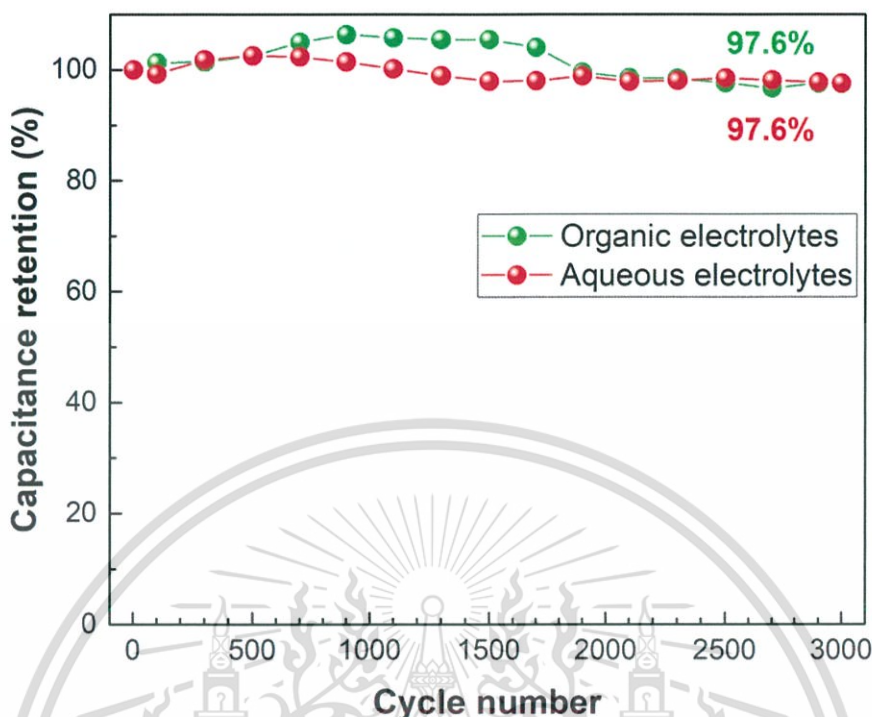


Figure 4.16 Cycling stability at the 3000th

4.4 Summary

The silkworm pupae waste-derived nitrogen self-doped AC (P-AC) was successfully synthesized by hydrothermal treatment and ZnCl₂ activation by varying temperature treatment at 700, 800 and 900 °C. Surpassing a commercial AC (YP50), the P-ACs showed higher nitrogen content but lower surface than YP50 as follows:

Surface area: 1062 – 1267 m² g⁻¹

Total pore volume: 0.73 – 0.77 cm³ g⁻¹

Nitrogen content: 3.8 – 6.4 at%

The main nitrogen-containing functional group is N-Q. This may be derived from amino acid groups existing in silkworm pupae. The P800 exhibited the highest electrochemical performance as follows:

Gravimetric capacitance: 155 F g⁻¹ in Na₂SO₄

This material is reserved for educational use only, not allowed for commercial use.

Forbidden to modify the content, and cite the document when use.

Volumetric capacitance: 86 F g⁻¹ in Na₂SO₄

Capacitance retention: 97.6 % @3000 cycles in aqueous and organic electrolytes

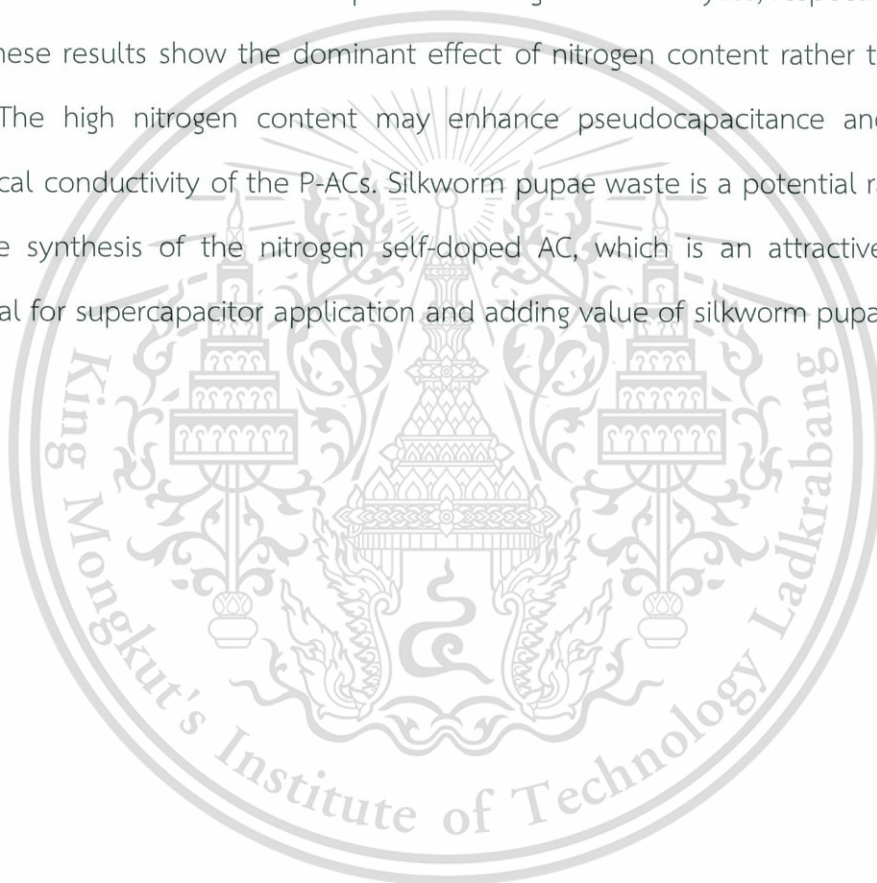
Specific capacitance: 92 F g⁻¹ in TEABF₄ in PC

Energy density: 18 W h kg⁻¹

Power density: 268 W kg⁻¹

Compared to the YP50, the P800 exhibited the highest electrochemical performance with the highest specific capacitance, approximately 3.0 and 1.2 times higher than that of the YP50 in aqueous and organic electrolytes, respectively.

These results show the dominant effect of nitrogen content rather than surface area. The high nitrogen content may enhance pseudocapacitance and improves electrical conductivity of the P-ACs. Silkworm pupae waste is a potential raw material for the synthesis of the nitrogen self-doped AC, which is an attractive electrode material for supercapacitor application and adding value of silkworm pupae waste.



CHAPTER 5

NITROGEN SELF-DOPED ACTIVATED CARBON DERIVED FROM *SAMANEA SAMAN* LEAVES AND ITS ELECTROCHEMICAL PROPERTIES

This chapter describes synthesis of nitrogen self-doped activated carbons (ACs) derived from *Samanea saman* leaves via direct activation to enhance energy density. Recently, nitrogen self-doped ACs prepared from nitrogen-enriched biomass waste were reported by many research groups. However, the nitrogen content in the ACs significantly decreased after two-step activation. Moreover, the conventional process with two steps is time-consuming. Thus, simple methods with sustainable raw materials and low cost have been required. In this chapter, a direct activation with sodium hydroxide (NaOH) negating pyrolysis or hydrothermal process using *Samanea saman* leaves as starting materials has been proposed. *Samanea saman* is known as a nitrogen-fixing tree. Chlorophyll in *Samanea saman* leaves (SSL) may provide a source of nitrogen for nitrogen self-doped ACs. Figure 5.1 shows a flow chart of the experimental procedure, including the morphology, surface area, pore size distribution, and chemical composition characterization.

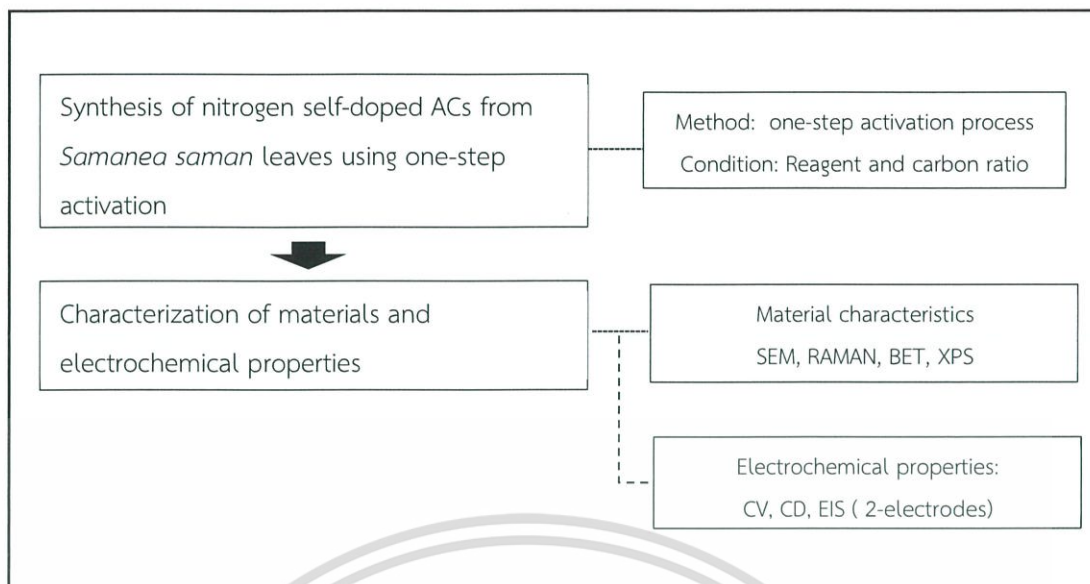


Figure 5.1 Diagram of synthesis of ACs from *Samanea saman* leaves

5.1 Synthesis of nitrogen self-doped activated carbons from *Samanea saman* leaves by direct activation

Nitrogen self-doped ACs derived from *Samanea saman* leaves were prepared via direct activation as shown in Figure 5.2.



Figure 5.2 Flow chart of synthesis of ACs from *Samanea saman* leaves

Procedure to synthesize ACs derived from SSLs is as follows:

- 1) Preparation of raw material:

1.1 Fresh SSLs were blended into small pieces. After drying, it was sieved by using a mesh size of 1 mm.

1.2 The SSL powder was impregnated with 1 M sulfuric acid (H_2SO_4) solution and then was stirred for 3 hours at 100 °C to eliminate inorganic elements, such as magnesium. Magnesium sulfate was dissolved in water and removed from SSLs. Finally, the SSL was washed by deionized (DI) water until a pH of 7 was obtained and dried at 120 °C for 12 hours.

2) Chemical activation process:

The SSL powders were impregnated with NaOH by mortar at weight ratios of SSL and NaOH as 1:1.5, 1:1.75, and 1:2 as shown in Table 5.1 (after this referred to as SD1.5, SD1.75 and SD2, respectively). The activation was done at 720 °C at a heating rate of 5 °C min⁻¹ for 1 hour under a flow of argon (99.999%) atmosphere at a flow rate of 500 mL min⁻¹. After activation, the sample was washed to pH 7 by DI water and dried at 120 °C for overnight.

For comparison, preparation of ACs from SSLs using the conventional process was also done (two-step: carbonization and activation process) [14]. Briefly, in the first step, the SSL was carbonized at 600 °C at a ramping rate of 5 °C min⁻¹ for 2 hours under nitrogen (99.999%) atmosphere. In the second step, the charcoal was mixed with NaOH at the weight ratio of charcoal and NaOH of 1:2.5, and subsequently activated at the same condition as in a direct activation (hereinafter referred to as S-AC).

The obtained ACs were characterized their morphology, porosity, chemical composition and electrochemical properties.

Table 5.1 Condition of a direct activation for synthesis of ACs derived from SSLs

N ₂ Flow rate (mL min ⁻¹)	Time activation (hour)	Temperature (°C)	Mass ratio of NaOH (SSL:NaOH)
500	2	720	1:1.5
			1:1.75
			1:2

5.2 Characterization of activated carbon derived from *Samanea saman* leaves by direct activation

The analytical techniques used for characterization of ACs were summarized in Table 5.2.

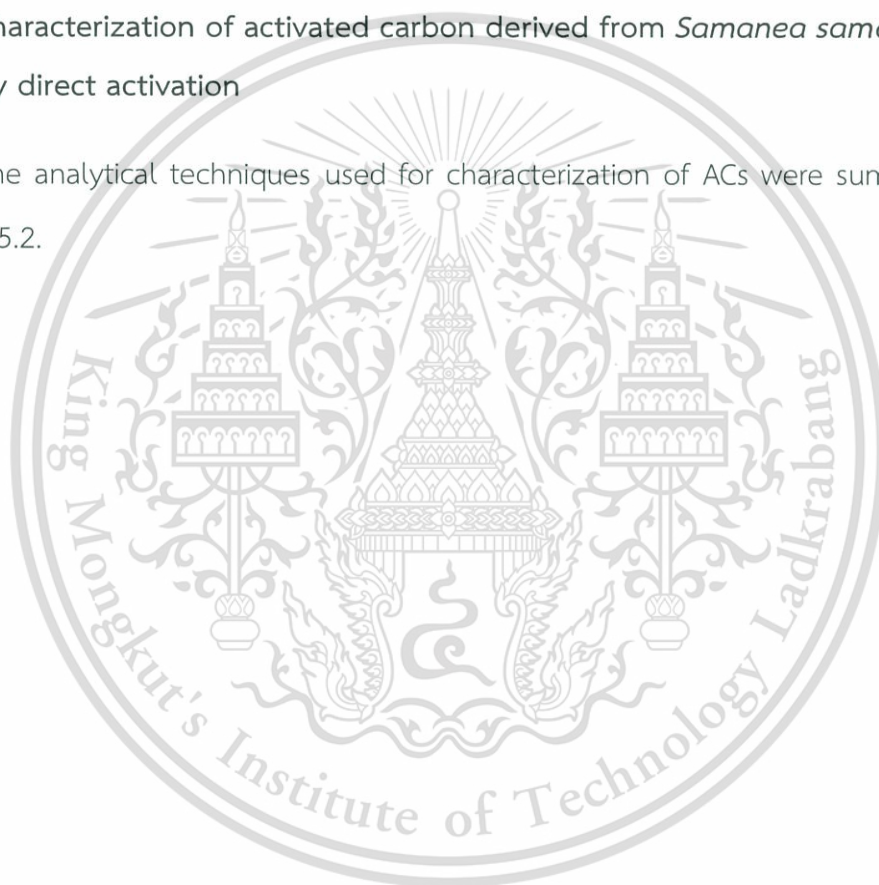


Table 5.2 Characterization techniques and their corresponding information

Techniques	Information
Scanning electron microscopy (SEM; HITACHI SU5000)	Morphologies structure
Nitrogen-adsorption isotherm (Micromeritics ASAP 2020)	Surface area and pore volume distribution
X-ray diffractometry (XRD; Rigaku SmartLab Studio II)	Crystallinity
Raman spectroscopy (Thermo Scientific DXR smart Raman)	Carbon structure
X-ray photoelectron spectroscopy (XPS; PHI Quantera II)	Chemical composition

5.2.1 Morphology of activated carbon derived from *Samanea saman* leaves

Figures 5.3a-b show SEM images of the SD2 and S-AC at a low magnification and Figure 5.3c-f show SEM images of the SD1.5, SD1.75, SD2 and S-AC at a high magnification, respectively. Both of the SD- and S-ACs showed sponge-like structures at low magnification. At high magnification, the morphologies of the SD- and S-ACs were not obviously different. SEM images at a high magnification revealed surface roughness with small flake-like pores smaller than 100 nm forming on the surface of the SD- and S-ACs. These pores were generated from the chemical reaction of NaOH. NaOH was decomposed into sodium during activation process as shown in equation (5.1) [51]. The pore formation by NaOH activation was related to a series of chemical reactions and Na intercalation. The metallic sodium during the gasification process intercalated into the carbon matrix and widening of the spaces between the carbon atomic layer and then removing metal and inorganic compounds from the carbon structure. The plausible reactions occurring during activation of NaOH could be shown as follows:

This material is reserved for educational use only, not allowed for commercial use.

Forbidden to modify the content, and cite the document when use.

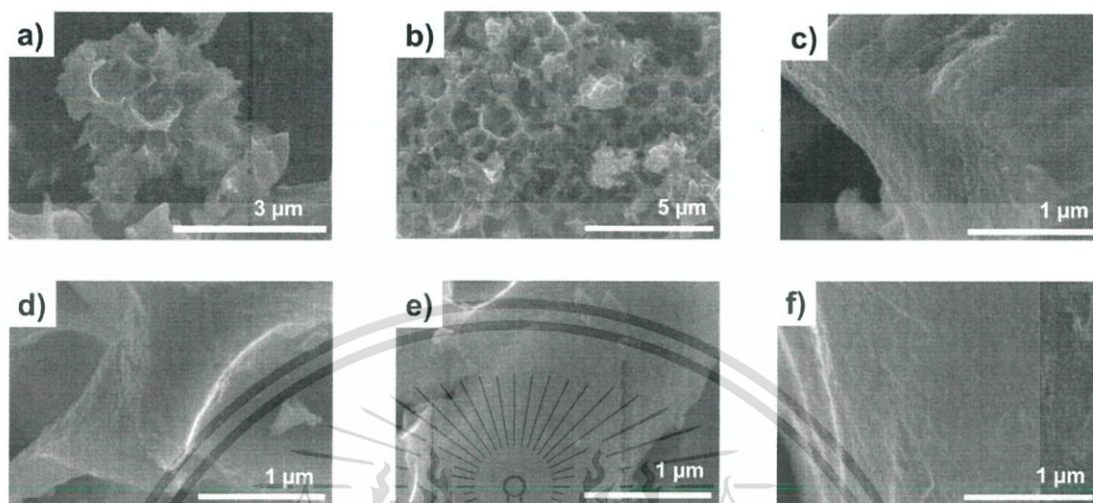


Figure 5.3 FE-SEM images at low magnification of (a) SD2 and S-AC. FE-SEM images at high magnification of (c) SD1.5, (d) SD1.75, (e) SD2 and (f) S-AC

5.2.2 Surface area and porosity of activated carbon derived from *Samanea saman* leaves

Nitrogen adsorption-desorption isotherms investigated the porosities of the ACs. The isotherms of the SD- and S-ACs were as shown in Figure 5.4a. The isotherms graphs show a steep curve at the low-pressure range, then parallel to the relative pressure axis at the high-pressure range. The adsorption and desorption branches display a narrow hysteresis loop. Thus, the SD- and S-ACs were classified as Type I isotherms (refer to the IUPAC), implying the microporous structure. A larger adsorption volume indicates a larger surface area. The porosity properties of the SD- and S-ACs were summarized in Table 5.3. The SD2 shows the highest surface area and the highest total pore volume. The specific surface area (S_{BET}) of the SD2 shows approximately $2930 \text{ m}^2 \text{ g}^{-1}$, and the total pore volume (V_{total}) achieved approximately $1.37 \text{ cm}^3 \text{ g}^{-1}$. Besides, the adsorption-desorption isotherm of the SD1.5 exhibited a sharp knee at the relative low pressure region ($P/P_0 < 0.1$) and a long plateau, suggesting a narrow

This material is reserved for educational use only, not allowed for commercial use.

micropore distribution, while those of the SD1.75 and the SD2 showed a gradually wider curve before a long plateau, suggesting a wider micropore distribution. Fig 5.4b exhibited the pore size distributions, which was calculated by DFT method. Therefore, these results show that increasing the mass ratio of NaOH agent to activation provides a sustained increase in S_{BET} and pore volume. However, the maximum mass ratio of NaOH was limited at the SD2 under our experimental condition. The excess NaOH molecules in the carbon pore wall might cause catalytic oxidation and subsequently decomposition, reducing the carbon yield as shown in equation:



For comparison, the SD2 shows superior properties in a surface area ($2930 \text{ m}^2 \text{ g}^{-1}$), a total pore volume ($1.37 \text{ cm}^3 \text{ g}^{-1}$), the volume ratio of mesopore and total pore ($V_{\text{meso}}/V_{\text{total}}$) (0.35) and a pore size (1.72 nm), suggesting that the direct activation is a capable method for a mesopore development and a pore expansion even though a lower NaOH mass ratio. The existence of mesopore and wide pore diameter of the ACs were the critical parameters for high-performance supercapacitors, which have played an essential role as a convenient route for fast transportation and penetration of electrolyte ions [52]. The significant increase in surface area of the SD2 compared to the S-ACs may attribute to the synergistic effect of organic compound decomposition and NaOH activation.

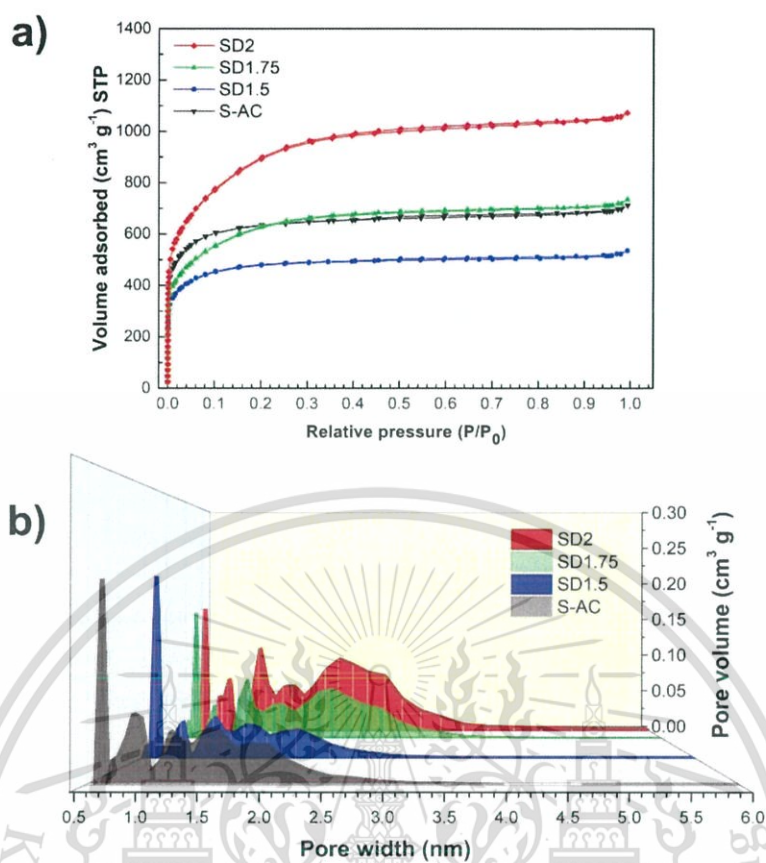


Figure 5.4 (a) N₂ adsorption/desorption isotherms, and (b) pore size distribution of the SD- and S-AC

Table 5.3 Porosity properties of SD- and S-ACs

Samples	S_{BET} (m ² g ⁻¹) ^a	Pore Diameter (nm) ^b	V_{total} (cm ³ g ⁻¹) ^c	V_{micro} (cm ³ g ⁻¹) ^c	V_{meso} (cm ³ g ⁻¹) ^c	$V_{\text{micro}}/V_{\text{total}}$	$V_{\text{meso}}/V_{\text{total}}$
S-AC	2403.1	1.63	0.86	0.75	0.10	0.87	0.11
SD1.5	1790.2	1.64	0.67	0.58	0.09	0.87	0.13
SD1.75	2112.3	1.72	0.92	0.65	0.27	0.71	0.29
SD2	2930.2	1.72	1.37	0.89	0.48	0.65	0.35

^a BET (Brunauer-Emmett-Teller) surface area. ^b Pore Diameter from DA method. ^c Total pore volume from DFT method. ^c Micropore-Mesopore volume from DFT method.

5.2.3 Crystallinity of activated carbon derived from *Samanea saman* leaves

The crystallinity of the SD- and S-ACs was characterized by XRD technique in the 2θ range of 12° to 69° . As shown in Figure 5.5, XRD patterns of SD- and S-ACs showed two broad peaks at approximately 24° and 44.6° , related to the (002) and (100) planes. It was identified as amorphous carbon. Furthermore, the low intensity of diffraction peak identified a disordered carbon structure and amorphous carbon.

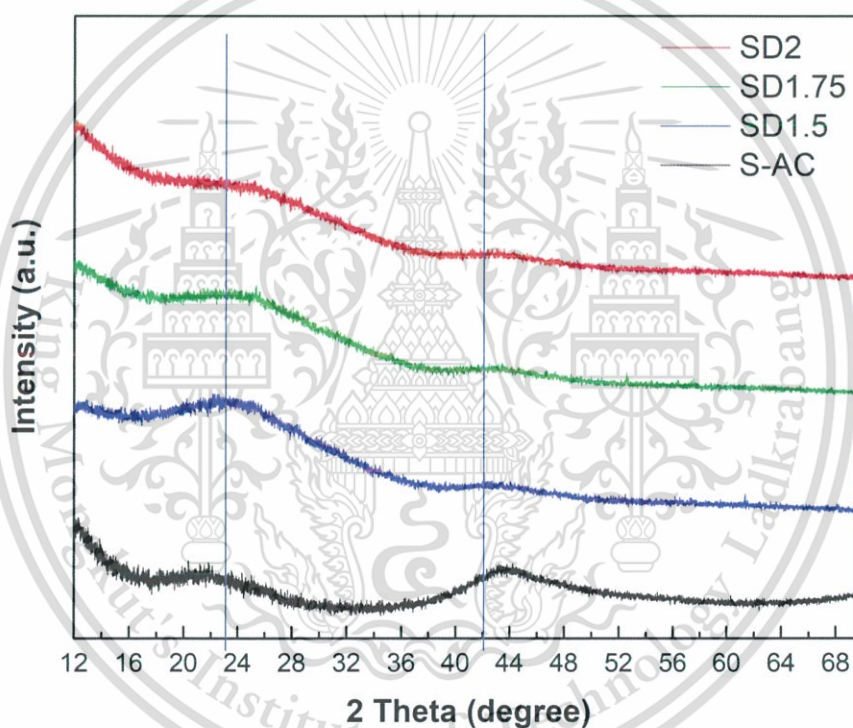


Figure 5.5 XRD diffraction patterns of all samples

5.2.4 Crystal plane structure of activated carbon derived from *Samanea saman* leaves

Raman spectroscopy techniques investigated crystal plane structure. Figure 5.6 shows the Raman spectra of the SD- and S-ACs. A couple of broad peaks, implying that as D-band and G-band by position approximately 1360 cm^{-1} and 1600 cm^{-1} were observed. Commonly, the D-band was caused by disordered carbon structures, and G-band arises from the stretching of the C-C bond in graphitic materials. The intensity ratio of D-band to G-band (I_D/I_G) is proportional to the ratio of defect sites in carbon materials. The value of I_D/I_G tended to decrease when chemical impregnation ratio increased (SD2 (0.97) < SD1.75 (0.98) < SD1.5 (0.99)). This shows that at higher NaOH contents were decomposed organic components and amorphous structures during activation, generating a higher degree of graphitic structures. Compared to the S-AC, the ratio of I_D/I_G of the SD-ACs show higher than the S-ACs. According to, the conventional activation applies thermal treatment both the carbonization process and activation process, thus enhancing the graphitic degree. Moreover, A stable carbon network of ACs with a lower surface area results in a high graphitic structure. However, it needs to adjust the balance between the degree of graphitic carbon structure and a heteroatom content to obtain the maximum supercapacitor performance.

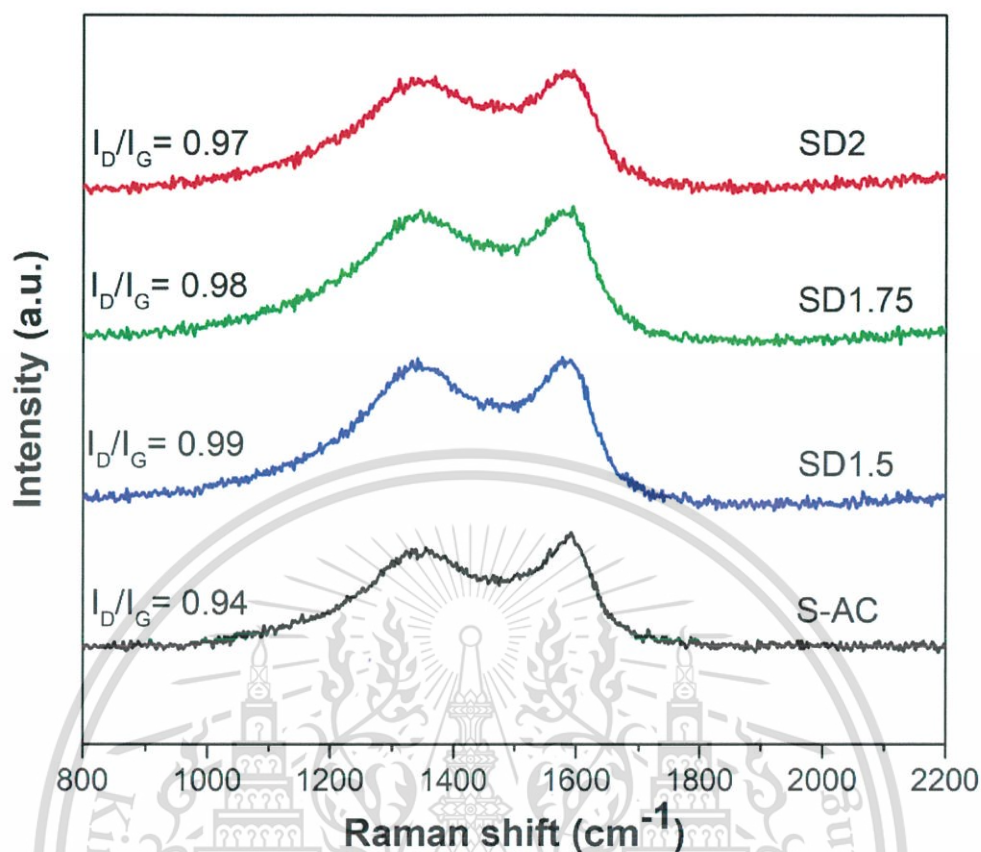


Figure 5.6 Raman spectra of all samples

5.2.5 Element composition of activated carbon derived from *Samanea saman* leaves

The elemental composition and chemical states of the ACs were investigated by using XPS technique. The summarized data of Table 5.4 exhibited the quantitative analysis of elemental composition. The ACs consisted of carbon, oxygen and nitrogen. The carbon contents of SD1.5, SD1.75, SD2 and S-AC were calculated as 86.7, 87.6, 88.4 and 90.6 at%, respectively. The superior graphitic carbon content of the S-AC than that of the SD-ACs was consistent with the results of I_D/I_G from Raman spectra. On the other hand, the nitrogen-enriched ACs play an important role in improvement of electrical conductivity and pseudocapacitance behavior of supercapacitor. The nitrogen contents of the SD1.5, SD1.75, SD2 and S-AC were calculated as 3.6, 4.2, 4.6 and 1.7

This material is reserved for educational use only, not allowed for commercial use.

Forbidden to modify the content, and cite the document when use.

at%, respectively. Nitrogen content of the SD2 was approximately 3 times higher than that of the S-AC. The ratios of nitrogen and carbon (N/C ratio) are in the following order: SD2 (5.2 %) > SD1.75 (4.8 %) >> SD1.5 (4.1 %) > S-AC (1.8 %).

Moreover, nitrogen content of the S-AC after activation decreased from 2.2 at% to 1.7at%, compared to the carbonized S-ACs. Chlorophyll may be decomposed with other organic compounds during carbonization at 600°C for 2 hours, resulting in a decrease of nitrogen content. The source of nitrogen in SSLs may come from chlorophyll. The chlorophyll is green pigments found in chloroplasts of plants, providing nitrogen self-doped ACs. The main elemental composition of SSLs were carbon, nitrogen, oxygen, magnesium and sulfur. The atomic ratio of nitrogen to magnesium is approximately 3.6, corresponding to the molecular structure of chlorophyll. The chlorophyll is four pyrrole rings containing nitrogen arranged in a ring around a magnesium ion, and a long hydrocarbon tail [53]. Nitrogen content in the SSL-derived activated carbon is approximately 4.6 at%. This value is comparable to the nitrogen-doped mesoporous by post treatment under ammonia atmosphere which including nitrogen approximately 2.96 – 7.8 at%. These results suggest that direct activation of nitrogen-containing agricultural wastes is a promising method to obtain nitrogen self-doped activated carbon.

The N1s spectra were deconvoluted to investigate their nitrogenated structures as shown in Figure 5.7. Four main peaks of nitrogen in different chemical states in the carbon network were located at approximately 398.3, 399.8, 401.1 and 403.6 eV, presenting to the pyridinic nitrogen (N-6), pyrrolic nitrogen (N-5), quaternary nitrogen (N-Q) and oxidized nitrogen (N-X), respectively. The content of each nitrogenated structure was estimated based on peak area as shown in Table 4.4. N-5 was the main component of all samples, while other nitrogen configurations were in the following order: N-X < N-Q < N-6. The dominant N-5 is depicted from the chlorophyll structure that consists of four pyrrole rings containing nitrogen arranged in a ring around a magnesium ion, and a long hydrocarbon tail.

This material is reserved for educational use only, not allowed for commercial use.

Forbidden to modify the content, and cite the document when use.

In general, N-5 and N-6 with two sp^2 carbon atoms contribute electron lone pairs into carbon systems and induce electron donor and chemical reactivity of the carbon atoms and serving a prominent role in the pseudocapacitance behavior. In case of N-Q, nitrogen atom is inside an aromatic ring, enhancing the electrical conductivity of carbon materials. It is theoretically proved that the nitrogen acts as electron donor in the carbon networks. The electrical properties of the ACs were investigated by Hall effect measurement. The resistivity and charge density of the SD2 and S-AC were calculated approximately $0.78 \Omega \cdot \text{cm}$, $1.09 \times 10^{19} \text{ cm}^{-3}$ and $0.82 \Omega \cdot \text{cm}$, $5.03 \times 10^{18} \text{ cm}^{-3}$, respectively. The higher carrier density and lower resistivity are an evidence of a higher nitrogen doping in SD2. These results are consistent with the XPS analysis.

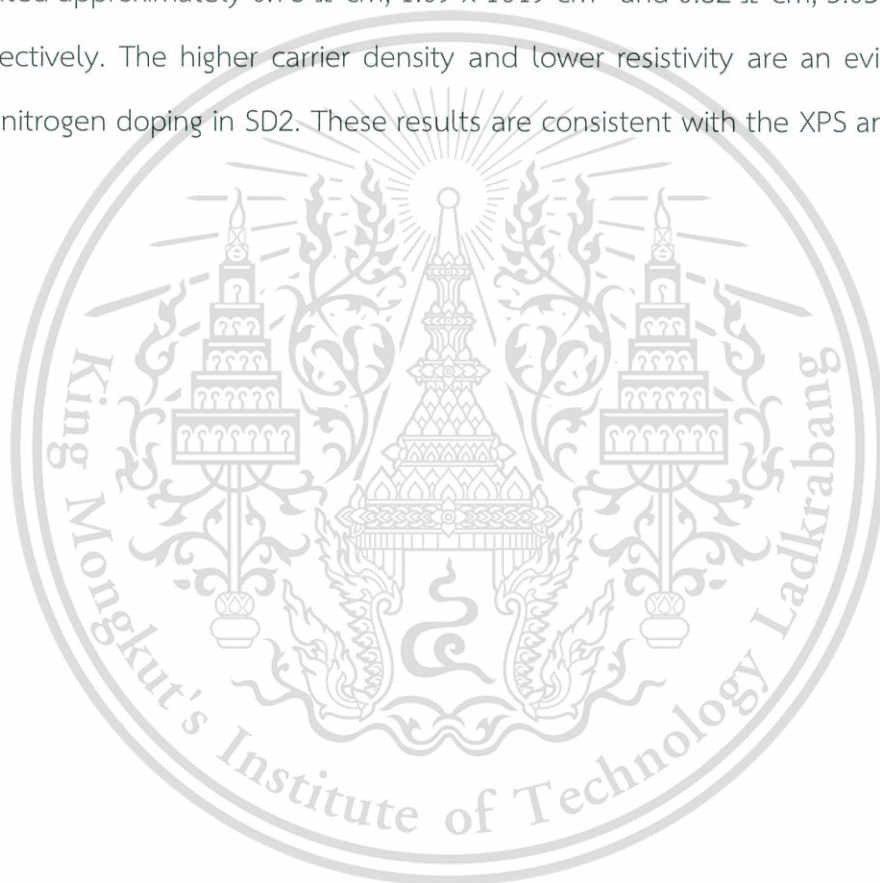


Table 5.4 Chemical composition of the SD- and S-ACs evaluated from XPS spectra

Sample	Content (at%)			N/C ratio (%)	Relative N1s peak area ^a (at%)			
	C	O	N		N-6	N-5	N-Q	N-X
SD1.5	86.7	9.7	3.6	4.15	0.87	1.98	0.58	0.17
SD1.75	87.6	8.2	4.2	4.79	1.03	2.34	0.72	0.11
SD2	88.4	7.0	4.6	5.20	1.10	2.58	0.87	0.05
S-AC	90.6	7.7	1.7	1.82	0.41	0.72	0.40	0.17

^a Pyridine N (N-6), pyrrolic N (N-5), quaternary N (N-Q) and oxidized pyridine N (N-X)

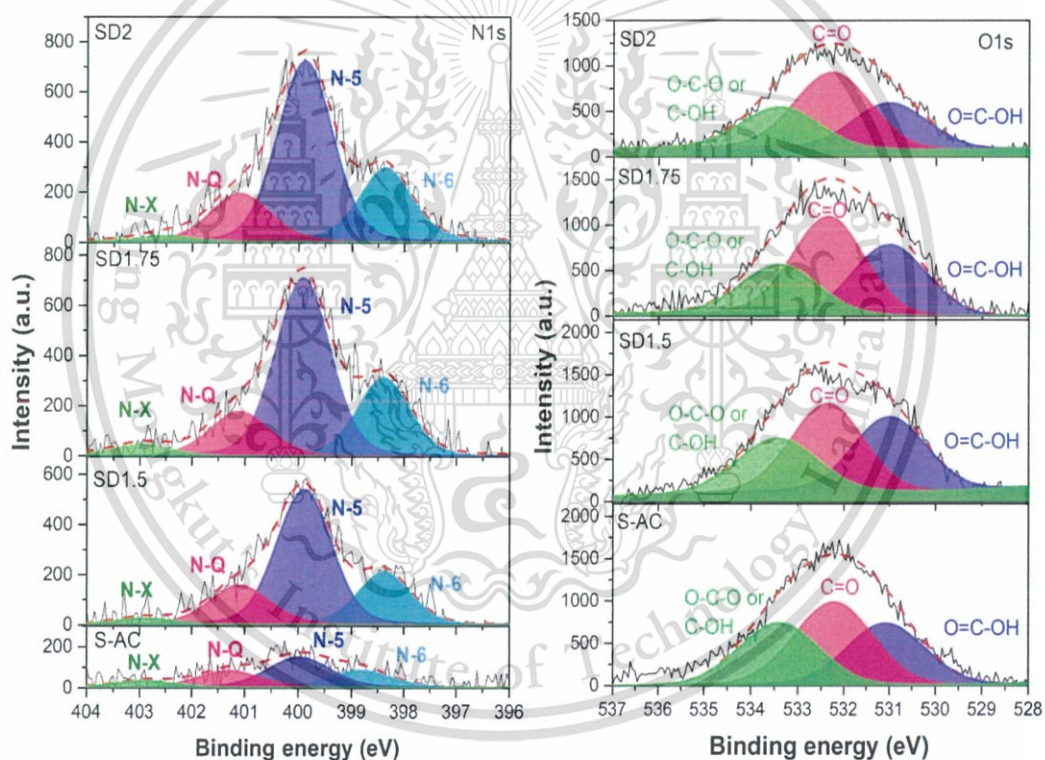


Figure 5.7 (a) N 1s and (b) O 1s XPS spectra of the SD- and S-ACs

5.3 Electrochemical properties of activated carbon derived from *Samanea saman* leaves

5.3.1 Electrode preparation

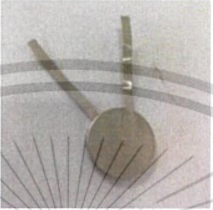
The synthesized ACs were pre-treated at 100 °C in a vacuum oven overnight before tablet formation. The AC tablets were prepared by mixing the synthesized ACs, carbon black and polytetrafluoroethylene at the weight ratio of 90:5:5 in a mortar. After that, the mixture was pressed under a pressure of 10 kN using a 10-mm diameter mold to form an electrode tablet by pressing

Regarding to characterization of electrochemical properties of electrode material, the AC tablets were assembled into a coin-cell structure (2032-type coin cell) as cathode and anode electrodes

5.3.2 Electrochemical measurement systems

The electrochemical properties of the electrode material and cell based on ACs derived from *Samanea saman* leaves were characterized by two-electrode system (Metrohm AUTOLAB PGSTAT 302). Summary of the test condition based on organic electrolytes and the test conditions of electrochemical properties are shown in Tables 5.5 and 5.6, respectively.

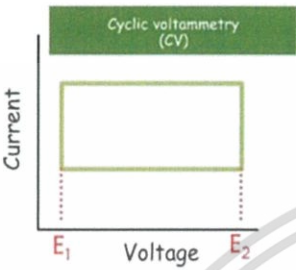
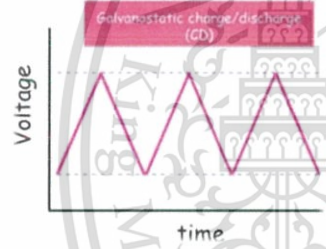
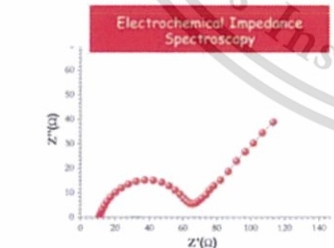
Table 5.5 Test condition based on organic electrolytes

Electrolyte	: 1M TEABF ₄ * in PC
Assembly condition	Inert atmosphere (Glove box)
Measurement system	Two electrodes
Structure	Coin cell
Electrode	ACs derived from <i>Samanea saman</i> leaves
Photograph measurement	

* TEABF₄ : Teraethylammonium tetrafluoroborate



Table 5.6 Measurement condition of electrochemical properties based on organic electrolyte

Technique	Parameter (Organic electrolyte: 2-electrode cells)	
Cyclic voltammetry (CV) 	Potential window	1.0 – 2.5 V
	Scan rate	1 mV s ⁻¹
Galvanostatic charge/discharge (CD) 	Current density	0.02 A g ⁻¹
	Potential window	2.5 V
Electrochemical impedance spectroscopy (EIS) 	Frequency range	0.1 Hz – 1 MHz
	Amplitude voltage	5 mV

5.3.3 Electrochemical performance of activated carbon derived from *Samanea saman* leaves

Electrochemical properties were characterized in terms of cyclic voltammetry (CV), galvanostatic charge-discharge (CD) and electrochemical impedance spectroscopy (EIS) techniques.

1) Cyclic voltammetry (CV)

The CV curves of all samples at a scan rate of 1 mV s^{-1} in the potential window range of 0 – 2.5 V are shown in Figure 5.8. All curves show a rectangular shape, implying electrical double-layer capacitance behavior at the interface between electrode material and electrolyte. Especially, the SD-ACs showed an additional hump at the potential at approximately 1.6 V. This hump may be due to redox reactions of the nitrogenated functional groups. In case of the S-AC, the hump was not clearly observed. This may be due to its lower nitrogen content. Normally, a large CV curve implied a higher specific capacitance. Focusing on the SD1.75, the larger curve of the SD1.75 compared to that of the S-AC implied its higher specific capacitance even though its lower surface. These results show that pseudocapacitance due to nitrogenated functional groups can effectively enhance capacitance of the ACs.

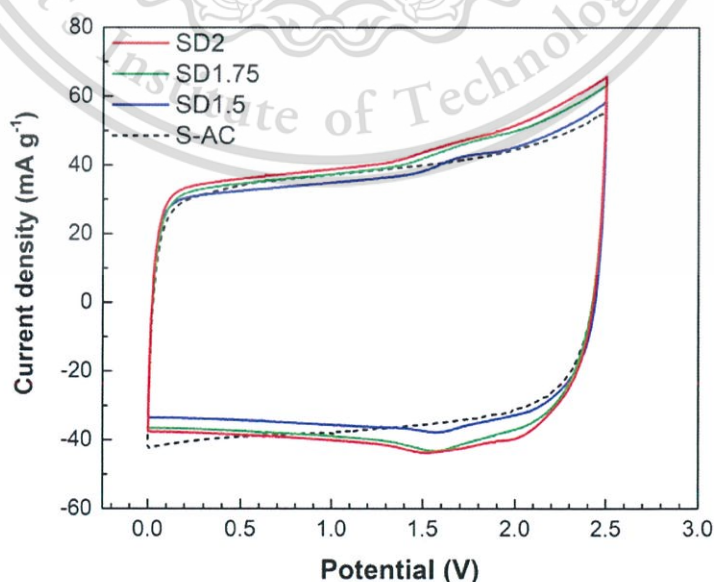


Figure 5.8 CV curves of the SD- and S-ACs

This material is reserved for educational use only, not allowed for commercial use.

Forbidden to modify the content, and cite the document when use.

2) Galvanostatic charge-discharge (CD)

The galvanostatic charge-discharge (CD) tests of two-electrode system were operated at a current density of 0.02 A g^{-1} in a window voltage from 0 to 2.5 V. CD curves of all samples were shown in Figure 5.9. The specific capacitances (C_s) were calculated from CD curves by the equation (3.10). All CD curves are a relatively symmetric triangular-type shape, indicating an excellent electrochemical reversibility and supercapacitive behavior. The CD curves of the SD-ACs showed a longer charge-discharge time, implying a higher specific capacitance than the S-AC. The gravimetric capacitances of the SD2, SD1.75, SD1.5 and S-AC were 180, 169, 151 and 138 F g^{-1} , respectively. The volumetric capacitances of the SD2, SD1.75, SD1.5 and S-AC were 88, 86, 76 and 75 F cm^{-3} , respectively. The values of the specific gravimetric and volumetric capacitances of each electrode material were in the following order: $\text{SD2} > \text{SD1.75} > \text{SD1.5} > \text{S-AC}$. Electrochemical properties are summarized as shown in Table. 5.7. The SD2 exhibited the highest electrochemical performance in both specific gravimetric and volumetric capacitances. These results were attributed to the synergistic effects of the highest surface area and additional pseudocapacitance due to nitrogen-containing functional groups.

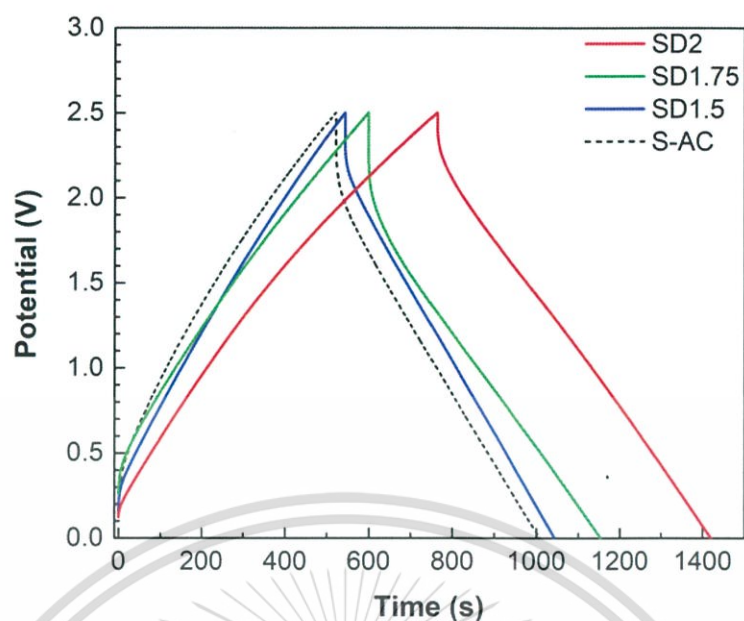


Figure 5.9 CD curves of the SD-and S-ACs

3) Electrochemical impedance spectroscopy (EIS)

The electrochemical impedance of the ACs derived from *Samanea saman* leaves were characterized. Nyquist plots of all samples obtained at the amplitude of 5 mV in the frequency range between 0.01 Hz to 1 MHz as shown in Figure 5.10. All samples present similar semicircle curves with a straight line, but different x-intercepts and diameters. The x-intercept ($Z' (\Omega)$) can be interpreted as the R_s of the electrode which is the total resistances of the electrode material, electrolytes, and the contact resistance between the collector and electrode material. The diameter of the semicircles can be interpreted as the R_{CT} of the electrode. The values of R_s and R_{CT} of the SD1.5, SD1.75, SD2 and S -AC are summarized in the Table 5.7. The SD2 shows the lowest R_s and R_{CT} compared to the S-AC, implying the enhanced electrochemical properties.

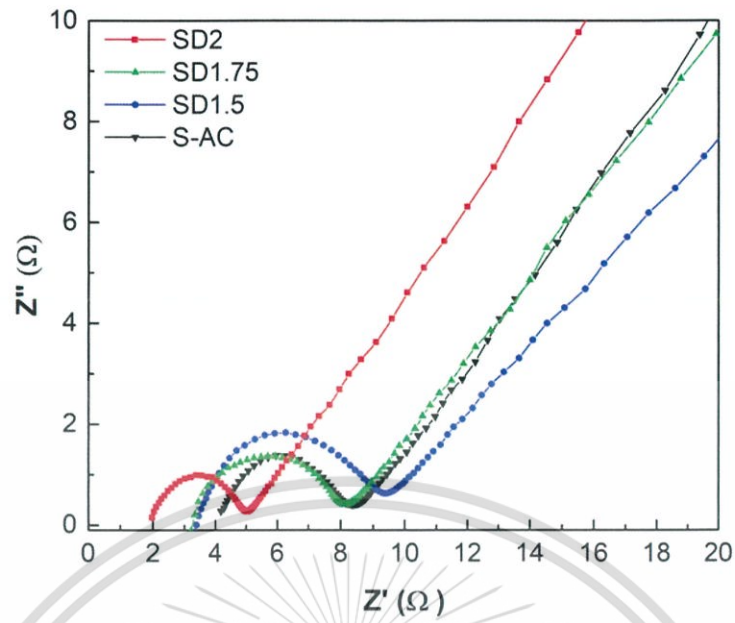


Figure 5.10 Nyquist plot of the SD- and S-ACs

Table 5.7 Summary of electrochemical properties of the SD- and S-ACs

Electrode	Specific capacitance		R_s (Ω)	R_{CT} (Ω)
	(Fg^{-1})	(Fcm^{-3})		
S-AC	138	75	4.2	4.2
SD1.5	151	76	3.3	6.0
SD1.75	169	86	3.2	4.8
SD2	179	88	2.0	3.1

The important factors to enhance supercapacitor performance are surface area, mesopore volume, pore diameter and doping level of heteroatoms in the carbon materials. In case of organic electrolyte, the ions in the forms of desolvated and/or partial desolvated ions involve in capacitive behavior. Generally, the solvated ions are larger than the desolvated ions. Thus, compared to the aqueous electrolyte, ions of the organic electrolyte are difficult to transfer into the micropores. Hence, the enlarger average pore diameter and the larger volume of the mesopore the SD-ACs are likely to be preferable path for ion accessibility, resulting in the supercapacitor enhancement in organic electrolyte system. Secondly, the nitrogen heteroatom in the SD-ACs also plays an essential role in enhancement of capacitive performance. As evidence in the SD1.5 and SD1.75, their electrochemical properties show the larger area of CV curves, the longer discharge time of CD curves, the smaller x-intercept and the smaller semicircle of EIS spectra. The reason of performance improvement can be explained as follows: The electron lone pair existing in N-5 and N-6 can enhance electrochemical performance by inducing the faradic reaction. The positive charged of N-Q can enhance the electrical conductivity of carbon material. This is confirmed by the result in the reduction of R_s and R_{CT} of the SD2.

4) Capacitance stability

This material is reserved for educational use only, not allowed for commercial use.

Forbidden to modify the content, and cite the document when use.

The SD2 showed the highest specific capacitance even though at the current densities of 0.02 A g^{-1} . A capacitance retention of the SD2-based electrode was examined by using CD measurements at the current density of 0.5 A g^{-1} . As shown in Figure 5.11, the capacitance retention of the SD2 was of 97.5 % after 3000 cycles, suggesting the highly stable electrode.

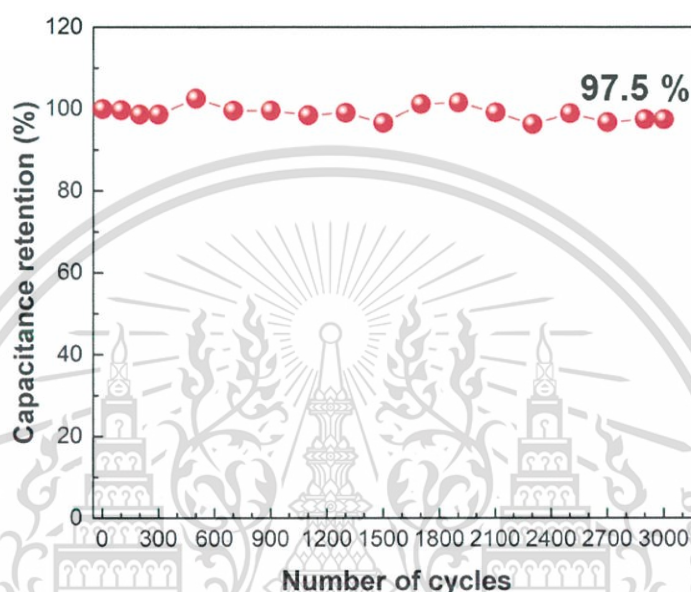


Figure 5.11 Capacitance retention of the SD2

5.3.4 Enhancement of energy density by extending voltage window

To improve the energy density, the SD2 was further investigated its working voltage window. The CD curves were tested at the window voltage up to 3.5 V based on 1 MTEABF₄ in PC electrolyte at the current density of 0.3 A g^{-1} as shown in Figure 5.12. The specific capacitance, energy density and power density were summarized as shown in Table 5.8. The specific capacitances gradually increased with the potential window, achieving the maximum specific gravimetric and volumetric capacitances of electrode material of 185 F g^{-1} and 86 F cm^{-3} at the potential voltage of 3.5 V, respectively. Moreover, the inset of Figure 5.12 displays the CD curves against the potential range of 2.5 – 3.5 V with a triangle shape, confirming the good

This material is reserved for educational use only, not allowed for commercial use.

Forbidden to modify the content, and cite the document when use.

electrochemical reversibility and supercapacitive behavior. However, a small voltage drop was observed. This may be due to the relatively high viscosity and low conductivity of organic electrolyte at ambient condition.

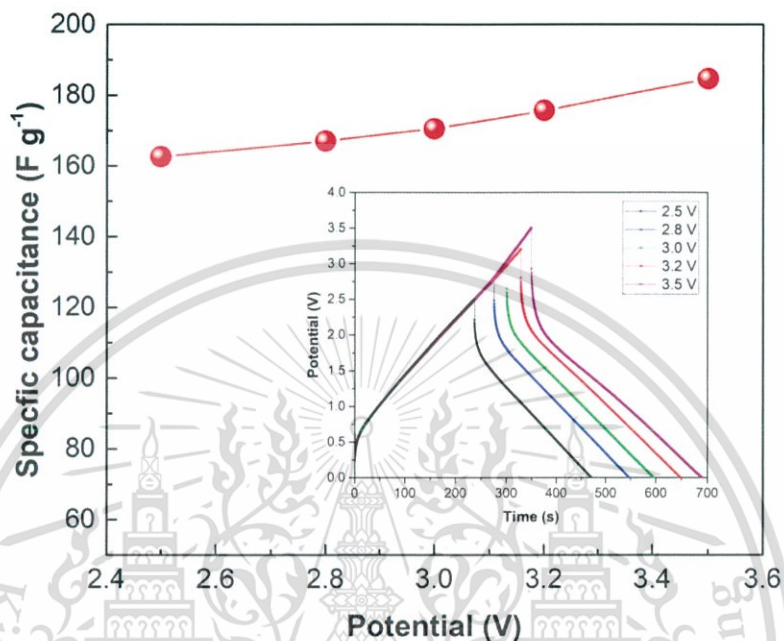


Figure 5.12 Specific capacitance by various voltage of SD2 in coin cell

Table 5.8 Summary of electrochemical properties of the SD2 at the voltage window up to 3.5 V

Voltage (V)	Specific capacitance		Energy density (Wh kg ⁻¹)	Power density (W kg ⁻¹)
	(F g ⁻¹)	(F cm ⁻³)		
2.5	163	76	35	542
2.8	167	78	46	602
3.0	171	80	53	649
3.2	176	82	62	702
3.5	185	86	79	830

Figure 5.13 shows the Ragone plot, a plot of power density against energy density, of the SD2 cell compared to other supercapacitor cells based on other agricultural wastes prepared by both conventional and direct methods. The summary data of each cell is shown in Table S1 at appendix section. The SD2 cell showed an energy density and a power density of 35 Wh kg⁻¹ and 542 W kg⁻¹ at 2.5 V and 79 Wh kg⁻¹ and 830 W kg⁻¹ at 3.5 V, respectively, exhibiting the improvement in energy density compared to ACs in other works. Moreover, as shown in Figure 5.14, a coil cell based on the SD2 was successfully lighted up the 64 super-bright white LEDs and 54 red LEDs.

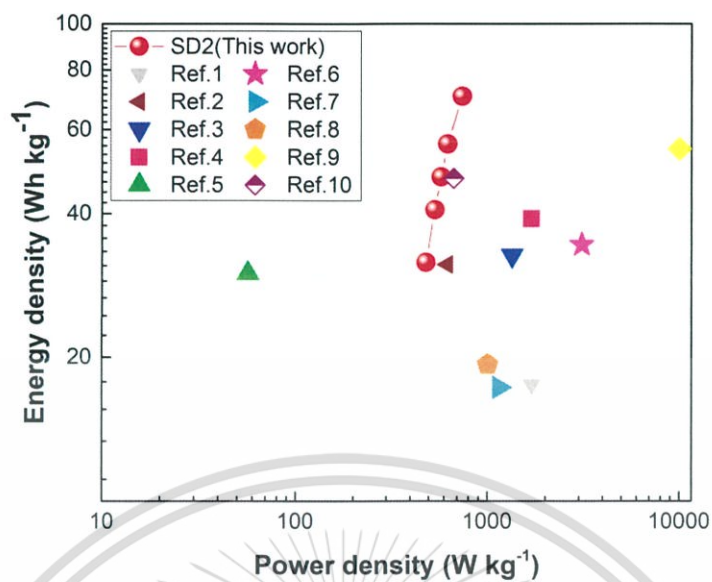


Figure 5.13 Ragone plot of coil cell of SD2 compared to other reports

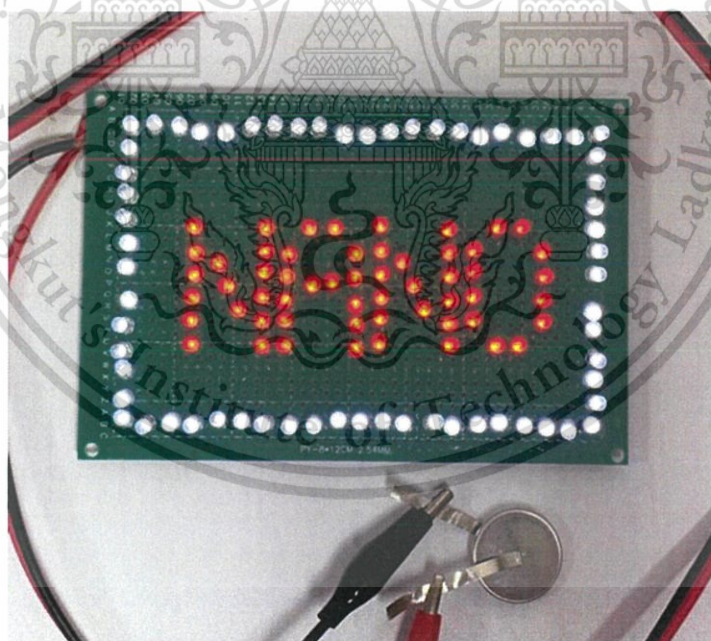


Figure 5.14 Photograph of coil cell of the P800 light up 64 white and 54 red LEDs.

5.4 Summary

The nitrogen self-doped ACs derived from direct activation of SSLs for supercapacitor with high energy density were successfully prepared. The SD-ACs were synthesized by impregnating with NaOH and directly activated at 720 °C without carbonization step. The weight ratio of raw SSLs and NaOH was optimized. Surpassing the ACs prepared by the conventional two-step method, the optimum condition was 1:2 (SD2) with the superior properties as follows:

Surface area: 2930 m² g⁻¹

Total pore volume: 1.37 cm³ g⁻¹

Nitrogen content: 4.6 at%.

The SD2 affords a nitrogen self-doping during a direct activation of SSLs with the highest content of N-5 that may come from chlorophyll component. Besides, the SD2 exhibits the highest electrochemical performance in the organic electrolyte as follows:

Gravimetric capacitance: 180 F g⁻¹

Volumetric capacitance: 88 F cm³

Capacitance retention: 97.5 % at a current density of 5 A g⁻¹

Highest voltage window: 3.5 V

Energy density: 79 Wh kg⁻¹

Power density: 829 W kg⁻¹

The direct activation of nitrogen-enriched SSLs presents the advantages in terms of a short-time process, low cost with a high surface area and a high content of nitrogen, providing a nitrogen self-doped ACs for high energy density supercapacitors.

CHAPTER 6

CONCLUSIONS

6.1 Synthesis of nitrogen-doped activated carbon derived from *silkworm pupae* and *Samanea Saman* leaves for supercapacitor application

Nitrogen self-doped ACs were successfully synthesized from nitrogen-containing agricultural wastes. Silkworm pupae were used as a starting material and were prepared by hydrothermal carbonization and ZnCl_2 activation, while *Samanea Saman* leaves were used as a starting material and were prepared by NaOH direct activation. The obtained ACs from different sources showed different properties

(1) Nitrogen self-doped ACs derived from silkworm pupae exhibited properties as follows:

Surface area: 1062 - 1267 $\text{m}^2 \text{g}^{-1}$

Total pore volume: 0.73 - 0.77 $\text{cm}^3 \text{g}^{-1}$

Nitrogen content: 3.8 - 6.4 at%

The main nitrogen-containing functional group is N-Q. This may be derived from amino acid groups existing in silkworm pupae. The P800 prepared at the activation temperature of 800 °C exhibited the highest electrochemical performance as follows:

Specific capacitance: 155 F g^{-1} in 1 M Na_2SO_4

91.6 F g^{-1} in 1M TEABF_4 in PC

Capacitance retention: 97.6 % @3000 cycles

Energy density: 18 W h kg^{-1} in 1M TEABF_4 in PC

Power density: 268 W kg^{-1} in 1M TEABF_4 in PC

Compared to commercial ACs (YP50), the P800 exhibited the highest electrochemical performance with the highest specific capacitance, approximately 3.0 and 1.2 times higher than that of the YP50 in aqueous and organic electrolytes, This material is reserved for educational use only, not allowed for commercial use.

Forbidden to modify the content, and cite the document when use.

respectively. These results imply the dominant effect of nitrogen content rather than surface area. The high nitrogen content may enhance pseudocapacitance and improves electrical conductivity. These results demonstrate that silkworm pupae waste is a potential raw material for the preparation of the nitrogen self-doped AC, which is an attractive electrode material for application in supercapacitor and contributes to the added value of silkworm pupae waste.

(2) Nitrogen self-doped ACs derived from *Samanea Saman* leaves (SSLs) exhibited properties as follows:

Surface area:	2930 m ² g ⁻¹
Total pore volume:	1.37 cm ³ g ⁻¹
Nitrogen content:	4.6 at%

The main nitrogen-containing functional group is N-5. This may be derived from chlorophyll structure. The SD2 (the weight ratio of SSLs and NaOH of 1:2) prepared at the activation temperature of 720 °C exhibited the highest electrochemical performance in 1M TEABF₄ in PC as follows:

Gravimetric capacitance:	180 F g ⁻¹
Volumetric capacitance:	88 F cm ⁻³
Capacitance retention:	97.5 % at a current density of 5 A g ⁻¹
Highest voltage window:	3.5 V
Energy density:	79 Wh kg ⁻¹
Power density:	829 W kg ⁻¹

The direct activation of nitrogen-enriched SSLs presents the advantages in terms of a short-time process, low cost with a high surface area, a high content of nitrogen and a widening voltage window, providing a nitrogen self-doped ACs for high energy density supercapacitor.

Summary of the ACs prepared from different starting materials is shown in Table 6.1. Comparison of nitrogen content prepared by different methods are shown in Table 6.2. This material is reserved for educational use only, not allowed for commercial use.

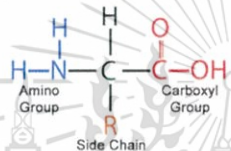
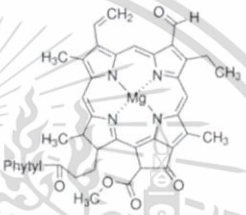
Table 6.1 Summary of the ACs prepared from different starting materials

Properties	Unit	ACs	
		P800 (Silkworm pupae)	SD2 (Samanea saman leaves)
N-content	at%	5.2	4.6
Surface area	$\text{m}^2 \text{g}^{-1}$	1188	2930
Pore diameter	nm	1.48	1.72
Pore volume	$\text{cm}^3 \text{g}^{-1}$	0.73	1.37
Specific capacitance (F g^{-1})	1M Na_2SO_4	154	322
	1M TEABF_4	92	179
Maximum Energy density	Wh kg^{-1}	18 @2.5 V	79 @3.5 V
Yield	%	5	10
Total process time	Hour	80	57
Feasibility	-	Low yield & long cycle time	Large scale production

This material is reserved for educational use only, not allowed for commercial use.

Forbidden to modify the content, and cite the document when use.

Table 6.2 Comparison of nitrogen content prepared by different methods

	Silkworm	<i>Samanea saman</i> leaves	Post-doping (Literature reviews)
Nitrogen (at%)	5.2	4.5	2.9 – 7.8
Main N- compound	N-Q	N-5	N-5
Origin of nitrogen	<p>Amino acid</p> <p>Amino Acid Structure</p> 	<p>Chlorophyll</p> 	Urea ($\text{CH}_4\text{N}_2\text{O}$), NH_3

6.2 Suggestions for future work

6.2.1 For practical application, a large-scale preparation of the ACs is required. The optimal parameter for a large-scale preparation should be further studied.

6.2.2 To obtain the maximum electrochemical properties, the selection of organic electrolyte with the size corresponding to the pore size of the ACs should be further investigated.

REFERENCE

- [1] R. Kötz, M. Carlen, Principles and applications of electrochemical capacitors, **Electrochim. Acta**, 45(15), (2000), 2483.
- [2] A. Burke, R&D considerations for the performance and application of electrochemical capacitors, **Electrochim. Acta**, 53(3), (2007), 1083.
- [3] J.R. Miller, P. Simon, Materials science. Electrochemical capacitors for energy management, **Science**, 321(5889), (2008), 651.
- [4] E. Lim, C. Jo, J. Lee, A mini review of designed mesoporous materials for energy-storage applications: from electric double-layer capacitors to hybrid supercapacitors, **Nanoscale**, 8(15), (2016), 7827.
- [5] A.M. Abioye, F.N. Ani, Recent development in the production of activated carbon electrodes from agricultural waste biomass for supercapacitors: A review, **J. Renew. Sustain. Energy**, 52, (2015), 1282.
- [6] C.-T. Hsieh, H. Teng, Influence of oxygen treatment on electric double-layer capacitance of activated carbon fabrics, **Carbon**, 40(5), (2002), 667.
- [7] G. Lota, B. Grzyb, H. Machnikowska, J. Machnikowski, E. Frackowiak, Effect of nitrogen in carbon electrode on the supercapacitor performance, **Chem. Phys. Lett.**, 404 (1-3), (2005), 53.
- [8] D. Hulicova-Jurcakova, M. Kodama, S. Shiraishi, H. Hatori, Z.H. Zhu, G.Q. Lu, Nitrogen-Enriched Nonporous Carbon Electrodes with Extraordinary Supercapacitance, **Adv. Funct. Mater.**, 19(11), (2009), 1800.
- [9] D. Hulicova-Jurcakova, M. Seredych, G.Q. Lu, T.J. Bandosz, Combined Effect of Nitrogen- and Oxygen-Containing Functional Groups of Microporous Activated Carbon on its Electrochemical Performance in Supercapacitors, **Adv. Funct. Mater.**, 19(3), (2009), 438.
- [10] X. Hong, K.S. Hui, Z. Zeng, K.N. Hui, L. Zhang, M. Mo, M. Li, Hierarchical nitrogen-doped porous carbon with high surface area derived from endothelium corneum gigeriae galli for high-performance supercapacitor, **Electrochim. Acta**, 130, (2014), 464.

- [11] J. Hou, C. Cao, F. Idrees, X. Ma, Hierarchical Porous Nitrogen-Doped Carbon Nanosheets Derived from Silk for Ultrahigh-Capacity Battery Anodes and Supercapacitors, **ACS Nano**, 9(3), (2015), 2556.
- [12] M. Wahid, G. Parte, D. Phase, S. Ogale, Yogurt: a novel precursor for heavily nitrogen doped supercapacitor carbon, **J. Mater. Chem. A**, 3(3), (2015), 1208.
- [13] S.-M. Alatalo, K. Qiu, K. Preuss, A. Marinovic, M. Sevilla, M. Sillanpää, X. Guo, M.-M. Titirici, Soy protein directed hydrothermal synthesis of porous carbon aerogels for electrocatalytic oxygen reduction, **Carbon**, 96, (2016), 622.
- [14] P. Dulyaseree, M. Fujishige, I. Yoshida, Y. Toya, Y. Banba, Y.-s. Tanaka, T. Aoyama, M. Phonyiem, W. Wongwiriyan, K. Takeuchi, M. Endo, Nitrogen-rich green leaves of papaya and *Coccinia grandis* as precursors of activated carbon and their electrochemical properties, **RSC Adv.**, 7(67), (2017), 42064.
- [15] M. Lu, F. Beguin, E. Frackowiak, **Supercapacitors : Materials, Systems, and Applications**, Wiley VCH, Weinheim, 2013.
- [16] F. Reymond, D. Fermin, H.J. Lee, H.H. Girault, Electrochemistry at liquid/liquid interfaces: methodology and potential applications, **Electrochim. Acta**, 45(15), (2000), 2647.
- [17] J. Chmiola, G. Yushin, Y. Gogotsi, C. Portet, P. Simon, P.L. Taberna, Anomalous Increase in Carbon Capacitance at Pore Sizes Less Than 1 Nanometer, **Science**, 313(5794), (2006), 1760.
- [18] M. Frank Rose, C. Johnson, T. Owens, B. Stephens, Limiting factors for carbon-based chemical double-layer capacitors, **J. Power Sources**, 47(3), (1994), 303.
- [19] T.Y. Kim, H.W. Lee, M. Stoller, D.R. Dreyer, C.W. Bielawski, R.S. Ruoff, K.S. Suh, High-Performance Supercapacitors Based on Poly(ionic liquid)-Modified Graphene Electrodes, **ACS Nano**, 5(1), (2011), 436.
- [20] L.L. Zhang, X.S. Zhao, Carbon-based materials as supercapacitor electrodes, **Chem. Soc. Rev.**, 38(9), (2009), 2520.
- [21] J.P. Zheng, P.J. Cygan, T.R. Jow, Hydrous Ruthenium Oxide as an Electrode Material for Electrochemical Capacitors, **J. Electrochem. Soc.**, 142(8), (1995), 2699.
- [22] V. Subramanian, C. Luo, A.M. Stephan, K.S. Nahm, S. Thomas, B. Wei, Supercapacitors from Activated Carbon Derived from Banana Fibers, **J. Phys. Chem. C.**, 111(20), (2007), 7527.

- [23] Y. Kim, B. Lee, H. Suezaki, T. Chino, Y. Abe, T. Yanagiura, K.C. Park, M. Endo, Preparation and characterization of bamboo-based activated carbons as electrode materials for electric double layer capacitors, **Carbon**, 44, (2006).
- [24] L. Sun, C. Tian, M. Li, X. Meng, L. Wang, R. Wang, J. Yin, H. Fu, From coconut shell to porous graphene-like nanosheets for high-power supercapacitors, **J. Mater. Chem. A**, 1(21), (2013), 6462.
- [25] S. Zhao, C.-Y. Wang, M.-M. Chen, J. Wang, Z.-Q. Shi, Potato starch-based activated carbon spheres as electrode material for electrochemical capacitor, **J. Phys. Chem. Solids**, 70(9), (2009), 1256.
- [26] X. Li, W. Xing, S. Zhuo, J. Zhou, F. Li, S.-Z. Qiao, G.-Q. Lu, Preparation of capacitor's electrode from sunflower seed shell, **Bioresour. Technol.**, 102(2), (2011), 1118.
- [27] M. Li, J. Xue, Integrated Synthesis of Nitrogen-Doped Mesoporous Carbon from Melamine Resins with Superior Performance in Supercapacitors, **J. Phys. Chem. C.**, 118(5), (2014), 2507.
- [28] T. Wei, Q. Zhang, X. Wei, Y. Gao, H. Li, A Facile and Low-Cost Route to Heteroatom Doped Porous Carbon Derived from *Broussonetia Papyrifera* Bark with Excellent Supercapacitance and CO₂ Capture Performance, **Sci. Rep.**, 6, (2016), 22646.
- [29] M. Zhou, F. Pu, Z. Wang, S. Guan, Nitrogen-doped porous carbons through KOH activation with superior performance in supercapacitors, **Carbon**, 68, (2014), 185.
- [30] J. Sun, J. Niu, M. Liu, J. Ji, M. Dou, F. Wang, Biomass-derived nitrogen-doped porous carbons with tailored hierarchical porosity and high specific surface area for high energy and power density supercapacitors, **Appl. Surf. Sci.**, 427, (2017).
- [31] B. Xu, S. Hou, G. Cao, F. Wu, Y. Yang, Sustainable nitrogen-doped porous carbon with high surface areas prepared from gelatin for supercapacitors, **J. Mater. Chem.**, 22(36), (2012), 19088.
- [32] Y.-Q. Zhao, M. Lu, P.-Y. Tao, Y.-J. Zhang, X.-T. Gong, Z. Yang, G.-Q. Zhang, H.-L. Li, Hierarchically porous and heteroatom doped carbon derived from tobacco rods for supercapacitors, **J. Power Sources**, 307, (2016), 391.
- [33] H. Chen, F. Yu, G. Wang, L. Chen, B. Dai, S. Peng, Nitrogen and Sulfur Self-Doped Activated Carbon Directly Derived from Elm Flower for High-Performance Supercapacitors, **ACS Omega**, 3(4), (2018), 4724.

- [34] X. Chen, J. Zhang, B. Zhang, S. Dong, X. Guo, X. Mu, B. Fei, A novel hierarchical porous nitrogen-doped carbon derived from bamboo shoot for high performance supercapacitor, **Sci. Rep.**, 7(1), (2017), 7362.
- [35] Wikipedia, **Scanning electron microscope** [online].
https://en.wikipedia.org/wiki/Scanning_electron_microscope, 2019.
- [36] Wikipedia, **Transmission electron microscopy** [online].
https://en.wikipedia.org/wiki/Transmission_electron_microscopy, 2019.
- [37] M.A. 2020, **Nitrogen-adsorption isotherm** [online].
<https://www.micromeritics.com/Product-Showcase/ASAP-2020-Plus-Physisorption.aspx>, 2019.
- [38] Rigaku, **X-ray diffractometer (XRD)** [online].
<https://www.rigaku.com/en/products/xrd/smartlab>, 2018.
- [39] ULVAC-PHI, **X-ray Photoelectron Spectroscopy** [online].
<https://www.ulvac-phi.com/en/products/xps/phi-quantera-ii/>, 2015.
- [40] Wikipedia, **Raman Spectroscopy** [online].
https://en.wikipedia.org/wiki/Raman_spectroscopy, 2019.
- [41] X.Y. Chen, C. Chen, Z.J. Zhang, D.H. Xie, X. Deng, J.W. Liu, Nitrogen-doped porous carbon for supercapacitor with long-term electrochemical stability, **J. Power Sources**, 230, (2013), 50.
- [42] H. Schmiers, J. Friebel, P. Streubel, R. Hesse, R. Köpsel, Change of chemical bonding of nitrogen of polymeric N-heterocyclic compounds during pyrolysis, **Carbon**, 37(12) (1999) 1965.
- [43] R. Wang, T. Zhou, H. Li, H. Wang, H. Feng, J. Goh, S. Ji, Nitrogen-rich mesoporous carbon derived from melamine with high electrocatalytic performance for oxygen reduction reaction, **J. Power Sources**, 261, (2014), 238.
- [44] J. Wang, L. Shen, B. Ding, P. Nie, H. Deng, H. Dou, X. Zhang, Fabrication of porous carbon spheres for high-performance electrochemical capacitors, **RSC Adv.**, 4(15) (2014) 7538.
- [45] H. Zhu, X. Wang, F. Yang, X. Yang, Promising carbons for supercapacitors derived from fungi, **Adv. Mater.**, 23(24), (2011), 2745.
- [46] D. Liu, C. Fu, N. Zhang, H. Zhou, Y. Kuang, Three-Dimensional Porous Nitrogen doped Graphene Hydrogel for High Energy Density supercapacitors, **Electrochim. Acta**, 213, (2016), 291.

This material is reserved for educational use only, not allowed for commercial use.

Forbidden to modify the content, and cite the document when use.

- [47] V. Augustyn, J. Come, M.A. Lowe, J.W. Kim, P.L. Taberna, S.H. Tolbert, H.D. Abruna, P. Simon, B. Dunn, High-rate electrochemical energy storage through Li⁺ intercalation pseudocapacitance, **Nat. Mater.**, 12(6), (2013), 518.
- [48] M. Yang, Z. Zhou, Recent Breakthroughs in Supercapacitors Boosted by Nitrogen-Rich Porous Carbon Materials, **Adv. Sci.**, 4(8), (2017), 1600408.
- [49] T. Devarajan, S. Higashiya, C. Dangler, M. Rane-Fondacaro, J. Snyder, P. Haldar, Novel ionic liquid electrolyte for electrochemical double layer capacitors, **Electrochem. Commun.**, 11(3), (2009), 680.
- [50] C. Zhong, Y. Deng, W. Hu, J. Qiao, L. Zhang, J. Zhang, A review of electrolyte materials and compositions for electrochemical supercapacitors, **Chem. Soc. Rev.**, 44(21), (2015), 7484.
- [51] M.A. Lillo-Ródenas, D. Cazorla-Amorós, A. Linares-Solano, Understanding chemical reactions between carbons and NaOH and KOH: An insight into the chemical activation mechanism, **Carbon**, 41(2), (2003), 267.
- [52] A.G. Pandolfo, A.F. Hollenkamp, Carbon properties and their role in supercapacitors, **J. Power Sources**, 157(1), (2006), 11.
- [53] B.H. Patel, in: M. Clark (Ed.), **Handbook of Textile and Industrial Dyeing**, Woodhead Publishing, Kidlington, United Kingdom, 2011, p. 395.



This material is reserved for educational use only, not allowed for commercial use.

Forbidden to modify the content, and cite the document when use.

1. Electrochemical properties of activated carbons derived from Silkworm pupae waste in 1 M TEAB₄

1.1 Electrochemical impedance spectroscopy (EIS) based on organic electrolytes

The EIS test can explain electrochemical impedance by showing the Nyquist plot of supercapacitor based on organic electrolytes. Figure S1 shows the Nyquist plots of each electrode in the frequency range between 1 Hz – 1 MHz with an amplitude of 5 mV. From Nyquist plot, the series resistance (R_s) and the kinetic resistance to the ion transfer (R_{CT}) can be determined. The values of R_s of the P700, P800, P900, and YP50 were 2.7, 2.5, 1.8 and 1.3 Ω , respectively. The values of R_{CT} of the P700, P800, P900, and YP50 were 18.8, 10.1, 4.8 and 10.8 Ω , respectively.

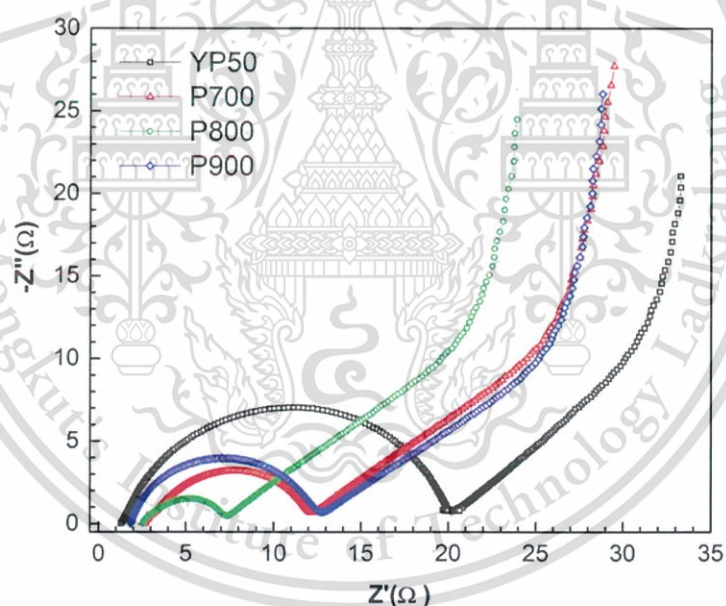


Figure S1 Nyquist plot of the P-ACs and YP50

2. Electrochemical properties of activated carbons derived from *Samanea saman* leaves in 1 M Na₂SO₄

2.1 Cyclic voltammetry (CV)

Electrochemical properties of each electrode using three-electrode system was measured at a potential range of 0.2 – 0.8 V at scan rate 1 mV s⁻¹ in 1 M H₂SO₄. Figure S2 shows CV curves of SD- and S-ACs. The SD2 showed a hump located at approximately 0 V, implying that it generated from redox reactions of the nitrogen functionalities. The area of the CV curves of the SD2 was the largest, implying that a high capacitance came from high surface area and nitrogen content.

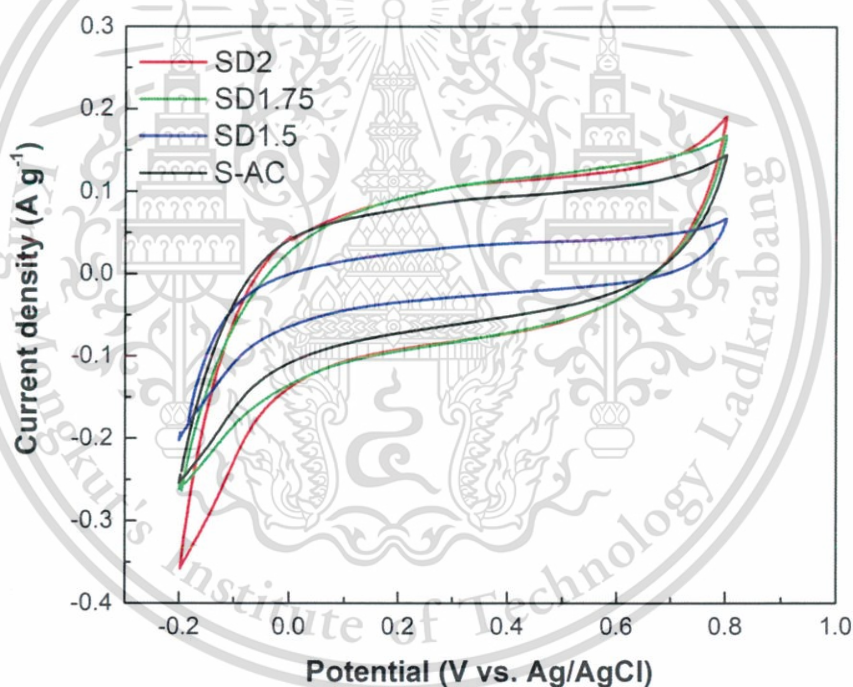


Figure S2 CV curves of the SD- and S-ACs

2.2 Galvanostatic charge-discharge (CD)

The galvanostatic charge-discharge (CD) tests based on three-electrode system were measured in the potential range of 0.0 – 1.0 V at the current density of 0.3 A g⁻¹ as shown in Figure S3. All CD curves displayed a quasi-triangular shape, indicating a

This material is reserved for educational use only, not allowed for commercial use.

Forbidden to modify the content, and cite the document when use.

good electrochemical reversibility and supercapacitive behavior. The values of the gravimetric capacitances of each electrode was calculated by CD curves. The gravimetric capacitances of the SD2, SD1.75, SD1.5 and S-AC were 322, 280, 205 and 83 F g⁻¹, respectively. The SD2 showed the longest charge-discharge times, given the highest specific capacitance values. The highest surface area, volumes of micro- and meso-pores and the highest nitrogen content played a dominant role in the highest gravimetric capacitance. This evidence result of the SD1.75 shows the higher specific capacitance even though its lower surface area than the S-AC.

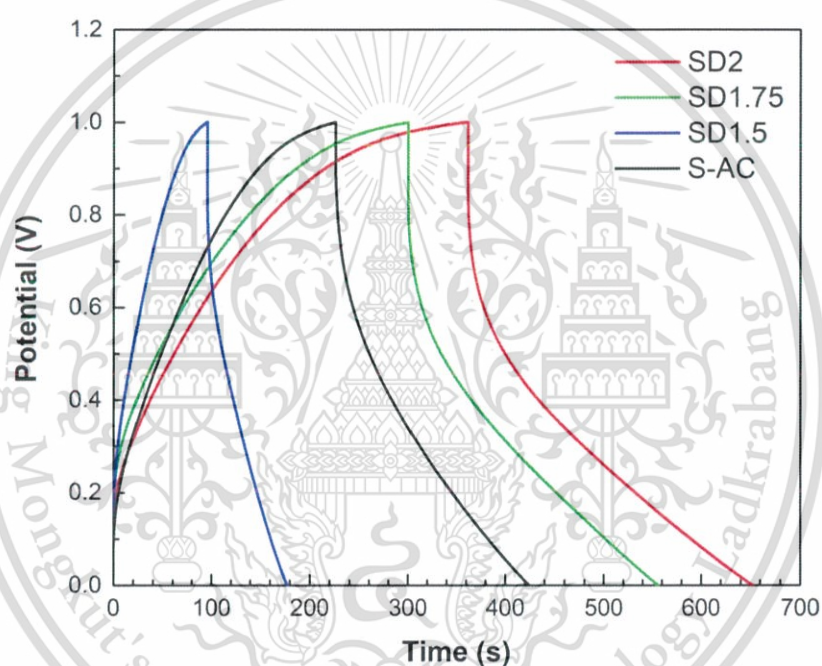


Figure S3 CD curves of the SD-and S-ACs

Table S1. Comparison of electrochemical performance in organic electrolyte of this work and other recently works

Precursors	Carbonization	Activation agent	Activation temperature/time (°C/h)	SSA ^a (m ² g ⁻¹)	C _s ^b (F g ⁻¹)	i ₀ ^c (A g ⁻¹)	Electrolyte *	Max E ^d (Wh kg ⁻¹)	Max P ^e (W kg ⁻¹)	Voltage (V)	Ref.
Silkworm pupae	HTC	ZnCl ₂	800/1	1188	91	0.2	1 M TEABF ₄ /PC	17.5	1698	2.5	1
Tobacco rods	HTC	KOH	900/1	2097	144	0.5	CH ₃ (C ₂ H ₅) ₃ NBF ₄ /AN	31.3	625	2.5	2
Wheat bran	HTC	KOH	800/1	2189	129	0.25	1 M TEABF ₄ /AN	32.7	1351	2.7	3
Green leaves	Pyrolysis/600	NaOH	720/1	2664	188	0.02	1 M TEABF ₄ /PC	39	1700	2.5	4
Paper pulp	HTC	KOH	800/1	2980	166	0.1	1 M TEABF ₄ /AN	30	57	3.0	5
Silkworm cocoon	Pyrolysis/500	KOH	900/2	3386	156	5	1 M TEABF ₄ /AN	34.4	3125	2.4	6
Seaweeds	Pyrolysis/900	-	-	1307	94	1	1 M TEABF ₄ /AN	17.3	1150	2.3	7
Rice husk	-	Microwave assisted ZnCl ₂	600 W	1552	94	0.05	1 M TEABF ₄ /PC	19.3	1007	2.7	8
Coconut shell	-	ZnCl ₂ +FeCl ₃	900/1	1874	196	1	1 M TEABF ₄ /PC	54.7	10000	3.0	9
Onion husks	-	K ₂ CO ₃	800/1	2571	188	0.5	1 M TEABF ₄ /AN	47.6	675	2.7	10
<i>S. saman</i> leaves	-	NaOH	720/1	2930	179	0.02	1 M TEABF ₄ /PC	79	830	3.5	This work

^a SSA: Specific surface area. ^b C_s: Specific capacitance. ^c i₀: Current density. ^d E: Energy density. ^e P: Power density.

*Electrolyte: TEABF₄/PC: Tetraethylammonium tetrafluoroborate in propylene carbonate, TEABF₄/AN: Tetraethylammonium tetrafluoroborate in acetonitrile, CH₃(C₂H₅)₃NBF₄/AN: Triethyl-methyl-ammonium tetrafluoroborate in acetonitril

AUTHOR BIOGRAPHY

Name-Surname Miss Vichuda Sattayarut
Date of Birth February 18, 1981
Present Address 50/664 Rungsit-Nakornnayok Rd., Thayaburi, Phatumtani
Province 12130 Thailand

Education

1999-2002 Bachelor of Science (Applied Physics),
King Mongkut's Institute of Technology Ladkrabang, Thailand
2006-2011 Master of industrial Engineering, Faculty of Engineering
Thammasat University, Thailand

Work Experience

2003-2016 Senior supervisor production engineer,
NEC TOKIN Electronics (Thailand) Co.,Ltd

Publications:

- (1) Vichuda Sattayarut, Thanthamrong Wanchaem, Pundita Ukkakimapan, Visittapong Yordsri, Paweena Dulyaseree, Mayuree Phonyiem, Michiko Obata, Masatsugu Fujishige, Kenji Takeuchi, Winadda Wongwiryapan, Morinobu Endo.

“Nitrogen self-doped activated carbons *via* the direct activation of *Samanea saman* leaves for high energy density supercapacitors.”

RSC Advances. 2019, 9 (38), 21724

- (2) Vichuda Sattayarut, Charathorn Chanthad, Pongtanawat Khemthong, Sanchai Kuboon, Thanthamrong Wanchaem, Mayuree Phonyiem, Michiko Obata, Masatsugu Fujishige, Kenji Takeuchi, Winadda Wongwiryapan, Paisan

This material is reserved for educational use only, not allowed for commercial use.

Forbidden to modify the content, and cite the document when use.

Khanchaitit, Morinobu Endo.

“Preparation and electrochemical performance of nitrogen-enriched activated carbon derived from silkworm pupae waste.”

RSC Advances. 2019, 9 (18), 9878.

Conferences:

- (1) Vichuda Sattayarut, Charathorn Chanthad, Pongtanawat Khemthong, Sanchai Kuboon, Thanthamrong Wanchaem, Mayuree Phonyiem, Michiko Obata, Masatsugu Fujishige, Kenji Takeuchi, Winadda Wongwiriyan, Paisan Khanchaitit, Morinobu Endo.

“Nitrogen self-doped activated carbon derived from silkworm pupae waste for performance enhancement of supercapacitor.”

The 2nd MRS Thailand International Conference 2019, Pattaya, Thailand, July 10-12 2019 (Poster presentation).

- (2) Vichuda Sattayarut, Pundita Ukkakimapan, Paweena Dulyaseree, Visittapong Yordsri, Mayuree Phonyiem, Nattapot Lerkkasemsan and Winadda Wongwiriyan

“Comparative Study on the Microstructures and Electrochemical Properties of CO₂- and Steam-Activated Carbons Derived from Sugarcane Bagasse”

The 13th International Conference on Ecomaterials 2017, Bangkok, Thailand, November 19-23, 2017 (Poster presentation).

- (3) Vichuda Sattayarut, Paweena Dulyaseree, Visittapong Yordsri, Pundita Ukkakimapan, Mayuree Phonyiem and Winadda Wongwiriyan

“Hierarchical nitrogen-enriched activated carbon derived from *Samanea saman* leaves for Supercapacitor application.”

The 1st MRS Thailand International Conference 2017, Chiang Mai, Thailand, October 31 – November 3, 2017 (Poster presentation).

- (4) Vichuda Sattayarut, and Winadda Wongwiriyan.

“Supercapacitor properties of activated carbon derived from *Samanea*

This material is reserved for educational use only, not allowed for commercial use.

Forbidden to modify the content, and cite the document when use.

saman leaves”,

The 27th International conference on Diamond and Carbon, Materials, Montpellier, France, September 4-8, 2016 (Poster presentation).

(5) Vichuda Sattayarut, and Parichat Chuenwathanakul,

“Optimization at anode connection of Tantalum capacitor by DOE method”

The 39th IE Network conference 2010, Ubonratchathani, October 13-15, 2010 (Oral presentation)

Awards:

- (1) Outstanding poster presentation: The 13th International Conference on Ecomaterials 2017, Bangkok, Thailand, November 19-23, 2017.
- (2) Best poster presentation: The 1st MRS Thailand International Conference 2017, Chiang Mai, Thailand, October 31 – November 3, 2017

